

Synthesis and defect characterization of pure phase Zr-MOFs
based on meso-tetracarboxyphenylporphyrin (TCPP)

Shaunak Shaikh

Thesis submitted to the faculty of the Virginia Polytechnic Institute and State University in
partial fulfillment of the requirements for the degree of Master of Science in Chemistry

Chair – Amanda J. Morris

Co-Chair – Nicholas J. Mayhall

Member – James Tanko

Member – Diego Troya

October 30, 2018 Blacksburg, VA

Key words: Metal-Organic Frameworks, porphyrins, polymorphism, defects, energy transfer

Abstract

Chapter 1: The unique chemical and biological properties of porphyrins have led to increased interest in the development of porphyrin-based materials. Metal organic frameworks (MOFs) can act as a scaffold for the immobilization of porphyrins in desired arrangements. The crystalline nature of MOFs allows for control over spatial arrangement of porphyrins and the local environment of the porphyrin molecules. This opens up the possibility of conducting systematic studies aimed at exploring structure-property relationships. Several strategies for the design and synthesis of porphyrin-based frameworks have been developed over the last two decades, such as, the pillared-layer strategy, construction of nanoscopic metal–organic polyhedrals (MOPs), post-synthetic modification, etc. These strategies provide an opportunity to engineer porphyrin-based MOFs that can target a specific application or serve as multi-functional assemblies. Porphyrin-based MOFs provide a tunable platform to perform a wide variety of functions ranging from gas adsorption, catalysis and light harvesting. The versatile nature of these frameworks can be exploited by incorporating them in multi-functional assemblies that mimic biological and enzymatic systems. Nano-thin film fabrication of porphyrin-based MOFs broadens their application range, making it possible to use them in the construction of photovoltaic and electronic devices.

Chapter 2: The reaction of zirconium salts with meso-tetracarboxyphenylporphyrin (TCPP) in the presence of different modulators results in the formation of a diverse set of metal-organic frameworks (MOFs), each displaying distinct crystalline topologies. However, synthesis of phase-pure crystalline frameworks is challenging due to the concurrent formation of polymorphs. The acidity and concentration of modulator greatly influence the outcome of the MOF synthesis. By

systematically varying these two parameters, selective framework formation can be achieved. In the present study, we aimed to elucidate the effect of modulator on the synthesis of zirconium-based TCPP MOFs. With the help of powder X-ray diffraction (PXRD) and scanning electron microscopy (SEM), modulator candidates and the optimal synthetic conditions yielding phase-pure PCN-222, PCN-223 and MOF-525 were identified. ^1H NMR analysis, TGA and N_2 gas sorption measurements were performed on select MOFs to gain insight into the relationship between their defectivity and modulator properties.

Chapter 3: Singlet-singlet energy transfer in PCN-223(free-base), a highly stable Zr-MOF based on meso-tetrakis(4-carboxyphenyl)porphyrin was investigated, using diffuse reflectance spectroscopy, steady-state emission spectroscopy, time-correlated single photon counting (TCSPC) spectroscopy and nanosecond transient absorption spectroscopy. The effects of the surrounding media and temperature on the excited-state properties of PCN-223(fb) were explored to understand the mechanistic aspects of energy transfer. Stern-Volmer photoluminescence quenching of PCN-223(fb) suspensions was performed to extract quenching rate constants and gain insight into the efficiency of energy transfer.

Chapter 4: The fourth chapter of this thesis is adapted from chapter 14 of the book “Elaboration and Applications of Metal-Organic Frameworks” authored by Jie Zhu, Shaunak Shaikh, Nicholas J Mayhall and Amanda J Morris. This chapter summarizes the fundamental principles of energy transfer in MOFs and provides an overview of energy transfer in lanthanide-Based luminescent MOFs, Ru/Os-Based MOFs, porphyrin- and metalloporphyrin-based MOF materials, and nonporphyrinic, organic chromophore-based MOFs.

General Audience Abstract

Metal Organic frameworks (MOFs) composed of Zirconium-oxo clusters connected through meso-tetra(4-carboxyphenyl)porphyrin (TCPP) linker molecules have emerged as promising solid-state materials because of their unique structural features and diverse applications. Although these MOFs have demonstrated great potential over the years, synthesizing them in phase-pure form has proven to be very challenging as they are susceptible to polymorphism. Syntheses of these frameworks often result in phase mixtures and have poor reproducibility. To address, this issue, we conducted a systematic exploration of the synthetic parameter landscape to identify reaction conditions for the synthesis of phase-pure Zirconium-based porphyrin MOFs, and to gain deeper insights into the factors governing the formation of these MOFs. We also investigated the defectivity of pristine Zr-TCPP MOFs using a variety of techniques, including ^1H NMR spectroscopy, thermogravimetric analysis (TGA), inductively coupled plasma mass spectrometry (ICP-MS), and Nitrogen gas adsorption/desorption measurements. The long-term goal of this project is to use phase-pure Zr-based porphyrin MOFs as model systems to study energy transfer in three dimensional structures. To achieve this goal, we characterized the photophysical properties of PCN-223(fb) (a Zr-based porphyrin MOF) using a variety of techniques including steady-state photoluminescence spectroscopy, time-resolved photoluminescence spectroscopy, nanosecond transient absorption spectroscopy and femtosecond transient absorption spectroscopy. Understanding the mechanistic aspects of energy transfer in PCN-223(fb) can pave the way for the design of a new generation of solar energy conversion devices.

Table of contents

Acknowledgements	I
Attributions	II
1. Porphyrin based frameworks: materials design, synthetic strategies, and emerging applications	
1.1 Introduction.....	1
1.2 Synthetic strategies for building functional porphyrin.....	5
1.2.1 Pillared-layer strategy.....	5
1.2.2 Construction of nanoscopic metal-organic polyhedrons (MOPs).....	9
1.2.3 Post synthetic modification.....	11
1.3 Applications of porphyrinic MOFs.....	12
1.3.1 Guest molecules absorption and separation.....	12
1.3.2 Catalysis.....	14
1.3.2.1 Oxidation catalysis.....	14
1.3.2.2 Lewis acid catalysis.....	16
1.3.2.3 Photocatalysis.....	18
1.3.4 Nano-thin film fabrication.....	18
1.4 Conclusion.....	20
1.5 Bibliography.....	21
2. Synthesis and defect characterization of pure phase Zr-MOFs based on TCPP ligand	
2.1 Introduction.....	25
2.2 Experimental procedures.....	27
2.3 Results and discussion.....	30
2.4 Defect characterization.....	38

2.5 Conclusion.....	43
2.6 Bibliography.....	44
3. Photophysical characterization of PCN-223(fb)	
3.1 Introduction.....	48
3.2 Experimental procedures.....	49
3.3 Results and discussion.....	51
3.4 Conclusion	62
3.5 Bibliography	63
3.6 Supplementary Information.....	66
4. Energy Transfer in Metal-Organic Frameworks	
4.1 Background information about energy transfer.....	70
4.1.1 Coupling Regimes	71
4.1.1.1 Strong coupling.....	71
4.1.1.2 Weak coupling.....	72
4.1.2 Coupling mechanisms.....	73
4.1.2.1 Distance dependence of coupling mechanisms.....	74
4.1.2.2 Dexter-type integral, $(ab ji)$	75
4.1.2.3 Förster-type integral, $(ai jb)$	76
4.2 Why MOFs.....	79
4.3 Lanthanide-based luminescent MOFs.....	81
4.3.1 ET in Ln-node-based MOFs.....	85
4.3.2 Ln@MOF.....	99

4.3.3 Summary.....	102
4.4 Ru/Os-based MOFs.....	103
4.4.1 Ru/Os in Zn-Node-based MOFs.....	105
4.4.2 Ru(bpy) ₃ ²⁺ -doped zirconium(IV) MOFs.....	112
4.4.3 Summary.....	116
4.5 Porphyrin- and metalloporphyrin-based MOF materials.....	116
4.5.1 Porphyrin-based MOFs as crystalline powders.....	118
4.5.2 Porphyrin-based MOFs as thin films.....	125
4.5.3 Summary.....	129
4.6 Non-porphyrinic, organic chromophore-based MOFs.....	130
4.6.1 Summary.....	135
4.7 References.....	136

Acknowledgements

To begin with, I would like to thank my advisor, Dr. Amanda Morris. Thank you for believing in me and for your continued support throughout my time in graduate school. I would also like to thank you for all that you taught me since the time I started as a graduate student and for guiding me in difficult situations. I am very grateful to Dr. Nicholas Mayhall, my co-advisor. Thank you for your guidance, constant encouragement and for being patient with me when I was a new graduate student. I would like to express my gratitude to Dr. James Tanko and Dr. Diego Troya, my other committee members. I am grateful for your input as members of my committee and for your valuable feedback. I owe a deep sense of gratitude towards Dr. Pavel Usov. I am also thankful to the current and previous members of Morris group and Mayhall group for helping me in my research efforts and for your friendship. Finally, I would like to thank my family for their unwavering support and encouragement during the graduate school.

Attributions

The second chapter of this thesis is based on a research project that aims to synthesize phase-pure MOFs and understand their defect chemistry. Dr. Pavel Usov, a previous post-doctoral researcher in the Morris group, contributed towards experimental design of the project. Meng Cai, a graduate student in the Morris group, collected Scanning Electron Microscopy (SEM) images of all the MOFs synthesized during the course of the project. Jie Zhu from Morris group provided assistance in gas adsorption measurements of phase-pure MOFs. Digested MOF samples were sent to Dr. Jeffrey Parks (Civil Engineering Department, Virginia Tech) for performing ICP-MS measurements.

The third chapter of this thesis is based on a research project that aims to carry out photophysical characterization of PCN-223(fb) MOF. Dr. Arnab Chakraborty, the current post-doctoral researcher in the Morris group, provided assistance in transient absorption measurements of the ligand and MOF. Jamie Alatis, an undergraduate researcher in the Morris group, assisted with MOF synthesis and experimentation.

Chapter-1

Porphyrin based frameworks: materials design, synthetic strategies, and emerging applications

1.1 Introduction-

Metal Organic frameworks (MOFs) are composed of metal centers or metal oxide clusters connected through organic linker molecules to give crystalline structures with a network of interconnected pores and channels. The organic linkers provide synthetic tunability while the inorganic nodes provide robustness and mechanical stability to the structure.¹ Owing to their ordered crystalline structure, diverse topological features and well-defined chemical functionalities, MOFs have shown immense potential for applications in drug delivery,²⁻⁴ catalysis,^{5,6} light harvesting,⁷⁻⁹ gas storage,^{10,11} and gas separation.¹² (Fig. 1)

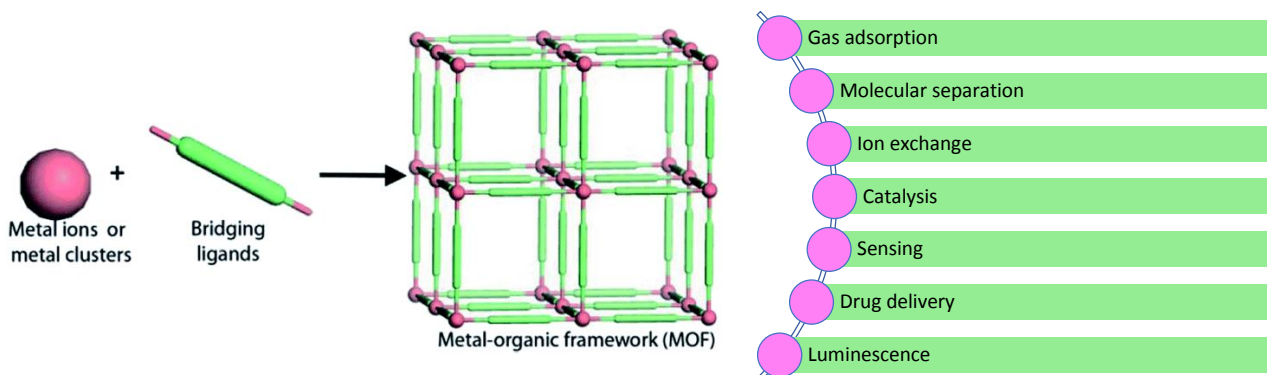


Figure 1. Schematic illustration of a metal–organic framework, assembled from organic linkers and metal nodes along with its application¹

Porphyrins and their metallo-derivatives play a vital role in several biological systems. They perform essential biochemical, enzymatic, and photochemical functions in natural systems like catalase, peroxidases and P450 cytochrome.¹³ Due to their high thermal and chemical stabilities, robust nature, and facile synthesis, they have also found use in the development of anti-cancer drugs, catalysts, semiconductors, superconductors, electronic materials, and nonlinear optical materials.¹⁴⁻¹⁹ Given that the electronic and optical properties of porphyrins and metalloporphyrins can

be synthetically tuned, incorporating them in coordination architectures like MOFs offers the opportunity of mimicking their diverse biological functionalities.

There has been a rapid growth in the field of porphyrin-based MOFs since 1990's. The first porphyrin based MOF was reported by Robson and co-workers in 1991.²⁰ The Robson group built a three-dimensional network consisting of Cd ion nodes linked through palladium-based tetrapyrrolyl porphyrin ligands (Fig. 2). This was the first example of a heterometallic MOF where the metal ion coordinated in the porphyrin core differed from the identity of metal ion comprising the metal node. This seminal study triggered the discovery of a wide variety of porphyrin-based MOFs over the next two decades. In the years to come, framework stability emerged as a key issue as the Cd-based MOFs reported by Robson group lost their structural integrity and collapsed upon removal of solvent molecules from the pores. In 1999, Lin reported the structure of SMTP-1, a layered framework built via self-assembly of tetra(4-pyridyl)porphyrin and Co(II) or Mn(II) metal ions.²¹ The notable feature of this framework is the axial coordination of two adjoining porphyrin pyridyl groups on the porphyrin metal centers, which supports the framework and prevents the pores from collapsing upon solvent removal. The stability of framework after solvent removal at 200° C was confirmed by powder X-Ray diffraction (PXRD). However, the metal center is coordinated by four nitrogen atoms of the porphyrin and two nitrogen atoms of the adjoining porphyrin pyridyl groups, leaving no open metal sites for further functionalization.

One of the earliest attempts to build a functional porphyrin-based MOF was made by Suslick and co-workers, who reported the structures of PIZA-1 and PIZA-3. PIZA-1 ($[\text{CoT}(p\text{-CO}_2)\text{PPCo}_{1.5}]$) consists of an assembly of trinuclear Co(III)-carboxylate building clusters linked through Co(III) tetra(4-carboxyphenyl)porphyrin.²² (Fig. 3) It possesses two sets of channels, one that run along the

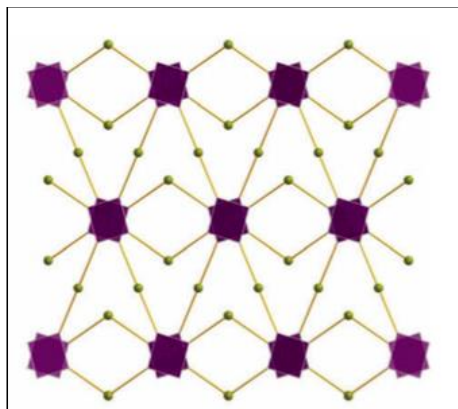


Figure 2. A representation of Pd-porphyrin based framework built by Robson and co-workers²⁰

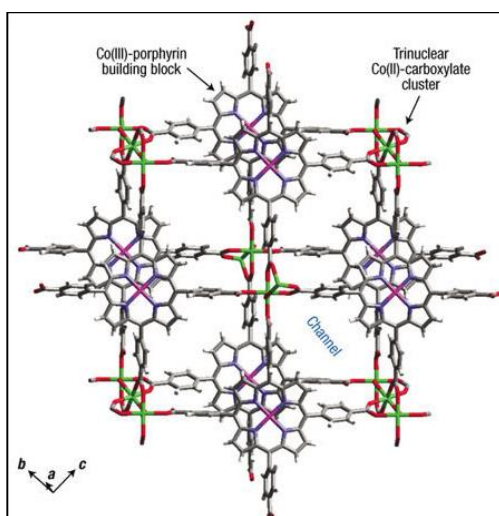


Figure 3. PIZA-1 framework viewed along a axis²²

“b” and “c” axes ($9 \times 7 \text{ \AA}^2$) and the other one along “a” axis ($14 \times 7 \text{ \AA}^2$). The walls of these large, pervasive channels are functionalized by porphyrin metal centers that ensure size-, shape- and functional group- selective adsorption of guest molecules. The evacuated host framework of PIZA-1 was exposed to a series of linear amines, aromatic amines, picoline derivatives, and alcohols, followed by gravimetric thermal desorption to monitor selective gas adsorption. By comparing the uptake capacity towards different guest molecules, it was revealed that PIZA-1 demonstrated size- and shape-selective sorption for less sterically hindered and more polar compounds (Fig. 4). In addition, PIZA-1 was shown to have

an exceptionally high, rapid water uptake capacity and retained its structural integrity even after 10 adsorption-desorption cycles.

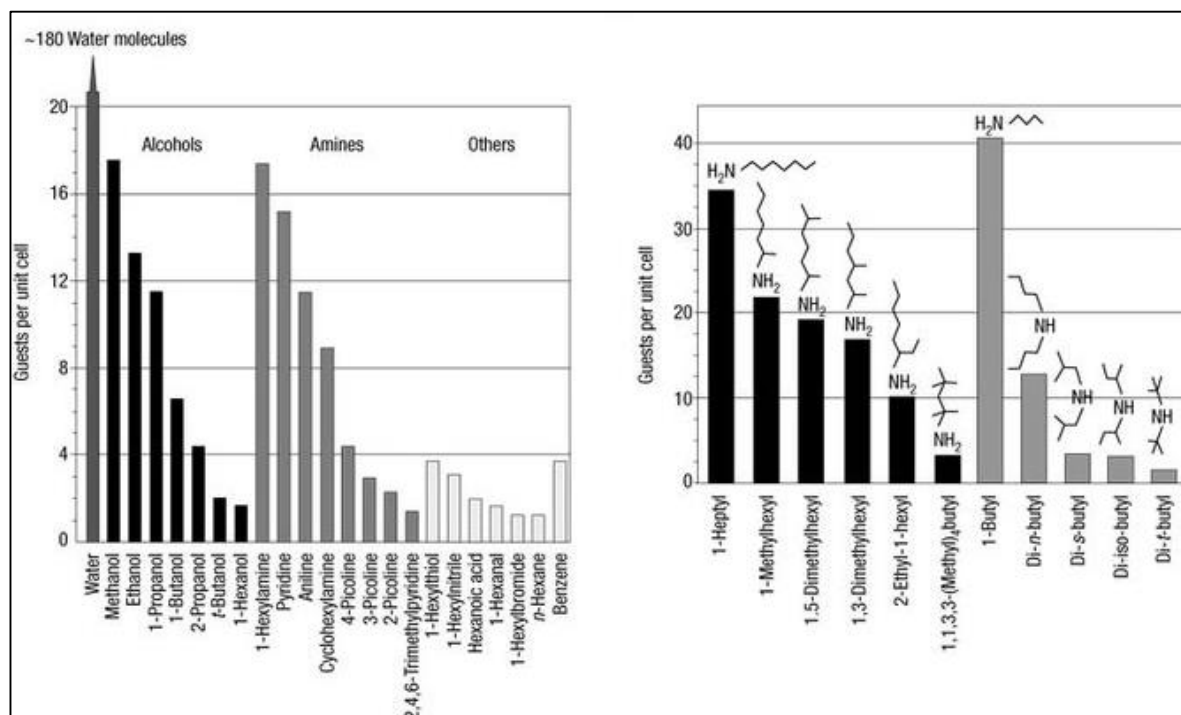


Figure 4. Size-, shape-, and functional-group selectivity of PIZA-1 as probed by thermal desorption of guest molecules²²

PIZA-3 was the first reported porphyrin-based framework that showed catalytic activity. PIZA-3 consists of Mn(III) tetra(4-carboxyphenyl)porphyrin coordinated to bent trinuclear Mn-clusters.²³ (Fig. 5) PIZA-3 was found to be a capable oxidation catalyst for hydroxylation of a variety of linear and cyclic alkanes and epoxidation of alkenes.

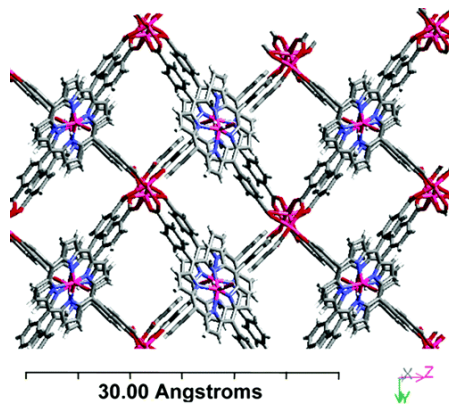


Figure 5. PIZA-3 network viewed along crystallographic a-axis. Solvate and coordinated DMF molecules have been removed for clarity.²³

Despite the interesting selective adsorption of PIZA-1 and catalytic properties of PIZA-3, they are fairly limited in terms of their performance and practical applicability. PIZA-1 has a relatively low surface area (BET surface area of $125 \text{ m}^2 \text{ g}^{-1}$ probed by nitrogen adsorption isotherm), resulting in low porosity.²² The constrained microporous channels of PIZA-3 hinder the accessibility to catalytic centers on the interior of the framework, causing the catalysis to occur predominantly on its exterior surface. This adversely affects the shape- and size- selectivity of the framework towards substrates and substantially slows down the catalytic oxidation process. In order to circumvent these limitations, it was highly desirable to build porphyrin-based frameworks that exhibit high surface area and enhanced catalytic activity. Research efforts aimed at developing porphyrinic MOFs with high surface area and catalytic activity faced two major challenges: (1) pore collapse due to the large open pores, (2) additional coordination to the metal inside the porphyrin by other porphyrin units, effectively saturating all metal sites.⁶ Efforts directed towards synthesis free-base MOFs followed by metallation of porphyrins via post-synthetic modifications to generate open metal sites were unsuccessful due to the tendency of unmetallated free-base porphyrin to coordinate to metal ions intended for metal node (secondary building unit) construction.

1.2 Synthetic Strategies for building functional porphyrin-based MOFs

1.2.1 Pillared-layer strategy

In recent years, synthetic strategies involving the formulation of desired porphyrinic architectures via judicious selection of metal nodes and custom-designed porphyrins and metalloporphyrins have received much attention from the scientific community. One such strategy that has been widely explored is the “pillared-layer strategy”. This strategy makes use of “pillar molecules” to connect the two-dimensional layers comprised of metal clusters (often referred to as paddlewheel) and porphyrin linkers.²⁴ Ditopic pillars like bipyridine analogues have been used extensively to interlink the

unsaturated sites on the 2D layers to form three-dimensional pillared layer frameworks. Such an arrangement provides three structural variables (porphyrin, paddlewheel, and pillar) that can be altered to systematically control topology and pore surface. In case of metallated porphyrins, there are three possible pillaring schemes: one heterogeneous AB (porphyrin-to-paddlewheel) connection, and two homogeneous pillaring connections: an AA (paddlewheel-to-paddlewheel) connection and an A'A' (porphyrin-to-porphyrin) connection (Fig. 6).

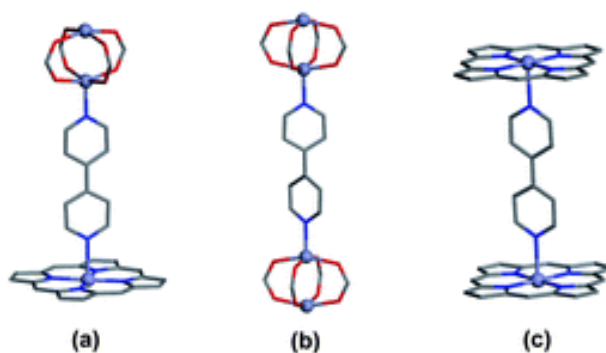


Figure 6. The three types of possible pillaring arrangements in porphyrin paddlewheel frameworks using a 4,4'-bipyridine ligand. (a) Heterogeneous AB, (b) homogeneous AA, and (c) homogeneous A'A' connections²⁴

Choi and co-workers showed that the coordination geometry of the metal center of the porphyrin governs the stacking sequence of the 2D layers. Metalloporphyrins with different metal centers (Co, Zn, and Pd) were used in this study, each representing 6-, 5- and 4- connected metal-coordination respectively. These metalloporphyrins along with metal clusters ($M_2(COO)_4$, ($M = Zn$ or Co)) and bipyridine pillars yielded different stacking patterns, depending on the coordination environment of the metal center. $Pd^{2+}(d^8)$ has a square planar geometry and prefers homogeneous pillaring such as that observed in PPF-5 (Fig 7). On the other hand, Zn^{2+} and Co^{2+} prefer heterogeneous pillaring such as that observed in PPF-3 and PPF-4.²⁴ Among the three stacking patterns, the AA pattern is considered desirable for applications targeting chemically active porphyrin metal centers in MOFs. This has led to the development of synthesis strategies that favor the formation of AA pattern over AB and A'A' patterns. For example, using a sterically hindered pillar like 2,2'-dimethyl-4,4'-bipyridine enables

selective coordination of the paddlewheel metal sites.²⁵ Steric effects induced due to the introduction of methyl groups make the coordination interactions between pyridyl groups and porphyrin metal centers unfavorable, leading to formation of AA-type patterns with potentially redox active porphyrin metal centers.

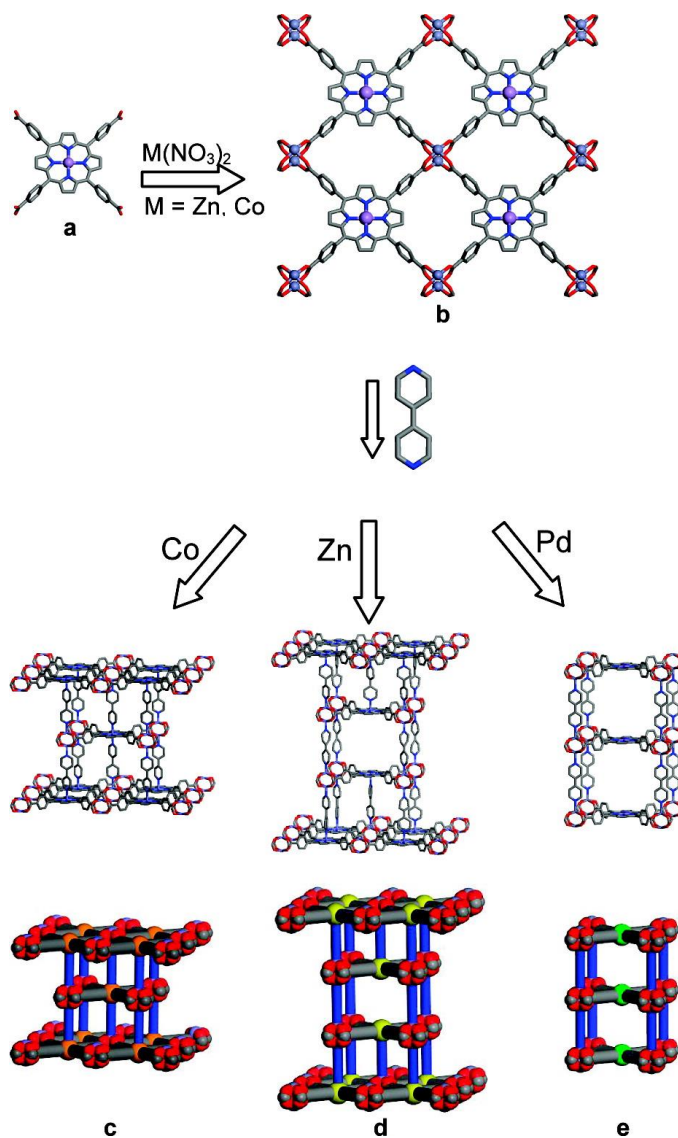


Figure 7. The 2D sheets are pillared with bipyridine to give (c) PPF-3 (Co), (d) PPF-4 (Zn), and (e) PPF-5 (Pd). The resulting stacking arrangements are dependent on the preferred coordination geometry of the porphyrin metal centers²⁴

Porphyrins can not only act as paddle-wheel building units, but also as pillaring ligands. Hupp and co-workers used free-base dipyrindyl porphyrin as pillars and a tetratopic carboxylate (1,2,4,5-tetrakis(4-carboxyphenyl)benzene) as struts to construct a highly porous ZnPO-MOF.²⁶

The ZnPO-MOF featured a high degree of porosity and contained fully reactant-accessible metalloporphyrin sites. It was also the first metalloporphyrin-based MOF to show catalytic activity in the interior of the material. It is worth noting that attempts to extend this approach to incorporate catalytically more active metals like Mn(III) were thwarted by the propensity of Mn(III)-porphyrin to form 2D networks in which the intended active site serves as an auxiliary node.

Synthesis of MOFs with catalytically active Fe- or Mn-porphyrin sites is challenging because these metals tend to prefer penta- or hexa-coordination, which results in ligation of both the paddlewheel and porphyrin metal sites. Hupp and co-workers used two strategies to avoid this problem.²⁷ The first strategy involved using a tetracarboxylated porphyrin ligand (L_1) in conjunction with a bulky dipyriddy porphyrin pillar (L_2) to create a structure with as few pillars as possible. Tetracarboxylated porphyrin ligands are known to produce MOFs particularly sensitive to steric effects, leading to the preferential formation of non-interpenetrated structures. The steric bulk associated with dipyriddy porphyrin ligands should prevent pillar coordination with metal centers of porphyrins. The second strategy exploits the differences in solubility of the pyridyl- and carboxylate-porphyrin struts. By choosing a mixture of solvents in which the tetracarboxylate porphyrin has a much better solubility than dipyriddy porphyrin (1:1 v/v DMF/EtOH), the growing 2D sheets of MOFs have access to a lower concentration of the dipyriddy porphyrin units. This should allow the pillars to coordinate to more favorable sites, i.e. paddlewheel sites. Hupp's group successfully implemented these strategies to incorporate numerous metalloporphyrins (Mn^{3+} , Fe^{3+} , Zn^{2+} , Pd^{2+} , and Al^{3+} complexes) in highly stable and porous MOFs called RPMs (robust porphyrinic materials). (Fig. 8)

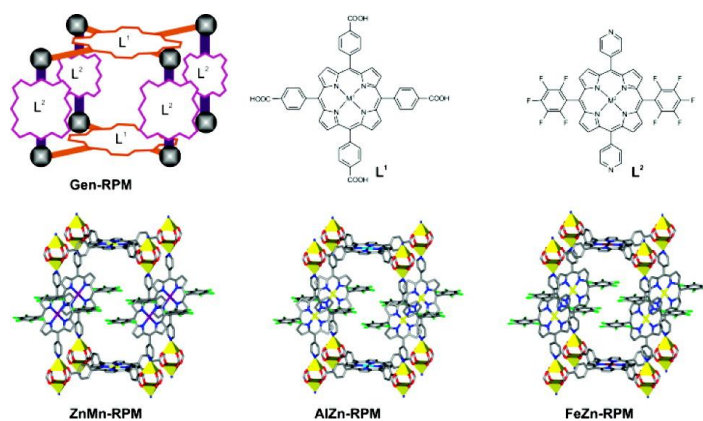


Figure 8. Top left: A schematic representation of a generic RPM unit cell, based on sheet formation by the tetraacid ligand (L_1) pillaring by a dipyridyl strut (L_2). The gray-black spheres are the paddlewheel-coordinated zinc nodes. Top center and right: Structures of the porphyrinic struts (L_1 and L_2) used to synthesize the RPM series. Bottom: Crystallography-derived stick representations of the unit cells of three RPMs.²⁷

1.2.2 Construction of nanoscopic metal-organic polyhedrons (MOPs)

Another strategy for designing and synthesizing porphyrinic frameworks is the construction of nanoscopic metal-organic polyhedral (MOP) cages in MOFs. The MOP cage serves as a secondary building block (SBB) that supports the structure of MOF and can be functionalized in order to optimize interactions with guest molecules. The π electron rich walls of these cages and the high density of open metal sites confined in a nanospace makes the MOP-based porphyrinic frameworks highly versatile materials. Ma and co-workers were the first to show that the vertex-linking of isophthalate ligands with metal paddlewheel clusters ($M_2(\text{COO})_4$, ($M = \text{Zn}, \text{Cu}, \text{Co}$)) allows generation of several type of faceted MOPs. In 2011, they reported MMPF-1 (the first example of a MOP-based MOF), built from 5,15-bis(3,5-dicarboxyphenyl)porphine (bdcpp) and dicopper paddlewheel node (Fig. 9).²⁸ In each cage, there are 8 open Cu sites associated with metallated bdcpp ligand and 8 open Cu sites associated with the dicopper paddlewheel cluster. All 16 open sites point towards the center of the cage, resulting in a very high density of open metal sites (~ 7 open metal sites per nm^3). Ma and co-workers later used a custom-designed ligand 5,15-bis(3,5-dicarboxyphenyl)-10,20-bis(2,6-dibromophenyl)porphyrin (dcdbp) and a dicopper paddlewheel SBU to form MMPF-3.²⁹ Interestingly, MMPF-3 is comprised of

three types of polyhedral cages: cubohemioctahedron, truncated octahedron and truncated tetrahedron that are connected together to form a 3D framework.

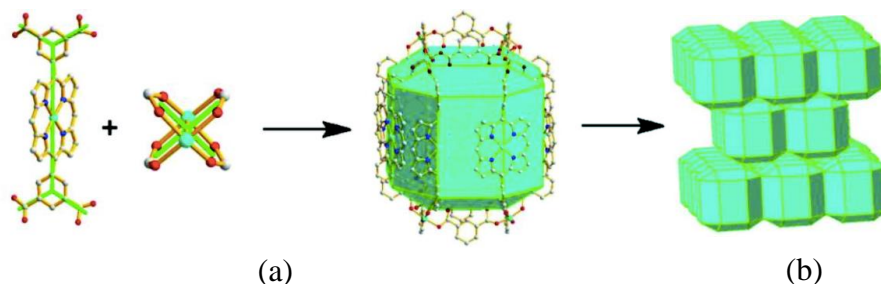


Figure 9. (a) Illustration of linking bdcpp ligand and dicopper paddlewheel to form the irregular rhombicuboctahedral cage (MOP). (b) MOPs serving as SBBs to form the MMPF-1 framework²⁸

In 2012, Ma and co-workers also designed an approach to build porphyrinic frameworks having SBBs with high connectivity and high symmetry, which was a rarity at that time. By connecting the triangular $Zn_2(NO_3)_2$ or $Cd_2(NO_3)_2$ moieties by square planar tetrakis(3,5-dicarboxyphenyl)porphyrin (tdcpp) units, MMPF-4 (Zn) and MMPF-5 (Cd) were constructed (Fig. 10).³⁰ The SBB in MMPF-4 and MMPF-5 is a small cubicuboctahedron composed of the faces of six Zn-tdcpp/Cd-tdcpp moieties that are linked by eight $Zn_2(CO_2)_3$ / $Cd_2(NO_3)_2$ units.

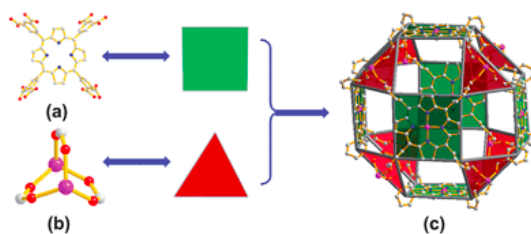


Figure 10. a) Tdcp serves as a square SBU; (b) $Zn_2(CO_2)_3$ paddlewheel moiety serves as a triangular SBU; (c) the small cubicuboctahedron in MMPF-4 is formed by 6 square Zn-tdcpp units and 8 triangular $Zn_2(CO_2)_3$ units³⁰

The utilization of metal-oxo clusters with high symmetry and high connectivity as SBUs allows formation of frameworks that incorporate nanoscopic polyhedral cages, as illustrated by Zirconium based porphyrin MOFs like MOF-525, PCN-222 and PCN-223 (Fig. 11).³¹⁻³³ MOF-525, reported by Morris et al., is assembled by the 12-connected zirconium cuboctahedral SBU, $Zr_6O_4(OH)_4(CO_2)_{12}$, and 5,10,15,20-tetrakis(4-carboxyphenyl)porphyrin (tcpp).³¹ It consists of two types of polyhedral cages.

The smaller cage, a distorted octahedron with a cavity diameter of ~ 1.1 nm, comprises of two Zr SBUs in the horizontal direction and four tcpp ligands linked to the two SBUs. The other cage, a cube with edge length of ~ 2.0 nm, consists of eight Zr SBUs at the vertices and six tcpp ligands at the faces. PCN-222 consists of Zr_6 nodes connected to 8 tetracarboxylate linkers with the carboxylate groups adopting a bridged conformation. Unlike the 12-connected Zr_6 cluster observed in MOF-525, only eight edges of the Zr_6 octahedron are bridged by carboxylates from TCPP ligands in PCN-222, while the remaining positions are occupied by terminal hydroxy groups.³² Consequently, the symmetry of the Zr_6 clusters is reduced from O_h to D_{4h} . The additional space engendered due to the reduction in symmetry results in the formation of mesopores. PCN-223, in particular, has a very unique structure. It consists of unprecedented D_{6h} symmetric $[Zr_6O_4(OH)_4]^{12+}$ nodes connected to 12 TCPP linkers, representing the first (4,12)-connected MOF with the “shp” topology.³³ PCN-223 contains uniform triangular 1D channels of 12 Å in diameter delimited by three Zr_6 units and three TCPP linkers. Since Zr(IV) fails to metallate the porphyrin during the synthesis of MOF-525, PCN-222 and PCN-223, the porphyrin remains in the free-base form and can be metallated. This opens up the possibility of functionalizing these polyhedral cages by metalating the porphyrin with various metal ions.

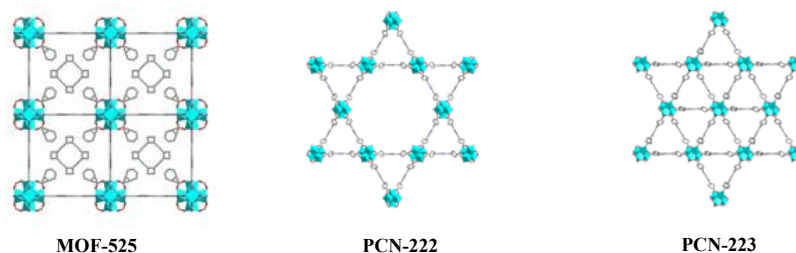


Figure 11. Examples of Zr-MOFs based on tetrakis(4-carboxyphenyl)porphyrin

1.2.3 Post synthetic modification

Post-synthetic metalation has been used to introduce a wide-variety of metals in free-base porphyrinic MOFs to furnish desired functionality. In a similar approach, metal ions weakly coordinated to the

porphyrin core can be exchanged by other suitable metals that are catalytically active.²⁴ Post-synthetic ligand exchange has also been observed in pillared porphyrinic MOFs, where the dipyrridyl pillaring linkers are replaced by molecules with similar structure.³¹ A single-crystal to single-crystal transformation can also be achieved via post synthetic ligand exchange. Fig. 12 illustrates how introduction of bipyridine linker to crystals of PPF-18 and PPF-20 transforms them to PPF-27 and PPF-4, respectively. The new frameworks retain the topology of their parent frameworks.

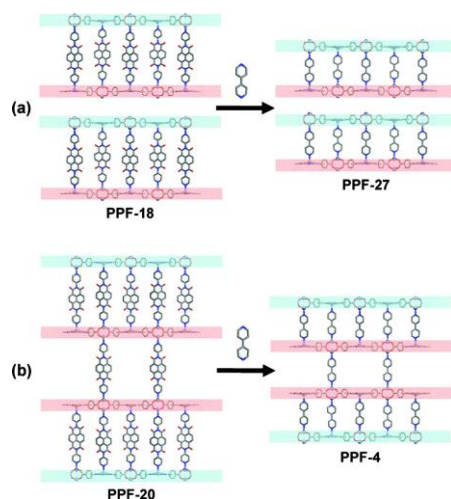


Figure 12. Introduction of the bridging linker 4,4'-Bipyridine to crystals of (a) PPF-18 and (b) PPF-20, transforming them to PPF-27 and PPF-4, respectively. Blue and pink bands represent “A” and “B” layers, respectively. The AB and ABBA topologies in PPF-18 and PPF-20 are retained in PPF-27 and PPF-4, respectively, showing a templating effect.³¹

1.3 Applications of porphyrinic MOFs

Porphyrinic MOFs have diverse set of applications in the fields of guest molecule adsorption and separation, catalysis and nano-thin films.

1.3.1 Guest molecules absorption and separation

Initial studies dealing with functional microporous behavior of porphyrinic MOFs were inspired from similar studies on inorganic Zeolites. As discussed before, PIZA-1 was the first porphyrinic MOF to exhibit size-, shape- and functional group- selective adsorption behavior for a series of linear amines, aromatic amines, picoline derivatives, and alcohols.²² PIZA-1 has a much higher accessible pore volume

than well-known molecular sieves like Zeolite 4A. The hydrophilic nature of its constrained pores made it an efficient desiccant for the selective drying of common organic solvents (for example, benzene, toluene and tetrahydrofuran). However, it is still considerably limited by its relatively low surface area (125 m²/g). Since the discovery of PIZA-1, several breakthroughs have been made in the preparation of porous porphyrin-derived MOFs with improved gas uptake capacity and separation ability. For example, PPF-1 was shown to have permanent microporosity, confirmed by a type-I nitrogen sorption isotherm at 77 K with a surface area of 622.4 m²/g.³²

MMPF-1, the first MOP-based MOF reported by Ma and co-workers, selectively adsorbs H₂ and O₂ over N₂, and CO₂ over CH₄. A significant difference is found in the amount of N₂ (5 cm³/g) and H₂ (50 cm³/g) uptake at 77 K and 760 Torr.³⁰ Gas adsorption studies conducted at 154 Torr (saturation pressure of O₂) revealed an O₂ uptake of 45 cm³/g, much higher than that of N₂ (Figure 13(a)). It was also found out that at 760 Torr, MMPF-1 can take up a larger amount of CO₂ (80 cm³/g) as compared to CH₄ (18 cm³/g) (Figure 13(b)). The selectivity of MMPF-1 is attributed to its small aperture size ~3.5 Å, which excludes larger molecules like N₂ (kinetic diameter ~ 3.64 Å) and CH₄ (kinetic diameter ~ 3.8 Å) but allows entry of smaller molecules like H₂ (kinetic diameter ~ 2.89 Å), O₂ (kinetic diameter ~ 3.46 Å) and CO₂ (kinetic diameter ~ 3.3 Å).

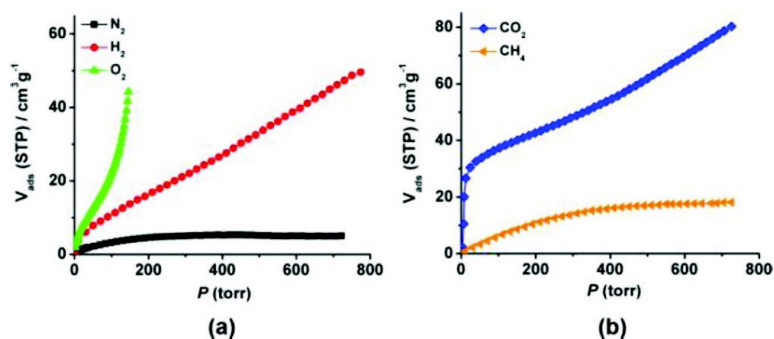


Figure 13. Gas adsorption isotherms of MMPF-1 at (a) 77 K and (b) 195 K³⁰

1.3.2 Catalysis

Porphyrins and metalloporphyrins are widely accepted as homogeneous catalysts possessing high catalytic activity towards the hydroxylation of alkanes and epoxidation of alkenes. MOFs that demonstrate high porosity and incorporate catalytically active porphyrins/metalloporphyrins as struts can serve as size- and shape-selective heterogeneous catalysts. In addition, the recyclability of the heterogeneous catalysts is an attractive attribute in large-scale reactions involving separation processes and waste disposal. Depending on the mechanism involved, the catalytic reactions carried out using porphyrinic MOFs can be divided into three main categories: oxidation catalysis, Lewis acid catalysis, and photocatalysis.

1.3.2.1 Oxidation catalysis

MMPF-3, a MOP based porphyrinic framework with a high density of open cobalt sites has been tested for its catalytic performance in the epoxidation of trans-stilbene.²⁹ Oxidation reactions were carried out with MMPF-3 and other controls like homogenous Co(dcdp), fcu-MOF-1, PPF-1(Co), and MMPF-2 in the presence of an oxidant (Tert-Butyl hydro-peroxide (tbhp)). MMPF-3 demonstrated better conversion efficiency in comparison to all the controls and also maintained its catalytic activity for eight cycles without showing any signs of leaching of cobalt ion (active site) or structural disintegration (Fig. 14).

Styrene epoxidation has been successfully demonstrated using homogeneous catalyst 5,10,15,20-tetrakis(pentafluorophenyl) porphyrin-Mn(Cl) and the heterogeneous framework Mn-RPM prepared using this ligand²⁷. In the presence of 2-(tert-butylsulfonyl)iodosylbenzene as oxidant, the homogeneous catalyst was found to undergo self-oxidative degradations, leading to its deactivation and reaching the reaction equilibrium after 750 epoxidation turnovers. On the other hand, the heterogeneous

framework can last for 2150 turnovers without deactivation. This result demonstrates that the heterogeneous MOF catalyst has a superior stability than its ligand component.

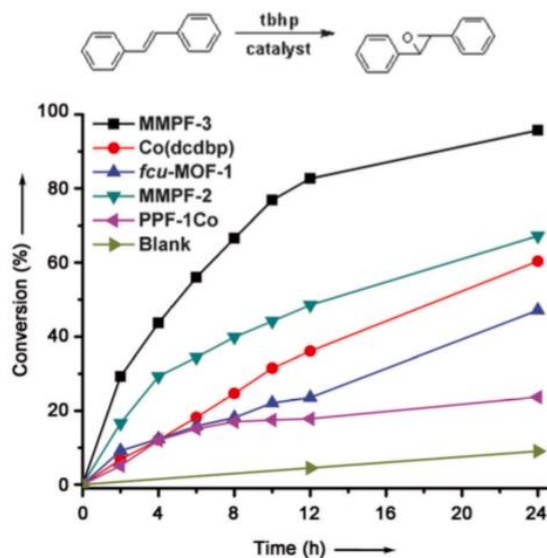


Figure 14. Kinetic traces of trans-stilbene epoxidation catalyzed by heterogeneous MMPF-3, homogenous Co(dcdpb), fcu-MOF-1, PPF-1Co, and in the absence of catalyst²⁹

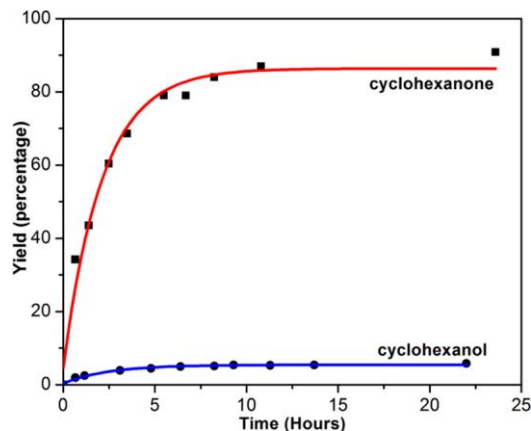


Figure 15. Catalytic oxidation of cyclohexane over Zr-PCN-221(Fe) at 65 °C. The curves are to guide the eye and do not fit to the data³⁷

Zhou and co-workers have explored the catalytic oxidation of cyclohexane using PCN-221 (Fe), a zirconium based metalloporphyrin framework.³⁷ In the presence of tbbp (oxidant), the reaction led to an almost quantitative conversion of cyclohexane into its oxidation products. PCN-221 (Fe) afforded high selectivity for cyclohexanone (yield of 86.9%) over cyclohexanol (yield of

5.4%). These results are ascribed to the high density of available Fe(III) centers on the pore surfaces of PCN-221 (Fe).

1.3.2.2 Lewis acid catalysis

ZnPO-MOF(Zn) is a robust framework prepared using the pillared-layer strategy, featuring Zn(II)dipyridylporphyrin pillars and tertratopic carboxylate struts.²⁶ It has large pores with a surface area of ~500 m²/g. The accessible Zn(II) sites incorporated on the surface demonstrate excellent catalytic activity for an acyl-transfer reaction between N-acetylimidazole and 3-pyridylcarbinol. In comparison to the uncatalyzed reaction, the reaction rate is enhanced 2420 times. The remarkable catalytic activity of ZnPO-MOF(Zn)MOF is credited to the Lewis acidic Zn(II) centers that provide coordination sites to substrates and assist in pre-concentrating reactant molecules in MOF channels.

The capture and sequestration of CO₂ is a novel method aimed at mitigating the high levels of atmospheric CO₂. It involves efficient chemical conversion of CO₂ into desirable and economically useful products. Notably, there has been an increased interest in the synthesis of cyclic carbonates via coupling of epoxide with CO₂. Cyclic carbonates have wide applications in pharmaceutical and fine-chemicals industry. Zhou and co-workers have shown that PCN-224(Co) can act as a heterogeneous Lewis acid catalyst in the presence of additives for the production of cyclic carbonates from CO₂ and epoxides at 100 °C under 2 MPa pressure (Fig. 16).³⁶ PCN-224 (0.1 mol% loading) yielded 42% conversion after 4 hours of reaction time and demonstrated recyclability after three consecutive runs.

Concentrating Lewis acid sites in confined, accessible pores can promote strong interactions with the substrate, which in turn promotes catalytic processes. Ma and co-workers executed this strategy using the MMPF-9 framework, comprising of an octatopic porphyrin ligand

Cu(II)5,10,15,20-tetrakis(3,5-dicarboxyphenyl) porphyrin (tdcbpp) and copper paddlewheel SBUs.³⁸ It is a channeled structure featuring a high density of Cu(II) sites within the confined nanospace. The high density of open copper sites renders MMPF-9 as a highly efficient heterogeneous catalyst for chemical fixation of CO₂ with epoxides at room temperature under 1 atm pressure, yielding 87.4% product in 48 hours (Table 1). Ambient reaction conditions not only provide an opportunity to decrease the cost of CO₂ fixation but also pave the way for development of greener synthetic methods.

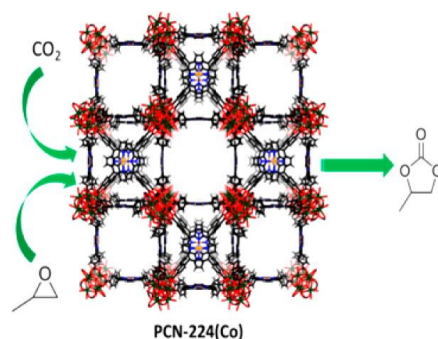


Figure 16. Schematic showing PCN-224(Co) catalyzing a coupling reaction between CO₂ and epoxide³⁶

Entry	Epoxides	Products	Yield (%)
1 ^a			87.4
2 ^b			49.2
3 ^a			80.3
4 ^a			30.5
5 ^c			65.9
6 ^a			29.7
7 ^d			86.4

^a Reaction conditions: epoxide (25 mmol) with MMPF-9 (0.03125 mmol), *n*-Bu₄NBr (0.58 g), at room temperature under 1 atm CO₂ for 48 hours.

^b The same reaction conditions as those when loaded with HKUST-1 (0.03125 mmol). ^c Reaction time was extended to 96 hours under the similar conditions. ^d The recyclability test of MMPF-9.

Table 1. Different substituted epoxides coupled with CO₂ catalyzed by MOFs at room temperature under 1 atm pressure

1.3.2.3 Photocatalysis

The highly conjugated structures of porphyrins and metalloporphyrins endows them with distinct chromophoric properties and photocatalytic activities in the homogeneous phase. Incorporating them into robust porous MOFs can induce electron transfer reactions, potentially leading to improvements in their chromophoric properties and photocatalytic activities. Porphyrinic MOFs can also be part of integrated assemblies that carry out electron transfer reactions to drive photocatalytic reactions. Rosseinsky and co-workers developed a multi-component system comprising of porphyrin-based MOF/ethylenediaminetetracetic acid(EDTA)/colloidal Pt, to demonstrate hydrogen evolution from water.³⁹ The porphyrin-based material, Zn-Al-PMOF, is obtained from a hydrothermal reaction of AlCl_3 and free-base TCPP ligand, followed by metalation of porphyrin core. It afforded a surface area of $\sim 1400 \text{ m}^2/\text{g}$ and exhibited high thermal and chemical stability. Zn-Al-PMOF serves as an antenna to harvest light and inject electrons from the sacrificial electron donor of EDTA to catalytically active centers of Pt. The multicomponent system shows heterogeneous photocatalytic activity, evolving hydrogen from water in the visible light range (Fig. 17).

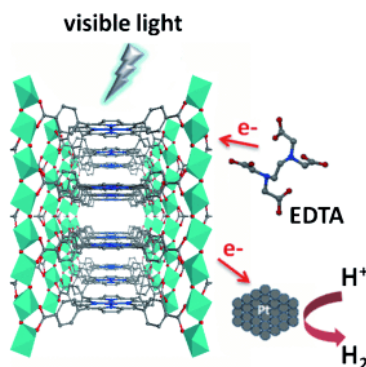


Figure 17. The photocatalytic reaction using Zn inserted Al-PMOF and colloidal Pt

1.3.4 Nano-thin film fabrication

In order to apply MOFs in nanotechnological devices, it is necessary to implement them as thin films. Because of their versatility and functionality, porphyrins present tremendous potential as building blocks of MOF thin films. However, the literature dealing with fabrication of porphyrin/metalloporphyrin MOF thin films is scarce as compared to porphyrinic/metalloporphyrin-based MOFs. The first attempt to fabricate a MOF nano-thin film was made in 2010 by Kitagawa and co-workers. They reported a facile bottom-up fabrication technique for growing a MOF thin film that is preferentially oriented on the surface of the substrate (NAFS-1). The layer-by-layer growth procedure was integrated with the Langmuir–Blodgett method to provide an effective protocol to create crystalline MOF nanofilms and to systematically control the film thickness (Fig. 18).⁴⁵ Synchrotron X-ray surface crystallography was used to demonstrate that the film exhibits highly crystalline order in both the out-of-plane and in-plane orientations with respect to the substrate.⁴⁶

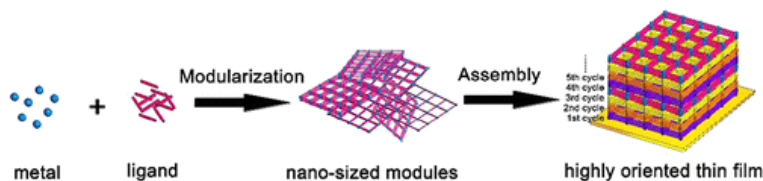


Figure 18. Illustration of the modular assembly process of the MOF nano- thin film

So et al. grew DA-MOFs as thin films on functionalized surfaces using layer-by-layer (LBL) approach.⁴⁷ In the layer-by-layer approach, the self-assembled monolayers (SAM) coated substrate is immersed in a solution of metal precursor (of MOF) followed by immersing it in a solution of organic linker with rinsing in between. The thickness of the film increased systematically with the number of assembly cycles. Polarization excitation and fluorescence measurements indicated that the porphyrin units are preferentially oriented in the MOF film. A far-red emitting squaraine dye (S1), which exhibits a high overlap integral with the DA-MOF, was

deposited onto the surface of the MOF film. Exclusive emission from S1 was observed following selective excitation of Zn-porphyrin units in a 50-cycle film (Fig. 19). These results suggest that the films can be used as antennae for light harvesting and efficient Förster energy transfer is possible within the film, considering the long-distance exciton propagation.

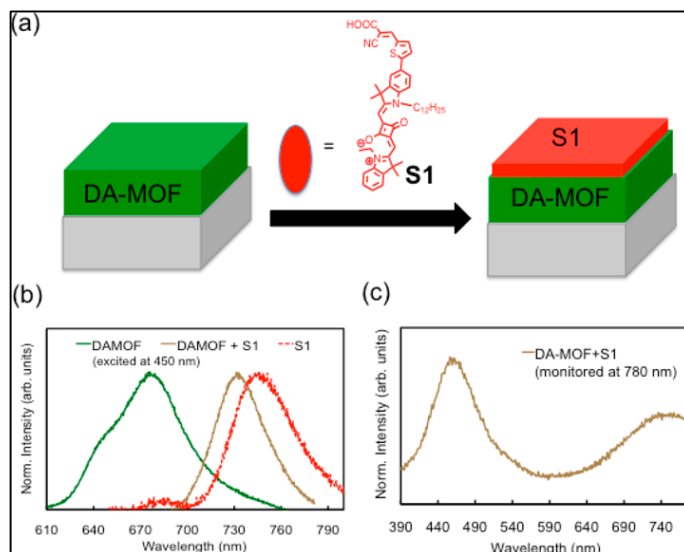


Figure 19. (a) Schematic diagram showing the preparation of a sensitized DA-MOF film. (b) Comparison of emission profiles of DA-MOF (green solid), S1 (red solid), and DA-MOF sensitized with S1 (light-green dotted) upon excitation at 450 nm. (c) Excitation profile of the DA-MOF+S1 film monitored at 780 nm, where the emission from DA-MOF is negligible.

1.4 Conclusion

Porphyrin based frameworks are only a small part of the broad family of MOFs but they have carved out a distinct niche for themselves because of their unique structural features and diverse applications. Although porphyrinic MOFs have demonstrated great potential over the years, more work is required in all domains before these materials can be commercialized. Several challenges dealing with large-scale synthesis and applicability also need to be addressed. In conclusion, the

field of porphyrinic MOFs that emerged more than two decades ago continues to attract interest of both the academia and industry, and should continue to grow in the future.

1.5 References

- (1) Furukawa, H.; Cordova, K. E.; O’Keeffe, M.; Yaghi, O. M. *Science* (80-.). **2013**, *341* (August), 974.
- (2) Vallet-Regí, M.; Balas, F.; Arcos, D. *Angew. Chemie Int. Ed.* **2007**, *46* (40), 7548–7558.
- (3) Horcajada, P.; Serre, C.; Vallet-Regí, M.; Sebban, M.; Taulelle, F.; Férey, G. *Angew. Chemie* **2006**, *118* (36), 6120–6124.
- (4) Horcajada, P.; Chalati, T.; Serre, C.; Gillet, B.; Sebrie, C.; Baati, T.; Eubank, J. F.; Heurtaux, D.; Clayette, P.; Kreuz, C.; Chang, J.-S.; Hwang, Y. K.; Marsaud, V.; Bories, P.-N.; Cynober, L.; Gil, S.; Férey, G.; Couvreur, P.; Gref, R. *Nat. Mater.* **2009**, *9*, 172.
- (5) Garcia-Garcia, P.; Muller, M.; Corma, A. *Chem. Sci.* **2014**, *5* (8), 2979–3007.
- (6) Lee, J.; Farha, O. K.; Roberts, J.; Scheidt, K. A.; Nguyen, S. T.; Hupp, J. T. *Chem. Soc. Rev.* **2009**, *38* (5), 1450–1459.
- (7) Son, H.-J.; Jin, S.; Patwardhan, S.; Wezenberg, S. J.; Jeong, N. C.; So, M.; Wilmer, C. E.; Sarjeant, A. A.; Schatz, G. C.; Snurr, R. Q.; Farha, O. K.; Wiederrecht, G. P.; Hupp, J. T. *J. Am. Chem. Soc.* **2013**, *135* (2), 862–869.
- (8) Lee, C. Y.; Farha, O. K.; Hong, B. J.; Sarjeant, A. A.; Nguyen, S. T.; Hupp, J. T. *J. Am. Chem. Soc.* **2011**, *133* (40), 15858–15861.
- (9) So, M. C.; Wiederrecht, G. P.; Mondloch, J. E.; Hupp, J. T.; Farha, O. K. *Chem. Commun.* **2015**, *51* (17), 3501–3510.
- (10) Farha, O. K.; Özgür Yazaydın, A.; Eryazici, I.; Malliakas, C. D.; Hauser, B. G.; Kanatzidis, M. G.; Nguyen, S. T.; Snurr, R. Q.; Hupp, J. T. *Nat. Chem.* **2010**, *2*, 944.

- (11) Ma, S.; Zhou, H.-C. *Chem. Commun.* **2010**, 46 (1), 44–53.
- (12) Li, J.-R.; Kuppler, R. J.; Zhou, H.-C. *Chem. Soc. Rev.* **2009**, 38 (5), 1477–1504.
- (13) Shubin, V. V.; Karapetyan, N. V.; Krasnovsky, A. A. *Photosynth. Res.* **1986**, 9 (1–2), 3–12.
- (14) H., E. *J. Porphyr. Phthalocyanines* **2000**, 4 (1), 88–102.
- (15) Wagenknecht, H. *Angew. Chemie Int. Ed.* 48 (16), 2838–2841.
- (16) Lo, P.-C.; Leng, X.; Ng, D. K. P. *Coord. Chem. Rev.* **2007**, 251 (17), 2334–2353.
- (17) Sandanayaka, A. S. D.; Ito, O. *J. Porphyr. Phthalocyanines* **2009**, 13 (10), 1017–1033.
- (18) Lane, B. S.; Burgess, K. *Chem. Rev.* **2003**, 103 (7), 2457–2474.
- (19) Han, H.; Hurley, L. H. *Trends Pharmacol. Sci.* **2000**, 21 (4), 136–142.
- (20) Abrahams, B. F.; Hoskins, B. F.; Robson, R. *J. Am. Chem. Soc.* **1991**, 113 (9), 3606–3607.
- (21) Kuan-Jiuh, L. *Angew. Chemie Int. Ed.* **1999**, 38 (18), 2730–2732.
- (22) Kosal, M. E.; Chou, J.-H.; Wilson, S. R.; Suslick, K. S. *Nat. Mater.* **2002**, 1, 118.
- (23) Suslick, K. S.; Bhyrappa, P.; Chou, J.-H.; Kosal, M. E.; Nakagaki, S.; Smithenry, D. W.; Wilson, S. R. *Acc. Chem. Res.* **2005**, 38 (4), 283–291.
- (24) Burnett, B. J.; Barron, P. M.; Choe, W. *CrystEngComm* **2012**, 14 (11), 3839–3846.
- (25) Barron, P. M.; Wray, C. A.; Hu, C.; Guo, Z.; Choe, W. *Inorg. Chem.* **2010**, 49 (22), 10217–10219.
- (26) Shultz, A. M.; Farha, O. K.; Hupp, J. T.; Nguyen, S. T. *J. Am. Chem. Soc.* **2009**, 131 (12), 4204–4205.
- (27) Farha, O. K.; Shultz, A. M.; Sarjeant, A. A.; Nguyen, S. T.; Hupp, J. T. *J. Am. Chem. Soc.* **2011**, 133 (15), 5652–5655.
- (28) Wang, X.-S.; Meng, L.; Cheng, Q.; Kim, C.; Wojtas, L.; Chrzanowski, M.; Chen, Y.-S.;

- Zhang, X. P.; Ma, S. *J. Am. Chem. Soc.* **2011**, *133* (41), 16322–16325.
- (29) Le, M.; Qigan, C.; Chungsik, K.; Wen-Yang, G.; Lukasz, W.; Yu-Sheng, C.; J., Z. M.; Peter, Z. X.; Shengqian, M. *Angew. Chemie Int. Ed.* **2012**, *51* (40), 10082–10085.
- (30) Wang, X.-S.; Chrzanowski, M.; Gao, W.-Y.; Wojtas, L.; Chen, Y.-S.; Zaworotko, M. J.; Ma, S. *Chem. Sci.* **2012**, *3* (9), 2823–2827.
- (31) Burnett, B. J.; Barron, P. M.; Hu, C.; Choe, W. *J. Am. Chem. Soc.* **2011**, *133* (26), 9984–9987.
- (32) Choi, E.-Y.; Wray, C. A.; Hu, C.; Choe, W. *CrystEngComm* **2009**, *11* (4), 553–555.
- (33) Feng, D.; Gu, Z.-Y.; Li, J.-R.; Jiang, H.-L.; Wei, Z.; Zhou, H.-C. *Angew. Chemie Int. Ed.* **2012**, *51* (41), 10307–10310.
- (34) Morris, W.; Voloskiy, B.; Demir, S.; Gándara, F.; McGrier, P. L.; Furukawa, H.; Cascio, D.; Stoddart, J. F.; Yaghi, O. M. *Inorg. Chem.* **2012**, *51* (12), 6443–6445.
- (35) Jiang, H.-L.; Feng, D.; Wang, K.; Gu, Z.-Y.; Wei, Z.; Chen, Y.-P.; Zhou, H.-C. *J. Am. Chem. Soc.* **2013**, *135* (37), 13934–13938.
- (36) Feng, D.; Chung, W.-C.; Wei, Z.; Gu, Z.-Y.; Jiang, H.-L.; Chen, Y.-P.; Darensbourg, D. J.; Zhou, H.-C. *J. Am. Chem. Soc.* **2013**, *135* (45), 17105–17110.
- (37) Feng, D.; Jiang, H.-L.; Chen, Y.-P.; Gu, Z.-Y.; Wei, Z.; Zhou, H.-C. *Inorg. Chem.* **2013**, *52* (21), 12661–12667.
- (38) Gao, W.-Y.; Wojtas, L.; Ma, S. *Chem. Commun.* **2014**, *50* (40), 5316–5318.
- (39) Fateeva, A.; Chater, P. A.; Ireland, C. P.; Tahir, A. A.; Khimyak, Y. Z.; Wiper, P. V.; Darwent, J. R.; Rosseinsky, M. J. *Angew. Chemie - Int. Ed.* **2012**, *51* (30), 7440–7444.
- (40) Liu, Y.; Yang, Y.; Sun, Q.; Wang, Z.; Huang, B.; Dai, Y.; Qin, X.; Zhang, X. *ACS Appl. Mater. Interfaces* **2013**, *5* (15), 7654–7658.

- (41) Fleming, C. N.; Jang, P.; Meyer, T. J.; Papanikolas, J. M. *J. Phys. Chem. B* **2004**, *108* (li), 2205–2209.
- (42) Lee, C. Y.; Farha, O. K.; Hong, B. J.; Sarjeant, A. a; Nguyen, S. T.; Hupp, J.; Hupp, J. T. *Synthesis (Stuttg)*. **2011**, 15858–15861.
- (43) Son, H. J.; Jin, S.; Patwardhan, S.; Wezenberg, S. J.; Jeong, N. C.; So, M.; Wilmer, C. E.; Sarjeant, A. A.; Schatz, G. C.; Snurr, R. Q.; Farha, O. K.; Wiederrecht, G. P.; Hupp, J. T. *J. Am. Chem. Soc.* **2013**, *135* (2), 862–869.
- (44) Liu, J.; Shekhah, O.; Stammer, X.; Arslan, H. K.; Liu, B.; Schüpbach, B.; Terfort, A.; Wöll, C. *Materials (Basel)*. **2012**, *5* (9), 1581–1592.
- (45) Makiura, R.; Motoyama, S.; Umemura, Y.; Yamanaka, H.; Sakata, O.; Kitagawa, H. *Nat. Mater.* **2010**, *9*, 565.
- (46) Motoyama, S.; Makiura, R.; Sakata, O.; Kitagawa, H. *J. Am. Chem. Soc.* **2011**, *133* (15), 5640–5643.
- (47) So, M. C.; Jin, S.; Son, H. J.; Wiederrecht, G. P.; Farha, O. K.; Hupp, J. T. *J. Am. Chem. Soc.* **2013**, *135* (42), 15698–15701.

Chapter 2

Synthesis and defect characterization of pure phase Zr-MOFs based on meso-tetracarboxyphenylporphyrin

INTRODUCTION

Owing to their ordered crystalline structures, wide range of available topologies and the ability to incorporate diverse chemical functionalities, metal-organic frameworks (MOFs) have shown immense potential in a number of applications, including drug delivery,¹⁻³ catalysis,⁴⁻⁷ light harvesting,⁸⁻¹² gas storage¹³⁻¹⁵ and gas separation.¹⁶ Zirconium MOFs based on meso-tetra(4-carboxyphenyl)porphyrin (TCPP) are an important sub-class of the broader family of these materials. The high connectivity and large size of TCPP (~2 nm) assists in generating large pores inside the frameworks, resulting in open mesoporous structures.¹³ Zr-TCPP MOFs consist of a common, periodically repeating building block having a general formula of $[\text{Zr}_6\text{O}_4(\text{OH})_4(\text{P})_3]$, where P denotes the TCPP linkers that connect the octahedral $[\text{Zr}_6\text{O}_4(\text{OH})_4]^{12+}$ nodes. If the D_{4h} symmetric TCPP linkers fully occupy all the available position around Zr_6 cluster, the structure with the highest symmetry should have (4,12)-connected ftw-a topology, reported in MOF-525.²² However, such an arrangement requires the carboxylate groups of the ligand to be coplanar with the porphyrin macrocycle. This constraint forces TCPP to adopt an energetically demanding conformation. To attain linkers in low energy conformation, both the connectivity and the symmetry of Zr_6 clusters have to decrease giving rise to entirely different topologies (Fig. 1).²³ The symmetry reduced TCPP ligands in these networks have a variety of aspect ratios (the ratio of two sides of the ligand) and dihedral angles between the central and peripheral rings.

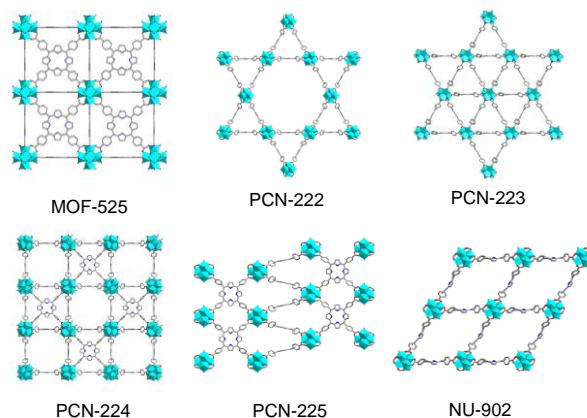


Figure 1. Structures of Zr-MOFs based on meso-tetra(4-carboxyphenyl)porphyrin

Despite exhibiting a diverse variety of structure types, Zr-based TCPP MOFs can be obtained under similar solvothermal reaction conditions, suggesting the lack of a thermodynamically dominant phase. As a result, one-pot syntheses often yield MOF powders containing two or more phases. This behavior reduces the reliability of synthetic procedures and complicates the determination of structure-property relationships. Several strategies for obtaining pure framework phases exist. Solvent-assisted separation of MOF components on the basis of their density difference is one possible approach.²⁴ However, the reported Zr-TCPP MOFs possess similar densities and therefore cannot be separated without substantial loss of material.²⁵ Another strategy is the introduction of seed crystals of the targeted Zr-TCPP polymorph into the synthesis solution.²⁶ Although this method improves the phase-purity of the final product, availability of phase-pure seed crystals of the targeted MOF is a pre-requisite.

A more attractive approach would be to fine tune the reaction parameters to selectively generate the desired structures.²⁷ Similar to other Zr-based MOFs, modulators are typically added during the synthesis of TCPP containing frameworks. Their primary role is to compete with the bridging TCPP linkers for coordination to Zr^{4+} ions, and slow down the rate of crystallization, leading to the formation of highly ordered MOF structures. Furthermore, modulators can act as templating

agents and directly guide the framework assembly. Therefore, the choice of modulator can be a useful handle to control the MOF crystallization process, and in turn direct the phase-purity. Webber et. al. and Islamoglu et. al. have demonstrated that the phase-purity of NU-1000, a related Zr-based MOF comprised of 1,3,6,8-tetrakis(p-benzoic acid)pyrene (TBAPy), can be significantly improved by judiciously selecting a modulator that disfavors the formation of NU-901 byproduct.^{28,29} Another important consideration is the ability of modulator to induce defect sites in Zr-based MOFs.^{30,31} Defects are known to significantly affect the physical and chemical properties of the material, such as porosity, thermal stability, mechanical characteristics, Lewis and Brønsted acidity, catalytic activity and conductivity.³¹⁻³⁶ Therefore, a controlled introduction of defects can allow for straightforward modification of properties of existing frameworks.

To our knowledge, the influence of modulator on the outcome of Zr-TCPP MOF synthesis has received limited attention compared to the UiO series. Keeping this in mind, we decided to perform a systematic exploration of the synthetic parameter landscape (modulator concentration, acidity and chemical properties) to gain deeper insights into the factors governing the formation of these frameworks. From this study, the synthetic conditions that could reliably produce phase-pure Zr-TCPP MOFs were identified. The defectivity of these pristine MOFs was further investigated using a variety of techniques, including ¹H NMR spectroscopy, thermogravimetric analysis (TGA), inductively coupled plasma mass spectrometry (ICP-MS) and N₂ gas sorption.

EXPERIMENTAL SECTION

Materials: All the chemicals were purchased from commercial suppliers and used as received. Meso-tetra(4-carboxyphenyl)porphyrin (>97%) was purchased from Frontier Scientific. Zirconium chloride (anhydrous, ≥99.5%), formic acid (FA, ≥95%), 4-chlorobenzoic acid (CBA, 99%) were purchased from Sigma-Aldrich. *N,N'*-dimethylformamide (DMF, spectrophotometric

grade, $\geq 99.9\%$) and glacial acetic acid (AA, ACS certified, 99.7%) were purchased from Fisher chemical. Trichloroacetic acid (TCA, $>99\%$), hexanoic acid (HA, $>98\%$), decanoic acid (DA, $>98\%$), myristic acid (MA, $>99\%$) and stearic acid (SA, $>98\%$) were purchased from TCI. Propionic acid (PA, 99%), trimethylacetic acid (TMA, 99%), trifluoroacetic acid (TFA, 99%), benzoic acid (BA, 99%), 4-nitrobenzoic acid (NBA, 99%) were purchased from Alfa Aesar. Chloroacetic acid (CAA, 99%) was purchased from Acros organics. Difluoroacetic acid (DFA), 2,6-difluorobenzoic acid (DFBA), pentafluorobenzoic acid (PFBA) and 4-methoxybenzoic acid (MBA) were received from Oakwood chemicals. Deuterated DMSO (DMSO- d_6 , 99.9%) was purchased from Cambridge Isotope Laboratories, Inc.

MOF Synthesis: 10 mg of H_4TCPP (1.265×10^{-5} mol) and 7 mg of $ZrCl_4$ (3.01×10^{-5} mol) were added to 10 ml DMF in a 6-dram vial and dissolved with the aid of ultrasonication. Modulator was then added to the vial, which was further sonicated to get a homogeneous reaction mixture. The vials were placed in an oven at 120 °C for 16 hours. After allowing them to cool down to room temperature, the resultant MOF powder was collected by centrifugation. It was washed 3 times with DMF and then soaked in ethanol for 3 days with fresh ethanol replacement every day. The MOFs were dried at room temperature and then activated by heating at 100 °C under vacuum.

Powder X-Ray diffraction (PXRD): A 600 W Rigaku MiniFlex powder diffractometer with a $CuK\alpha$ (0.15418 nm) radiation source was used, with a sweeping range of 2–25° in continuous scanning mode. PXRD traces were collected in 0.05° increments at a scanning rate of 0.2°/min.

Scanning electron microscopy (SEM): SEM samples were prepared by suspending MOF powders in ethanol with sonication. The resulting suspensions were drop-casted on pre-cut glass slides. After drying, the glass slides were mounted on SEM sample pegs with the help of double-sided copper tape. The sides of the glass slides and the platform of sample peg were coated with

conductive carbon paint purchased from Electron Microscopy Sciences. A LEO (Zeiss) 1550 field-emission scanning electron microscope, equipped with an in-lens detector, operating at 5.0 kV was used to obtain high-resolution images of the MOF particles.

¹H NMR analysis: The measurements were conducted using the Agilent U4-DD2 400 MHz spectrometer. A 15-25 mM solution of the 3-(trimethylsilyl)propionic-2,2,3,3-d₄ acid sodium salt (TMSP) was prepared in DMSO-d₆ (*ca.* 10 mg mL⁻¹). 700 μL of this solution was added to a micro-centrifuge tube containing 1.5-2 mg of MOF. A drop of concentrated sulfuric acid (98%) was added to this mixture and the tube was sonicated to digest the framework. The content of the tube was quantitatively transferred to an NMR tube that was again sonicated and heated at 80 °C for 30 minutes to ensure complete digestion.

Thermogravimetric analysis (TGA): A Q-series thermogravimetric analyzer from TA Instruments was used to assess the thermal stability and defectivity of MOFs. Samples weighing ~3-5 mg were placed on a platinum pan and heated under air at a rate of 5 °C/min over the temperature range of 25–800 °C.

Gas adsorption isotherms: The N₂ adsorption measurements were conducted using a Micromeritics 3Flex instrument. A 6 mm large bulb sample cell was used to hold the samples and was degassed under vacuum at a temperature of 100 °C for 24 h. The surface area of the MOFs was determined from the N₂ adsorption isotherms at 77 K by fitting the adsorption data within the 0.05–0.3 P/P₀ pressure range to the BET equation.

Inductively Coupled Plasma Mass Spectrometry (ICP-MS): The MOF samples were digested in 70% nitric acid and heated at 90 °C for 1 h. The resulting solution was diluted with deionized water so that the final concentration of nitric acid was 7% by volume. The samples were

analyzed for zirconium content using a Thermo Electron X-Series ICP mass spectrometer in accordance with Standard Method 3125-B.

RESULTS AND DISCUSSION

Synthesis of Zr-TCPP MOFs was achieved by dissolving 3.01×10^{-5} mol of $ZrCl_4$ and 1.26×10^{-5} mol of TCPP in 10 mL DMF along with desired amounts of modulator. The mixture was sonicated for 15 minutes then the vial was placed in an oven and heated at 120 °C for 16 hours. The resulting polycrystalline MOF powders were isolated by centrifugation, washed with DMF and ethanol and finally, dried under vacuum. The modulators under investigation were based on monocarboxylic acid species and were loosely divided into three classes, namely small aliphatic modulators, aromatic modulators and long chain modulators. The concentration of modulators was varied, ranging from 10 to 6000 equivalents ($[Modulator]/[TCPP]$), depending on their acidity, and solubility in the synthesis solvent. Other factors affecting the MOF synthesis, such as reaction temperature, time, solvent, solvent volume, precursor concentration, order of addition and reaction apparatus were kept constant. PXRD patterns of Zr-TCPP MOFs simulated from single crystal X-ray diffraction data served as reference standards for phase identification of resulting powders. Routine interpretation of powder patterns is often limited to a qualitative visual comparison of the peak positions and relative peak intensities of experimental and simulated patterns. Fig. 2a shows an example PXRD pattern of a mixed-phase MOF powder and the contributions from each component. However, visual analysis of diffraction peaks underutilizes the available information, and can lead to incorrect conclusions about the phase composition of reaction product. Quantitative estimation of phase composition is therefore important for elucidation of factors governing the formation of Zr-TCPP frameworks. Fitting the sum of individual pure phase patterns to the experimental data is an effective method to determine the abundance of each phase in the MOF

sample.³⁷ This approach relies on the additive nature of crystalline components of the powder pattern. Therefore, the experimental powder patterns were fit to a linear combination of pure phase patterns (Equation 1)

$$\vec{Y} = a\vec{X}_1 + b\vec{X}_2 + c\vec{X}_3 \dots \dots \dots \quad (1)$$

where \vec{Y} is the column vector representing the observed pattern, \vec{X}_n are the column vectors representing pure phase patterns and the scalars (a, b, c...) give the relative abundance of each phase. Equation 1 was represented in a matrix form and the coefficient matrix was calculated with the help of GNU-Octave software. Fig. 2b shows an example of the fitted pattern of a mixed phase MOF sample overlaid on its observed pattern. Both patterns are in good agreement, which indicates that the phase composition obtained from the quantitative analysis is reasonably accurate. The percentage contribution of each component is reported in Fig. 2b. Similar analysis was performed on other crystalline MOF samples.

In addition, SEM characterization was carried out as a second method to explore phase-purity of the MOF samples. The Zr-TCPP polymorphs exhibit distinctly different morphologies, which can be easily discerned through visual analysis of the SEM images. While SEM imaging is qualitative in nature, it is particularly useful for detecting small amounts of phase impurities that might be overlooked in the PXRD analysis. Fig. 3(Left) shows a representative SEM image of a phase-pure sample with small bean-shaped particles (length $\sim 2 \mu\text{m}$). All MOF particles are morphologically identical and are similar in size. In contrast, Fig. 3(Right) shows the SEM image of a mixed-phase sample, where distinctly different morphologies corresponding to different framework components are clearly visible.

After completing phase characterization of MOFs, the data was compiled into three screening plots, one for each of the modulator series. These plots depict the change in the phase composition

as a function of modulator concentration and chemical properties (acidity or chain length), from which trends could be straightforwardly identified. For example, the screening plot for small aliphatic acids is dominated by PCN-222 and PCN-223 frameworks, with PCN-224 and MOF-525 phases found as minor impurities in some cases (Fig 4a). From these results, reaction conditions that are able to produce pure phase PCN-223 (propionic acid) and PCN-222 (difluoroacetic and formic acids) were discovered. When long chain saturated carboxylic acids were employed, the dominating component in the powder patterns changed compared to small aliphatic modulators. Under these conditions, MOF-525 was found to crystallize preferentially (Fig 4b). Pure phase MOF-525 samples were obtained with myristic acid (MA) and stearic acid (SA). On the other hand, the aromatic modulator series was peculiar in the sense that crystalline MOF powders could only be obtained within a narrow region of modulator acidity and concentration. All the reactions in this series yielded mixed-phase powders (Fig 4c).

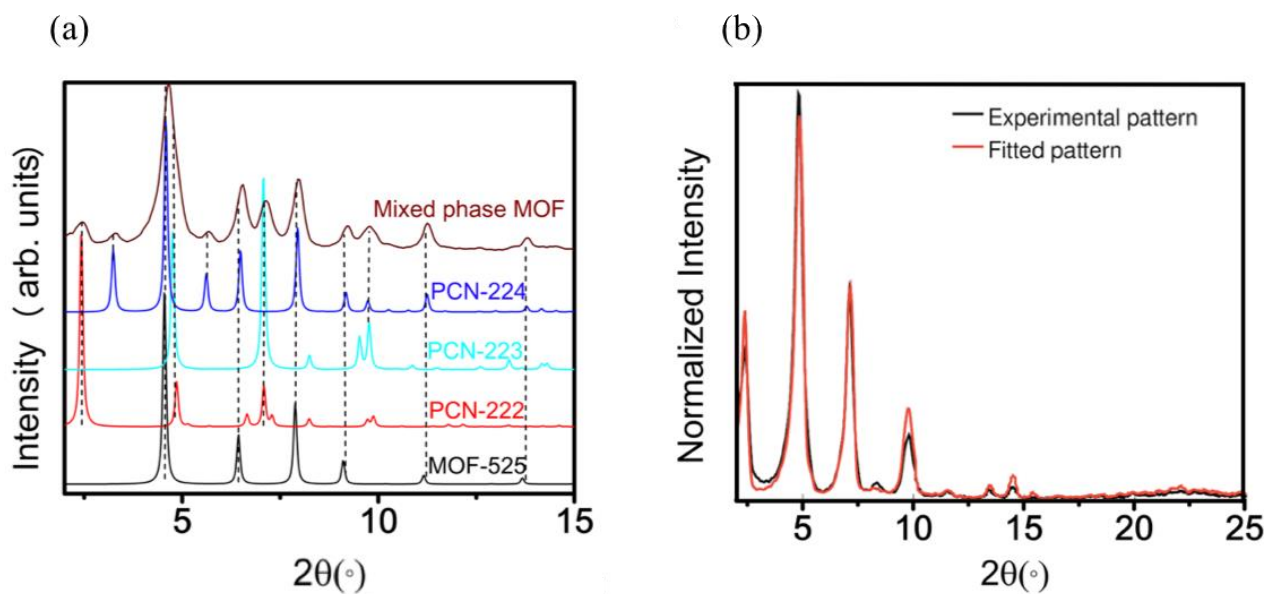


Figure 2. (a) Visual analysis of the phase composition of a mixed-phase MOF sample. (b) Comparison of experimental and fitted patterns of a mixed-phase MOF sample. The fit indicates that this sample consists of 38% PCN-222 component and 62% PCN-223 component.

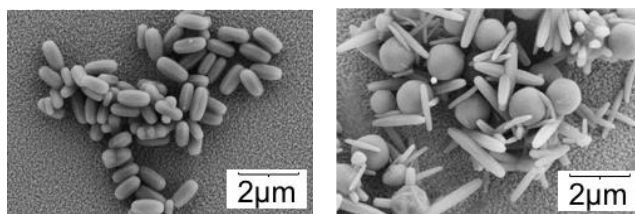
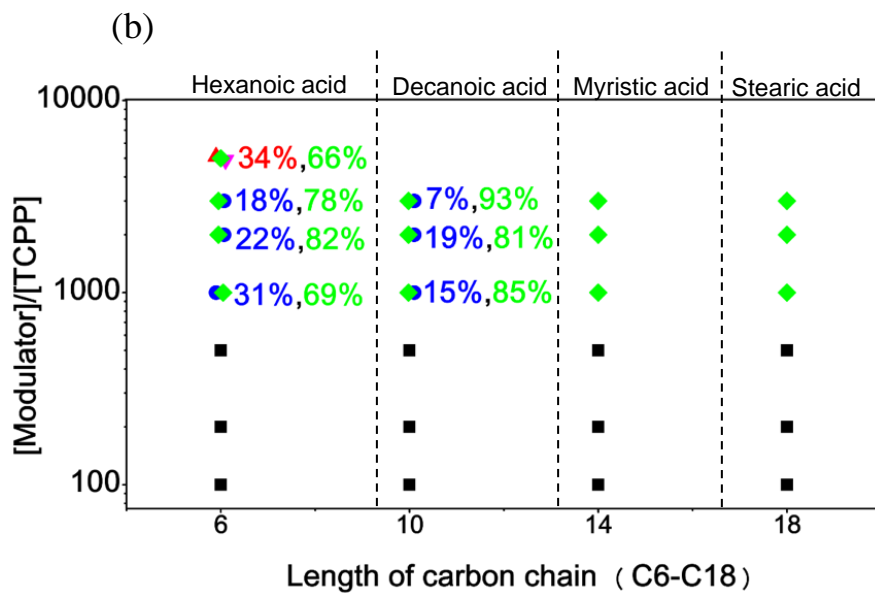
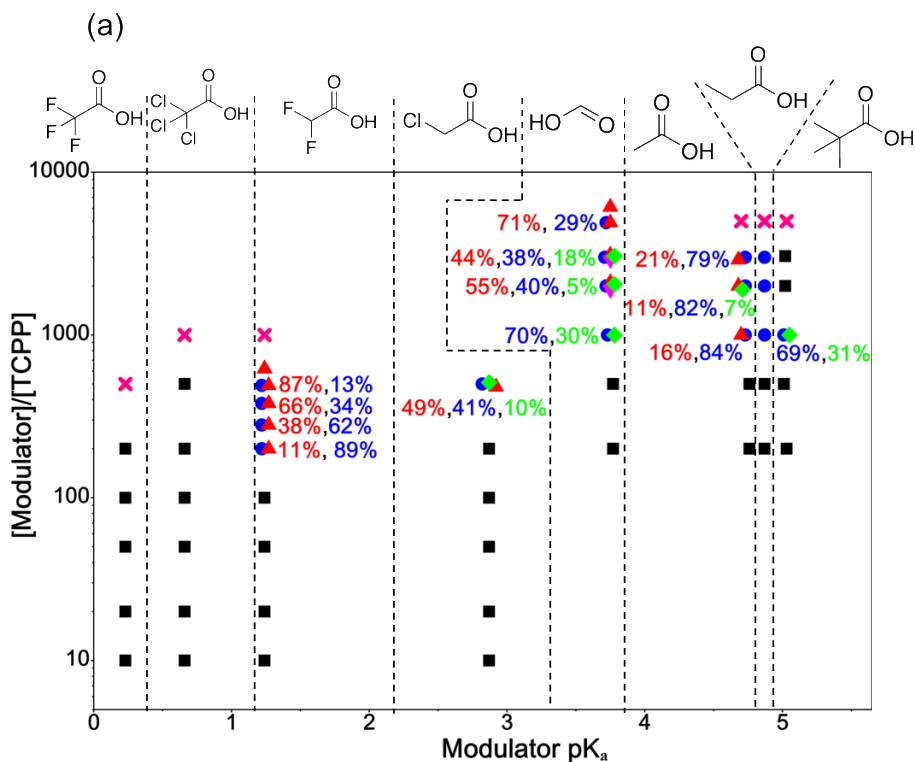


Figure 3. Left: SEM image of a phase-pure MOF. All particles have the same morphology Right: SEM image of a mixed-phase MOF.

The screening plots also depict trends that relate the relative concentrations of modulator and linker ($[\text{Modulator}]/[\text{TCPP}]$ ratio) to the crystallinity of MOFs. For instance, reactions with low $[\text{Modulator}]/[\text{TCPP}]$ ratio yielded poorly crystalline MOF powders of uncertain phase composition. The crystallization and precipitation of MOFs in this case is rapid and uncontrolled, which resulted in the formation of poorly defined, largely amorphous material. Increasing the $[\text{Modulator}]/[\text{TCPP}]$ ratio was found to dramatically improve the crystallinity of MOF powders. Higher modulator concentration slows down the coordination reactions and inhibits the framework assembly, allowing for structural error correction and improving the overall crystallinity. The screening plots also revealed the existence of an upper limit on $[\text{Modulator}]/[\text{TCPP}]$ ratio, beyond which MOF formation does not take place. Using modulators in large excess prevented the MOF nuclei from attaining the critical size and growing into crystals that precipitate out of synthesis solution. Therefore, crystalline MOF powders can only be obtained within a finite range of $[\text{Modulator}]/[\text{TCPP}]$ ratio. Low crystallinity powders are obtained below this range and no MOF precipitation occurs above it. It is also worth noting that as the acidic strength of modulator increased, the working $[\text{Modulator}]/[\text{TCPP}]$ ratio range narrowed down and shifted to lower values. For example, weakly acidic modulators like DA, MA, and SA produced crystalline MOFs in a very broad range of $[\text{Modulator}]/[\text{TCPP}]$ ratio (1000 to 3000). In fact, the upper limit in this case was restricted by the physical amount of the modulator which could be fit into the reaction

vessel. On the other hand, strongly acidic modulators like DFA, CAA, and NBA produced crystalline MOFs in a more narrow range of [Modulator]/[TCPP] ratio (500 to 1000).



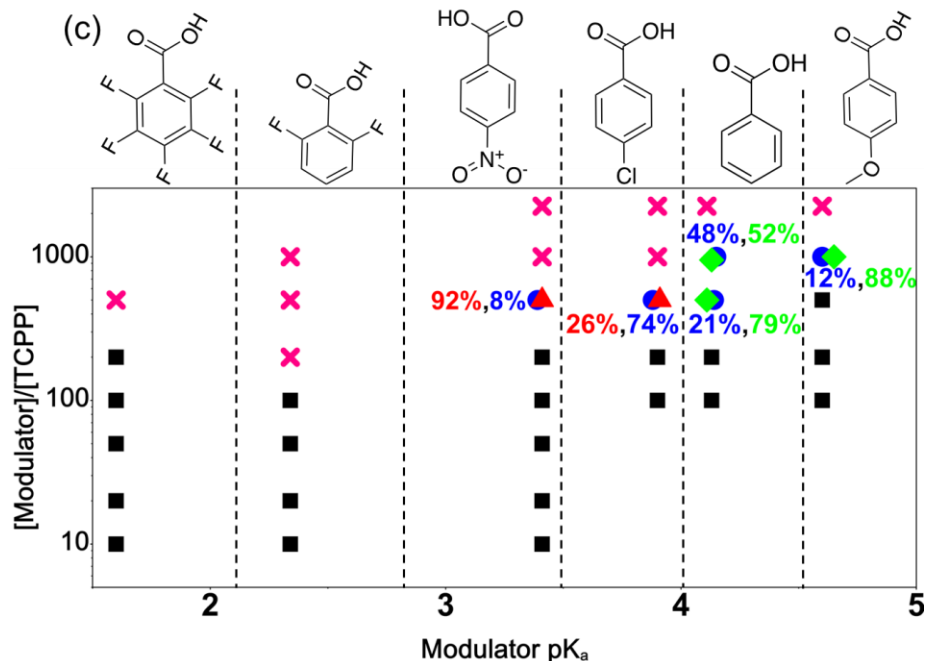


Figure 4. (a) Screening plot for small aliphatic modulators. The modulators along with their respective pK_a values are – trifluoroacetic acid (0.23), trichloroacetic acid (0.66), difluoroacetic acid (1.24), chloroacetic acid (2.87), formic acid (3.77), acetic acid (4.76), propionic acid (4.87) and trimethylacetic acid (5.03). (b) Screening plot for long chain modulators. Modulators used in this series were hexanoic acid (C6), decanoic acid (C10), myristic acid (C14) and stearic acid (C18). (c) Screening plot for aromatic modulators. The modulators along with their respective pK_a values are – pentafluorobenzoic acid (1.6) 2,6-difluorobenzoic acid (2.34), 4-nitrobenzoic acid (3.41), benzoic acid (4.11) and 4-methoxybenzoic acid (4.47). The pK_a values of modulators used for the construction of screening plots are for aqueous media (for qualitative analysis of phase distribution). PCN-224 was obtained only in trace amounts and its percentage contribution to phase composition analysis is not included. Legends: square (black) – low crystallinity powder, circle (dark blue) – PCN-223, triangle (red) – PCN-222, inverted triangle (magenta) – PCN-224, rhombus (green) – MOF-525, cross (pink) – no precipitate.

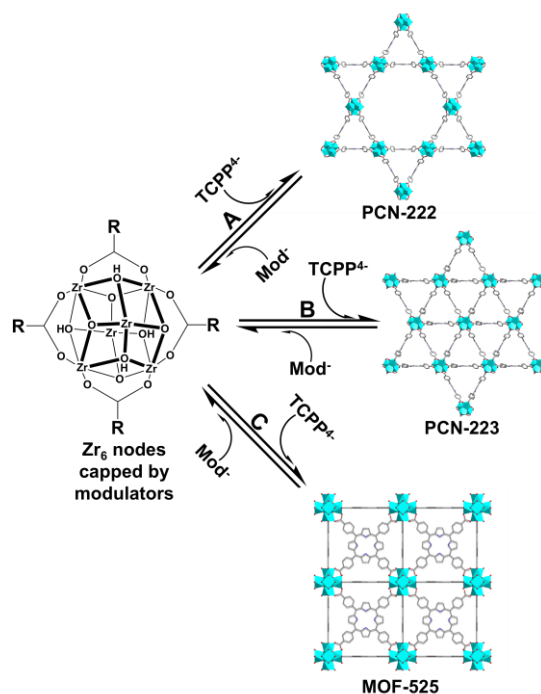
The conditions of the MOF formation reaction, such as temperature, $[\text{Modulator}]/[\text{Ligand}]$ ratio, and the allotted reaction time, determine which reaction pathway is favored: either the thermodynamically controlled or the kinetically controlled one.³⁸ If these competing reaction pathways lead to different products, then the composition of the resultant MOF powder is

dependent on whether the reaction is under thermodynamic or kinetic control. Therefore, the reaction conditions mentioned above influence the selectivity of the reaction. The modulator screening study offers an opportunity to investigate the effect of [Modulator]/[Ligand] ratio on Zr-TCPP polymorph selectivity during the synthesis (temperature and time were kept constant for all reactions conducted in this study). Since PCN-222, PCN-223, and MOF-525 are the predominant products observed in the modulator screening study, the scope of this discussion will be limited to these three polymorphs. It is worth noting that a Zr-TCPP MOF reaction solution consists of Zr^{4+} salt, TCPP ligand with varying degree of protonation ($TCPP^{n-}$, $n = 0-4$), protonated modulator (Mod), and deprotonated modulator (Mod^-). Out of these, only the fully deprotonated ligand molecules and deprotonated modulator molecules are directly involved in the coordination. The ratio of the concentrations of deprotonated modulator and fully deprotonated TCPP ($[Mod^-]/[TCPP^{4-}]$) is therefore a better descriptor of the coordination environment during the MOF formation process.

The magnitude of $[Mod^-]/[TCPP^{4-}]$ ratio depends on the nature and concentration of modulator. For instance, strongly acidic modulators afford very high $[Mod^-]/[TCPP^{4-}]$ ratio since they dissociate to a larger extent, furnishing a greater concentration of deprotonated species. Furthermore, they shift the equilibrium towards the protonated form of the ligand, lowering the concentration of $TCPP^{4-}$. If the $[Mod^-]/[TCPP^{4-}]$ is very high, then equilibria A, B and C in scheme 1 are shifted in favor of the incorporation of modulator into the pre-nucleation MOF clusters (molecular aggregates formed prior to nucleation). This prevents the clusters from growing and attaining the critical size of nucleation. Consequently, the less stable clusters break down and dissolve in synthesis solution. The stable ones, on the other hand, have a higher probability of surviving and growing into nuclei. Thus, very high $[Mod^-]/[TCPP^{4-}]$ ratio can be expected to favor

formation of the most stable polymorph. Typically, the most stable polymorph is the thermodynamically favored product. The observed phase composition of MOFs prepared using strongly acidic modulators like DFA, FA and NBA indicate that PCN-222 is the most stable polymorph and therefore, the thermodynamically favored product of the reaction between Zr^{4+} and TCPP.

Scheme 1. Representation of the equilibria governing the formation of Zr-TCPP polymorphs (TCPP⁴⁻ = fully deprotonated ligand and Mod⁻ = deprotonated modulator (RCOO⁻))



The samples synthesized in the presence of DFA and FA (Fig. 3a) show a gradual increase in the proportion of PCN-222 phase as the concentration of modulator (Mod) is increased. Similarly, the crystalline phase obtained in the NBA series is also predominantly PCN-222 framework. Intermediately strong acids like AA, PA and CBA dissociate to a lesser extent and yield a lower $[Mod^-]/[TCPP^{4-}]$. When they were employed as modulators, the major product of the MOF synthesis is PCN-223. On lowering the $[Mod^-]/[TCPP^{4-}]$, the MOF assembly and crystal growth process is expected to proceed faster and the reaction between Zr^{4+} and TCPP is governed by

kinetics. Thus, PCN-223 can be considered as a kinetically favored product. Interestingly, Feng et al. also reported that shortening the reaction time and adding less or weaker modulator leads to the preferential formation of PCN-223 over PCN-222.¹⁸ Weakly acidic modulators, such as MBA, DA, MA and SA facilitate the formation of MOF-525. Since $[\text{Mod}^-]/[\text{TCPP}^{4-}]$ is too low in this case, we propose that MOF-525 is the most kinetically favored product of the reaction between Zr^{4+} and TCPP. According to Ostwald's rule of stages, the rate of formation of less stable polymorphs is usually higher than that of the most stable polymorph.^{39,40} Since MOF-525 has an energetically demanding structure, it possibly forms at a much faster rate than PCN-222 and PCN-223.

DEFECT CHARACTERIZATION

Defects in the framework structure can influence the surface areas, catalytic activities, and mechanical and thermal stabilities of pristine MOFs.^{30,31,41,42} A controlled introduction of defects can therefore be used to tailor the framework properties for desired applications. It has been demonstrated that by varying the acidity and/or concentration of the modulator, the defectivity of Zr-based MOFs can be systematically tuned.³³ High concentrations of strongly acidic modulators (with pK_a lower than that of ligand) typically afford MOF structures with high defect concentrations.^{32,33,43} This behavior is attributed to the ability of strongly acidic species to outcompete the ligand for the coordination to Zr_6 clusters. Consequently, the resultant framework might contain modulator terminated metal nodes leading to a more defective structure. To probe this behavior in Zr-TCPP frameworks, the defect chemistry of phase-pure MOFs obtained from the screening study, namely DFA-600 (PCN-222), FA-6000 (PCN-222), PA-2000 (PCN-223), MA-3000 (MOF-525) and SA-3000 (MOF-525), was investigated. The sample nomenclature was

derived from the name and modulator equivalents used in the synthesis, for example, DFA-600 refers to a MOF prepared using 600 equivalents of DFA.

To correlate linker deficiency with the structure defectivity, molecular formulae of the MOFs and the total modulator to ligand molar ratio in the framework ($[\text{Modulator}]/[\text{Ligand}]$) were calculated.^{31,42} The first parameter describes the overall defectivity of MOF structure and can be calculated from TGA data. $[\text{Modulator}]/[\text{Ligand}]$, on the other hand, only quantifies modulator-terminated defects and is obtained from ^1H NMR analysis. The interpretation of this value can be complicated by the presence of defect sites that are terminated by other species or trapped modulator molecules inside the pores of the framework. In addition to these parameters, Zr recovery from digested MOF samples can provide valuable information about metal deficiency and the nature of defect sites. Two types of defects are known to exist in Zr-based MOFs: missing linker defects and missing cluster defects. In the latter case, the entire $[\text{Zr}_6\text{O}_4(\text{OH})_4]^{12+}$ node and all the surrounding linkers are removed. Zirconium deficiency is associated exclusively with missing cluster defects, whereas the linker deficiency is influenced by either of the two types of defects. Therefore, zirconium amount in the MOF sample can be directly correlated with concentrations of missing cluster defects. The ratio of experimental zirconium concentration (obtained from ICP-MS) and theoretical zirconium concentration (based on ideal structure of MOF) gives the zirconium recovery of the MOF sample.

BET surface area analysis of MOFs has demonstrated that structural incorporation of modulators into the defective structures could lead to an increase in surface area and average pore size.^{44,45} As a result, these quantities can be utilized to compare defect concentrations in MOFs prepared under different conditions. Surface areas and pore size distributions of the phase pure MOFs obtained

from the screening study were also compared with those reported in the literature, described by the %SA_{difference} parameter (Table 1).

The %linker deficiencies of the two pure phase PCN-222 MOFs (DFA-600 and FA-6000) revealed that their structures were highly defective with almost 25% linkers missing per cluster (~2 out of the expected 8 positions around Zr₆ cluster that are typically occupied by TCPP) (Fig. 6a). Both TGA and ¹H NMR based methods determined similar defect levels for the two frameworks. This result correlates well with other Zr-based MOFs where strongly acidic modulators also led to increased concentration of defects. Furthermore, both DFA-600 and FA-6000 were found to be deficient in zirconium, which indicates the presence of missing cluster defects in these samples (Fig. 6c). Interestingly, Lillerud and co-workers also proposed that missing cluster defects are the predominant defect type in UiO-66 MOFs prepared using DFA and FA as modulators.³³ The N₂ uptake capacity (and thus the porosity) of DFA-600 and FA-6000 was comparable between the two samples, with small differences in BET surface area and pore size distribution (Table 1). Upon comparing all the experimental parameters used to describe defectivity, it can be concluded that DFA-600 and FA-6000 frameworks display high degree of similarity in the nature and concentration of their defects. Although DFA is more acidic than FA, the concentration of the latter (6000 equivalents) used in reaction was much higher than DFA (600 equivalents) affording comparable defectivities of the resultant MOFs.

PA-2000 (pure phase PCN-223) was relatively less defective than DFA-600 and FA-6000 with only 10% linkers missing per cluster (~1 out of 12 positions around Zr₆ cluster) (Fig. 6a). Interestingly, the [Modulator]/[Ligand] ratio in PA-2000 was unusually high and overestimated its defect concentrations (Fig. 6b). This effect may be attributed to residual modulator trapped inside the pores that was not removed during the activation procedure. Another explanation for such

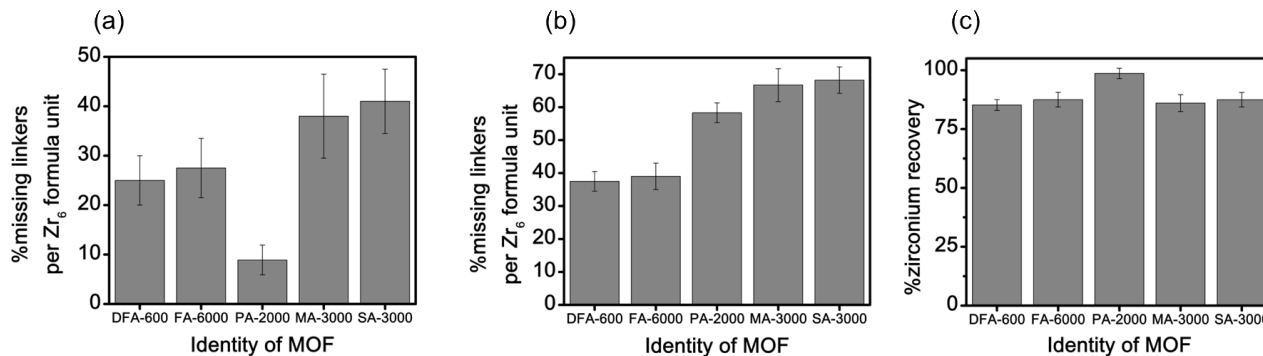


Figure 6. (a) %missing linkers per Zr₆ formula unit of phase pure MOFs calculated from TGA (DFA-600 and FA-6000) or a combination of TGA and ¹H NMR (PA-2000, MA-3000 and SA-3000) experiments. (b) %missing linkers per Zr₆ formula unit of phase pure MOFs obtained from [Modulator]/[Ligand]. TGA and ¹H NMR analysis was conducted on three samples of each of the phase-pure MOFs to calculate the standard deviations. (c) %zirconium recovery of the phase-pure MOFs. Three samples of each of the phase-pure MOFs were digested in nitric acid and zirconium content analyzed with the help of ICP-MS.

Table 1. Comparison of BET surface areas and pore sizes of MOFs prepared in this study with the MOFs reported in literature.

MOF	SA _{Exp} (m ² /g) experimental	SA _{Lit} (m ² /g) literature	%SA _{diff.} $\frac{SA_{Exp} - SA_{Lit}}{SA_{Lit}}$	Average pore sizes (nm) experimental	Average pore sizes (nm) literature
DFA-600	2380	2312*	2.94%	0.9 and 3.9	0.8 and 3.6
FA-6000	2436	2312*	5.36%	0.9 and 3.4	0.8 and 3.6
PA-2000	1809	1600*	13.06%	1.2	1.1
MA-3000	2012	2620**	-23.20%	1 and 1.87	1.1 and 2.0
SA-3000	1581	2620**	-39.65%	1 and 1.75	1.1 and 2.0

* BET surface areas obtained from N₂ adsorption isotherms at 77 K

** BET surface area obtained from Ar adsorption isotherms at 87 K

anomalous behavior could be that reaction by-products, like zirconium propionate contribute to the increased propionic acid concentrations measured by ¹H NMR analysis and skew the [Modulator]/[Ligand] ratio. PA-2000 samples yielded almost quantitative zirconium recovery,

suggesting that the missing cluster defects are largely absent in this framework (Fig. 6c). AA, which is similar to PA in terms of pK_a and chain length, has been shown to selectively induce missing linker point defects in azobenzene-based UiO MOF.^{33,43} Hence, it is reasonable to conclude that defects in PA-2000 framework are predominantly missing linker point defect.

The most surprising behavior however, was observed for long-chain weakly acidic modulators, such as MA and SA. Both of them resulted in the formation of phase pure MOF-525 samples (MA-3000 and SA-3000) that were highly defective with 40% linkers missing per cluster (~5 out of 12 positions around Zr_6 cluster) (Fig. 6a). Considering that MA and SA are not fully miscible with the reaction solvent, and bulkier than other modulators, the formation of highly defected MOF structures suggests that these factors play the dominant role in inducing defects in this case. Missing cluster defects may be prevalent in these MOFs, as evidenced by the decreased zirconium recovery (Fig. 6c). BET surface areas and pore size distributions of MA-3000 and SA-3000 were significantly different from those reported in literature for MOF-525 (Table 1). The %SA_{difference} for MA-3000 and SA-3000 was found to be -23.20% and -39.65% respectively. Bulky MA and SA molecules that are trapped in the pores or bound to Zr_6 clusters can partially block the access to the MOF interior, resulting in a pore blockage defect.^{43,44} This effect can cause reduction in the surface area accessible for adsorption and lower the effective diameters of the octahedral and cubic pores found in MOF-525

To sum up, modulator concentration and acidity play a central role in determining the concentration and nature of defects in Zr-TCPP MOFs. However, for long-chain weakly acidic modulators, miscibility and steric effects have to be taken into consideration. As seen in the case of MA-3000 and SA-3000 frameworks, miscibility and/or steric effects can significantly impact the defect chemistry of Zr-TCPP MOFs, promoting missing cluster defects and pore blockage. The

mechanism by which the steric effects and miscibility of modulator in DMF (reaction solvent) alters the defect chemistry of MOFs is not fully understood. We postulate that if there is a significant polarity difference between the solvent and modulator (as is the case with MA and SA), then the modulator can also function as a co-solvent and interfere in the crystal growth process. Both MA and SA are also sterically demanding modulators, and it is possible that they obstruct crystallization of the ideal MOF-525 structure, leading to more defects.

CONCLUSION

Facile synthesis of phase-pure Zr-TCPP MOFs is a challenge as they are susceptible to polymorphism. Syntheses of these frameworks often result in phase mixtures and have poor reproducibility. To address this issue, a modulator screening study to identify reaction parameters required for the synthesis of phase-pure Zr-TCPP MOFs was conducted. A variety of modulators with diverse structures and wide-ranging acidity (pK_a) were tested. Reaction conditions that yield nanocrystalline powders of pure PCN-222, PCN-223 and MOF-525 phase were identified. The interplay between thermodynamic and kinetic control over Zr-TCPP polymorph formation was correlated with the modulator-to-ligand molar ratio to elucidate how modulator properties influence polymorph selectivity during the reaction between Zr^{4+} and TCPP.

Defect engineering of MOFs via modulated synthesis is a promising approach for tailoring their properties. Defect characterization of Zr-TCPP MOFs revealed that in addition to modulator acidity and concentration, steric effects and solubility also influenced the defectivity of the resultant frameworks. The nature of defects was also found to be dependent on these factors. Strongly acidic modulators (DFA and FA) and sterically demanding modulators (MA and SA) tended to produce missing cluster defects while moderately acidic small-molecule modulator (PA) predominantly generated missing linker defects.

REFERENCES

- (1) Vallet-Regí, M.; Balas, F.; Arcos, D. *Angew. Chemie Int. Ed.* 2007, 46 (40), 7548–7558.
- (2) Horcajada, P.; Serre, C.; Vallet-Regí, M.; Sebban, M.; Taulelle, F.; Férey, G. *Angew. Chemie* 2006, 118 (36), 6120–6124.
- (3) Horcajada, P.; Chalati, T.; Serre, C.; Gillet, B.; Sebrie, C.; Baati, T.; Eubank, J. F.; Heurtaux, D.; Clayette, P.; Kreuz, C.; Chang, J.-S.; Hwang, Y. K.; Marsaud, V.; Bories, P.-N.; Cynober, L.; Gil, S.; Férey, G.; Couvreur, P.; Gref, R. *Nat. Mater.* 2009, 9, 172.
- (4) Lee, J.; Farha, O. K.; Roberts, J.; Scheidt, K. A.; Nguyen, S. T.; Hupp, J. T. *Chem. Soc. Rev.* 2009, 38 (5), 1450–1459.
- (5) Llabres i Xamena, F.; Gascon, J. *Metal Organic Frameworks as Heterogeneous Catalysts; Catalysis Series; The Royal Society of Chemistry*, 2013.
- (6) Garcia-Garcia, P.; Muller, M.; Corma, A. *Chem. Sci.* 2014, 5 (8), 2979–3007.
- (7) Song, J. L.; Zhang, Z. F.; Hu, S. Q.; Wu, T. B.; Jiang, T.; Han, B. X. *Green Chem.* 2009, 11 (7), 1031–1036.
- (8) So, M. C.; Wiederrecht, G. P.; Mondloch, J. E.; Hupp, J. T.; Farha, O. K. *Chem. Commun.* 2015, 51 (17), 3501–3510.
- (9) Lee, C. Y.; Farha, O. K.; Hong, B. J.; Sarjeant, A. A.; Nguyen, S. T.; Hupp, J. T. *J. Am. Chem. Soc.* 2011, 133 (40), 15858–15861.
- (10) Fleming, C. N.; Maxwell, K. A.; DeSimone, J. M.; Meyer, T. J.; Papanikolas, J. M. *J. Am. Chem. Soc.* 2001, 123 (42), 10336–10347.
- (11) Lee, C. Y.; Farha, O. K.; Hong, B. J.; Sarjeant, A. a; Nguyen, S. T.; Hupp, J.; Hupp, J. T. *Synthesis (Stuttg.)*. 2011, 15858–15861.

- (12) Son, H.-J.; Jin, S.; Patwardhan, S.; Wezenberg, S. J.; Jeong, N. C.; So, M.; Wilmer, C. E.; Sarjeant, A. A.; Schatz, G. C.; Snurr, R. Q.; Farha, O. K.; Wiederrecht, G. P.; Hupp, J. T. *J. Am. Chem. Soc.* 2013, 135 (2), 862–869.
- (13) Ma, S.; Zhou, H.-C. *Chem. Commun.* 2010, 46 (1), 44–53.
- (14) Farha, O. K.; Özgür Yazaydın, A.; Eryazici, I.; Malliakas, C. D.; Hauser, B. G.; Kanatzidis, M. G.; Nguyen, S. T.; Snurr, R. Q.; Hupp, J. T. *Nat. Chem.* 2010, 2, 944.
- (15) Li, H.; Eddaoudi, M.; O’Keeffe, M.; Yaghi, O. M. *Nature* 1999, 402 (6759), 276–279.
- (16) Li, J.-R.; Kuppler, R. J.; Zhou, H.-C. *Chem. Soc. Rev.* 2009, 38 (5), 1477–1504.
- (17) Feng, D.; Gu, Z.-Y.; Li, J.-R.; Jiang, H.-L.; Wei, Z.; Zhou, H.-C. *Angew. Chemie Int. Ed.* 2012, 51 (41), 10307–10310.
- (18) Feng, D.; Gu, Z.-Y.; Chen, Y.-P.; Park, J.; Wei, Z.; Sun, Y.; Bosch, M.; Yuan, S.; Zhou, H.-C. *J. Am. Chem. Soc.* 2014, 136 (51), 17714–17717.
- (19) Jiang, H.-L.; Feng, D.; Wang, K.; Gu, Z.-Y.; Wei, Z.; Chen, Y.-P.; Zhou, H.-C. *J. Am. Chem. Soc.* 2013, 135 (37), 13934–13938.
- (20) Zhu, J.; Shaikh, S.; Mayhall, N. J.; Morris, A. J. In *Elaboration and Applications of Metal-Organic Frameworks; Series on Chemistry, Energy and the Environment; WORLD SCIENTIFIC, 2017; Vol. Volume 2, pp 581–654.*
- (21) Deria, P.; Gómez-Gualdrón, D. A.; Hod, I.; Snurr, R. Q.; Hupp, J. T.; Farha, O. K. *J. Am. Chem. Soc.* 2016, 138 (43), 14449–14457.
- (22) Li, M.; Li, D.; O’Keeffe, M.; Yaghi, O. M. *Chem. Rev.* 2014, 114 (2), 1343–1370.
- (23) Liu, T.-F.; Feng, D.; Chen, Y.-P.; Zou, L.; Bosch, M.; Yuan, S.; Wei, Z.; Fordham, S.; Wang, K.; Zhou, H.-C. *J. Am. Chem. Soc.* 2015, 137 (1), 413–419.

- (24) Farha, O. K.; Mulfort, K. L.; Thorsness, A. M.; Hupp, J. T. *J. Am. Chem. Soc.* 2008, 130 (27), 8598–8599.
- (25) Jiang, H.-L.; Makal, T. A.; Zhou, H.-C. *Coord. Chem. Rev.* 2013, 257 (15), 2232–2249.
- (26) Xu, H.-Q.; Wang, K.; Ding, M.; Feng, D.; Jiang, H.-L.; Zhou, H.-C. *J. Am. Chem. Soc.* 2016, 138 (16), 5316–5320.
- (27) Kelty, M. L.; Morris, W.; Gallagher, A. T.; Anderson, J. S.; Brown, K. A.; Mirkin, C. A.; Harris, T. D. *Chem. Commun.* 2016, 52 (50), 7854–7857.
- (28) Islamoglu, T.; Otake, K.; Li, P.; Buru, C. T.; Peters, A. W.; Akpınar, I.; Garibay, S. J.; Farha, O. K. *CrystEngComm* 2018.
- (29) Webber, T. E.; Liu, W.-G.; Desai, S. P.; Lu, C. C.; Truhlar, D. G.; Penn, R. L. *ACS Appl. Mater. Interfaces* 2017, 9 (45), 39342–39346.
- (30) Cheetham, A. K.; Bennett, T. D.; Coudert, F.-X.; Goodwin, A. L. *Dalt. Trans.* 2016, 45 (10), 4113–4126.
- (31) Fang, Z.; Bueken, B.; De Vos, D. E.; Fischer, R. A. *Angew. Chemie - Int. Ed.* 2015, 54 (25), 7234–7254.
- (32) Hu, Z.; Castano, I.; Wang, S.; Wang, Y.; Peng, Y.; Qian, Y.; Chi, C.; Wang, X.; Zhao, D. *Cryst. Growth Des.* 2016, 16 (4), 2295–2301.
- (33) Shearer, G. C.; Chavan, S.; Bordiga, S.; Svelle, S.; Olsbye, U.; Lillerud, K. P. *Chem. Mater.* 2016, 28 (11), 3749–3761.
- (34) Wu, H.; Chua, Y. S.; Krungleviciute, V.; Tyagi, M.; Chen, P.; Yildirim, T.; Zhou, W. *J. Am. Chem. Soc.* 2013, 135 (28), 10525–10532.
- (35) Bennett, T. D.; Cheetham, A. K.; Fuchs, A. H.; Coudert, F. X. *Nat. Chem.* 2016, 9 (1), 11–16.

- (36) Cheetham, A. K.; Bennett, T. D.; Coudert, F.-X.; Goodwin, A. L. *Dalt. Trans.* 2016, 45 (10), 4113–4126.
- (37) S. Chipera and D. Bish. *Adv. Mater. Phys. Chem.* 2013, 3, 47–53.
- (38) Cheetham, A. K.; Kieslich, G.; Yeung, H. H.-M. *Acc. Chem. Res.* 2018, 51 (3), 659–667.
- (39) Ruckenstein, E., Berim, G. *Kinetic Theory of Nucleation*; CRC Press: Boca Raton, 2016.
- (40) Desiraju, G. R.; Vittal, J. J.; Ramanan, A. *Crystal Engineering*; Co-Published with Indian Institute of Science (IISc), Bangalore, India, 2011.
- (41) Thornton, A. W.; Babarao, R.; Jain, A.; Trouselet, F.; Coudert, F.-X. *Dalt. Trans.* 2016, 45 (10), 4352–4359.
- (42) Trickett, C. A.; Gagnon, K. J.; Lee, S.; Gándara, F.; Bürgi, H.; Yaghi, O. M. *Angew. Chemie Int. Ed.* 54 (38), 11162–11167.
- (43) Epley, C. C.; Love, M. D.; Morris, A. J. *Inorg. Chem.* 2017, 56 (22), 13777–13784.
- (44) Walton, K. S.; Snurr, R. Q. *J. Am. Chem. Soc.* 2007, 129 (27), 8552–8556.
- (45) Gómez-Gualdrón, D. A.; Moghadam, P. Z.; Hupp, J. T.; Farha, O. K.; Snurr, R. Q. *J. Am. Chem. Soc.* 2016, 138 (1), 215–224.

Chapter 3

Photophysical characterization of PCN-223(fb)

3.1 Introduction

One of the most important components of artificial photosynthesis assemblies are the antennae, which collect solar energy and direct it towards the reaction centers. A multi-chromophoric array with energy cascade can direct sequential photoexcited energy flow and perform the function of light harvesting antenna assemblies.¹ Multiporphyrin arrays have been studied extensively with the aim of constructing antenna assemblies that mimic natural photosynthetic systems in terms of the efficiency of excitation energy transfer (EET). Subtle changes in structural parameters, such as connectivity, distance, and orientation between porphyrin units in the array can have strong implications on the nature of interchromophoric interactions, and the rates and efficiencies of EET.² Highlighted by highly-ordered crystal structures and synthetic tunability via crystal engineering, metal organic frameworks (MOFs) allow for precise control of distances and angles between chromophores and their alignment by judicious choice of ligands and metal nodes.³⁻⁶ Porphyrin based MOFs are therefore ideal candidates to study EET as a function of structural parameters. Such studies will aid in the design of porphyrin-based architectures that are conducive for energy transfer. Before examining the role of MOF structure in EET, it is necessary to first understand the mechanistic aspects of EET and the factors that determine the efficiency of EET in porphyrin-based MOFs. To address these issues, we probed the energy transfer characteristics of PCN-223(fb), a Zr-MOF based on meso-tetrakis(4-carboxyphenyl)porphyrin.

Zr-TCPP MOFs have been studied extensively due to their exceptional chemical stability under harsh experimental conditions and their ability to exhibit a variety of functionalities like catalysis, light harvesting, gas-storage and sensing.^{4,7-12} PCN-223, in particular, has a very unique structure (Fig. 1).¹⁰ It consists of unprecedented D_{6h} symmetric $[Zr_6O_4(OH)_4]^{12+}$ nodes connected

to 12 TCPP linkers, representing the first (4,12)-connected MOF with the “shp” topology. The closely-packed structure of PCN-223 supports a high density of chromophores that can simultaneously absorb light and participate in the energy transfer process. PCN-223 also manifests a small porphyrin-porphyrin torsional angle ($\sim 55^\circ$) that facilitates strong interchromophoric electronic coupling between TCPP units.¹³ Based on these merits, PCN-223 qualifies to serve as a model system to explore EET mechanism in porphyrin-based MOFs.

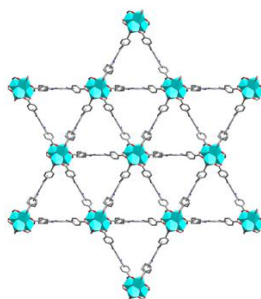


Figure 1. View of PCN-223(fb) along the c axis with uniform triangular 1D channels

Herein, we present a detailed study of the photophysical properties of PCN-223(fb). The effects of pH and temperature on the excited state properties of PCN-223(fb) were investigated and compared with those of ligand. The triplet state of the MOF was probed with the help of nanosecond transient absorption spectroscopy. Quenching studies were performed on the ligand and the MOF to determine the rate and efficiency of EET.

3.2 Materials and Methods

Materials: Meso-tetracarboxyphenylporphyrin (>97%) was purchased from Frontier Scientific and was used without further purification. Zirconium chloride (anhydrous, $\geq 99.5\%$) was purchased from Sigma-Aldrich. Dimethylformamide (DMF, spectrophotometric grade, $\geq 99.9\%$) was purchased from Fisher chemical. Propionic acid (PA, 99%), were purchased from Alfa Aesar.

Synthesis of PCN-223(fb): 10 mg of H₂TCP (1.265×10⁻⁵ moles) and 7 mg of ZrCl₄ (3×10⁻⁵ moles) were added to 10ml DMF and ultrasonically dissolved in a 6-dram vial. 2 ml propionic acid was added to the vial and the vial was sonicated for 15 minutes to get a homogeneous reaction mixture. The vial was placed in an oven set at 120 °C for 16 hours. After allowing it to cool down to room temperature, the resultant nano-crystalline MOF powder was collected by centrifugation. It was washed 3 times with DMF and then soaked in ethanol for 3 days with fresh ethanol replacement every day. The MOF was allowed to dry at room temperature and then evacuated by heating it at 100 °C under vacuum.

Powder X-ray diffraction and Scanning electron microscopy (PXRD): A 600 W Rigaku MiniFlex powder diffractometer with a Cu (K α = 0.15418 nm) radiation source was used, with a sweeping range of 2°–50° in continuous scanning mode. PXRD traces were collected in 0.05° increments at a scanning rate of 0.2°/min, and patterns were generated with PDXL software.

Scanning electron microscopy (SEM): Samples were prepared for SEM by suspending MOFs in ethanol and sonicating it. The resulting suspension was drop-casted on pre-cut glass slides. After allowing the samples to dry, the glass slides were mounted on SEM sample pegs with the help of double-sided copper tape. The sides of the glass slides and the platform of sample peg were coated with conductive carbon paint. A LEO (Zeiss) 1550 field-emission scanning electron microscope, equipped with an in-lens detector, operating at 5.0 kV was used to obtain high-resolution images of the MOF powders.

Thermogravimetric Analysis (TGA): A Q-series TGA from TA Instruments was used to assess the thermal stability of MOFs. Samples weighing ~5-10 mg were placed on a platinum pan and heated under nitrogen at a rate of 5 °C/min over the temperature range of 40–800 °C.

Gas Sorption Isotherms: The gas adsorption measurements were conducted on a Micromeritics 3Flex instrument. A 6 mm large bulb sample cell was used to hold the samples and was degassed under vacuum at a temperature of 100 °C for 24 h. The surface area of the MOFs was determined from the N₂ adsorption isotherms at 77 K by fitting the adsorption data within the 0.05–0.3 P/P₀ pressure range to the BET equation.

Diffuse absorption spectroscopy: The diffuse absorption spectra of TCPP and PCN-223(fb) were obtained using an Agilent Technologies 8453 UV-Vis diode array spectrophotometer (1 nm resolution) where the sample compartment was replaced with an integration sphere. The powder samples were diluted by mixing with BaSO₄.

Steady-state emission spectroscopy and time-resolved emission lifetimes: The steady-state emission spectra were obtained using a QuantaMaster Model QM-200-4E emission spectrophotometer from Photon Technology, Inc. (PTI). The excitation light source was a 75 W Xe arc lamp (Newport). The detector was a thermoelectrically cooled Hamamatsu 1527 photomultiplier tube (PMT). Emission traces were analyzed using Origin. Time-resolved fluorescence lifetimes were obtained via the time-correlated single photon counting technique (TCSPC) with the same QuantaMaster Model QM-200-4E emission spectrophotometer from Photon Technology, Inc. (PTI) equipped with a 350 nm LED and a Becker & Hickl GmbH PMH-100 PMT detector with time resolution of < 220 ps FWHM. Fluorescence lifetime decays were analyzed with the help of origin.

3.3 Results and Discussion: Synthesis of PCN-223(fb) was achieved by following a method that has been used in a prior work.¹⁴ Briefly, 3×10^{-5} moles of ZrCl₄ and 1.26×10^{-5} moles of TCPP were dissolved in 10 mL DMF along with 2.52×10^{-2} moles of propionic acid as the modulator. The mixture was sonicated for 15 minutes then the vial was placed in an oven and heated at 120

°C for 16 h. PCN-223(fb) MOF powders were characterized by PXRD (Fig. 2a) and SEM (Fig. 2b). Comparison of the PXRD pattern obtained from synthesis to the simulated pattern from single crystal XRD data indicated high phase purity. SEM image shows small bean-shaped MOF particles with a length of $\sim 2 \mu\text{m}$. All MOF particles are morphologically identical, which further verifies the phase purity. In addition, thermal stability and surface area of as-prepared PCN-223(fb) were studied by thermogravimetric analysis and N_2 adsorption isotherms, which agree with literature (Fig. S1 and S2).

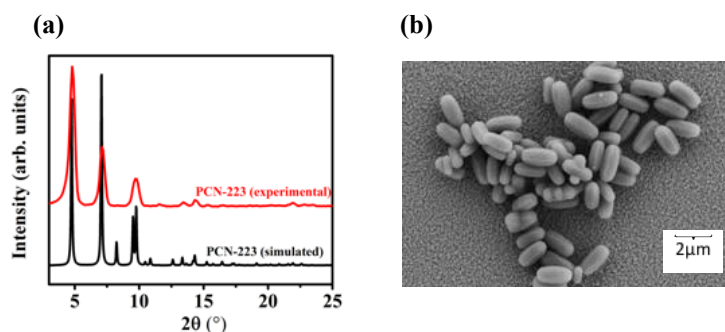


Figure 2. (a) PXRD characterization of PCN-223(fb) (b) SEM image of PCN-223(fb)

To examine how the ground and excited-state properties of TCPP are affected upon coordination into the MOF structure, the absorption spectra of TCPP and PCN-223(fb) were compared (Fig. 3). The electronic absorption spectrum of TCPP consists of two distinct regions. The first involves the transition from the ground state to the second excited state ($S_0 \rightarrow S_2$) and the corresponding band is called the Soret or B band. The second region consists of a weak transition to the first excited state ($S_0 \rightarrow S_1$) in the range between 500-750 nm (the Q bands). PCN-223(fb) displays an absorption spectrum similar to that of TCPP with a sharp Soret band and four Q bands. The Soret band of PCN-223 is blue shifted by 13 nm relative to ligand, which is attributed to structural changes that TCPP undergoes as it is incorporated in the MOF. Twisting of phenyl rings and changes in the macrocyclic ring planarity of TCPP may be responsible for increasing the

electronic transition energy-gap (S_0 - S_2), and thus for the blue shift. The peak positions and the peak intensities of Q bands of PCN-223 match those of TCPP (SI, Table 1), suggesting that the energy gap between ground state and first excited state of TCPP is relatively unaffected upon incorporation in MOF.

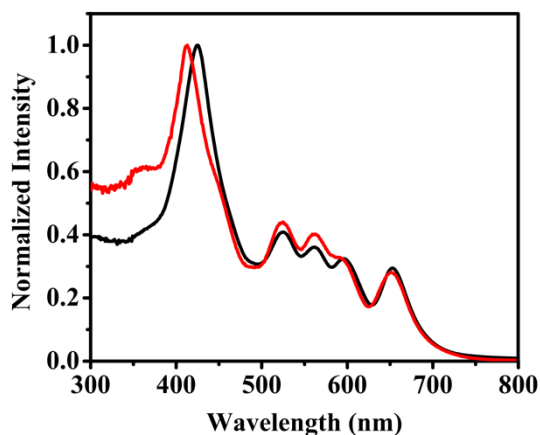


Figure 3. Diffuse absorption spectra of TCPP (black) and PCN-223(fb) (red)

The acid-base properties of porphyrins in aqueous solutions provide important information about their reactivity, aromaticity, tautomerization mechanisms and stereochemistry.¹⁵⁻¹⁷ The central macrocycle of porphyrins exhibits an amphoteric behavior and can exist in either neutral (free-base), protonated, or deprotonated form (Fig. 4). Mono-protonation of the free-base form induces nonplanar distortions in the porphyrin structure, which makes the second protonation more favorable.^{18,19} The first protonation step is immediately followed by the second step, yielding the porphyrin dication, while the monoprotinated species is present in very small amounts at any given time. To determine the pK_a values corresponding to the two protonation steps, a 10^{-6} M TCPP solution was titrated against a 0.01 M NaOH solution (Fig. S3(a)). The pH corresponding to the half equivalence point was found to be 3.14 ($pK_2 \approx pK_3 = 3.14$). A suspension of PCN-223(fb) was also titrated against 0.01 M NaOH solution to find the pK_a values corresponding to protonation of TCPP units incorporated in MOF ($pK_2 \approx pK_3 = 4.03$) (Fig. S3(b)).

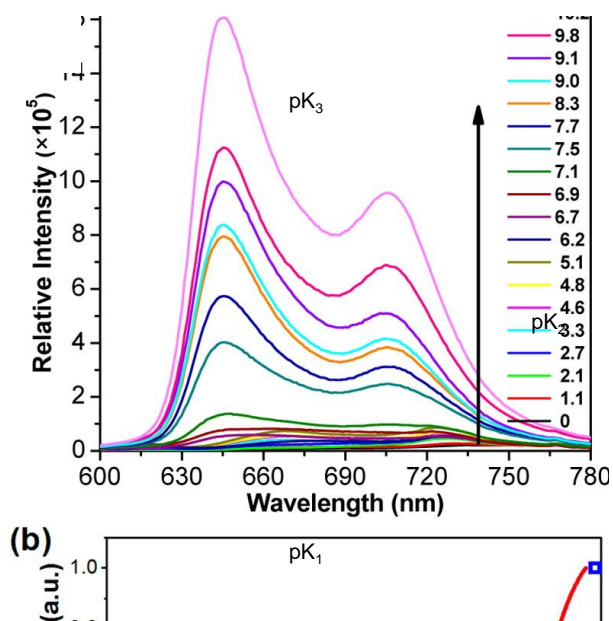


Figure 4. Protonation and deprotonation processes of TCPP in acidic and basic media.⁸ pK_1 , pK_2 and pK_3 represent the pK_a values associated with these processes. The first and second protonation processes almost indistinguishable, such that $pK_2 \approx pK_3$. The equivalence point corresponding to the protonation of TCPP and PCN-223(fb) were found to be at pH 5.54 and 5.70 respectively.

Varying solution pH can shift the protonation-deprotonation equilibrium of the macrocycle in favor of a particular form, which has been shown to greatly influence the photophysics of the porphyrin molecule.¹⁹ Non-planarity induced in the porphyrin structure due to protonation of the free-base form breaks up their π -electron conjugated double-bond system. Loss of conjugation promotes non-radiative relaxation of excited state that results in significant fluorescence quenching and short fluorescence lifetimes.²⁰ To investigate the effects of pH variation on the fluorescence properties of TCPP and PCN-223(fb), their steady-state emission spectra were measured in an experimental pH range of 3.5 to 8.5 ($\lambda_{\text{excitation}} = 415 \text{ nm}$). Given that PCN-223(fb) is stable in aqueous environments with pH values ranging from 0 to 10,¹⁰ the experimental pH range is suitable for investigating the photophysics of the MOF without loss in crystallinity. The peak positions and intensities of fluorescence spectra of TCPP and PCN-223(fb) were found to be strongly correlated

with pH of solution/suspension. The fluorescence spectra of the neutral form of TCPP and PCN-223(fb) ($5.5 < \text{pH} < 8.5$) displays a sharp band at 645 nm (Q(0,0)) and a relatively weaker band at 720 nm (Q(0,1)) (Fig 5a and 5b). The intensity of the band at 720 nm is highly diminished and is not noticeable in Fig 5. Structural changes induced in the porphyrin macrocycle due to protonation of central nitrogen atoms cause the band at 645 nm to broaden and red shift by 35 nm. As a result, the fluorescence spectrum appears to be a single, broad band with a maximum at 680 nm (Fig. 5c).

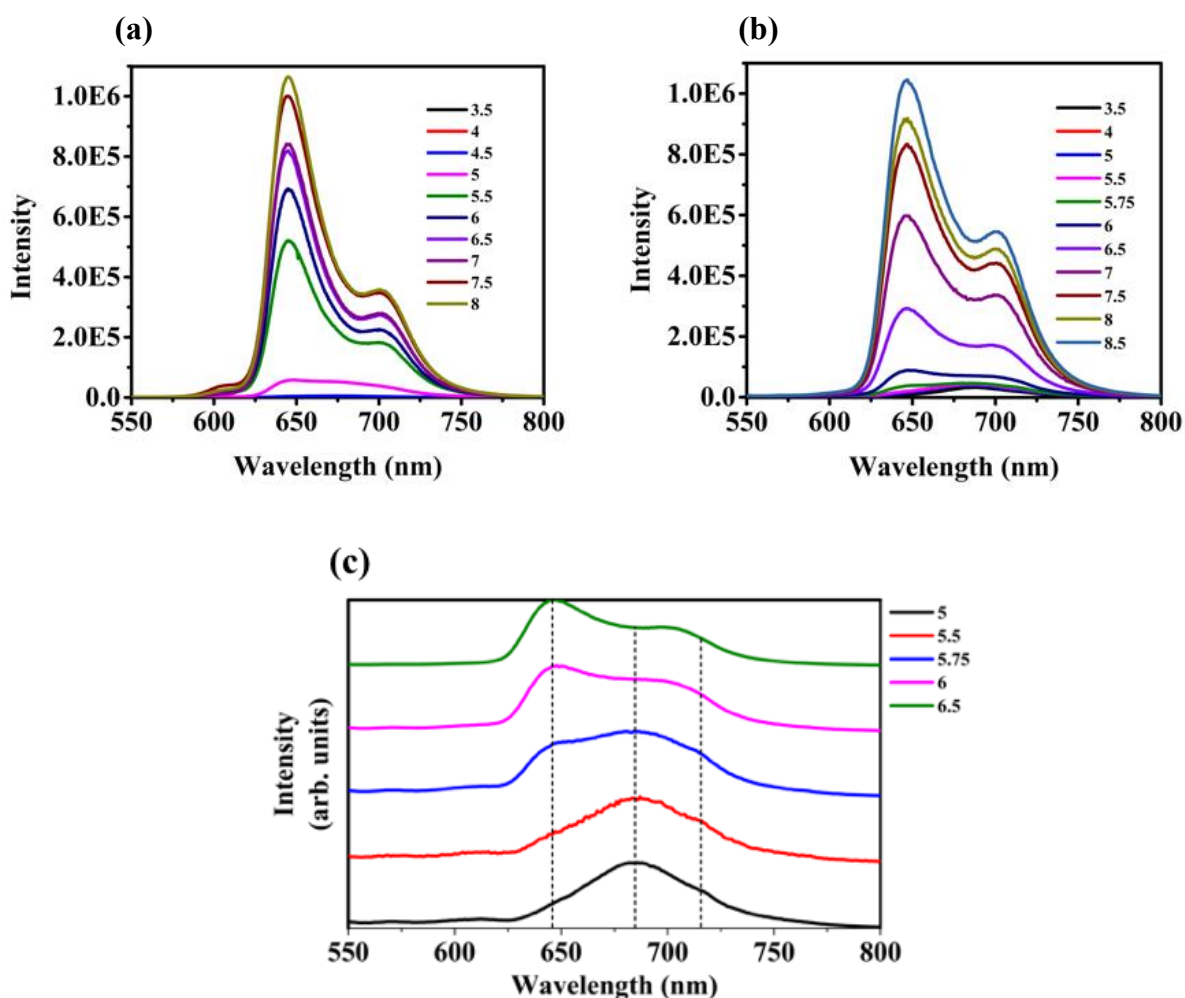


Figure 5. (a) Fluorescence spectra of TCPP in water (10^{-6}M) as a function of pH (b) Fluorescence spectra of PCN-223(fb) in water as a function of pH. (c) Spectral evolution in pH range 5 to 6.5 of PCN-223(fb).

Time resolved fluorescence measurements were also conducted to monitor the fluorescence decay kinetics of TCPP and PCN-223(fb) in the experimental pH range. The

fluorescence lifetime of TCPP ($\lambda_{\text{excitation}} = 415 \text{ nm}$, $\lambda_{\text{emission}} = 645 \text{ nm}$) was found to be strongly dependent on the pH value of solution (Figure 6a). The fluorescence decay curves of TCPP obtained in the pH range of 5.5 to 8.5 were almost identical and best fit to a mono-exponential decay model. The fluorescence lifetime extracted from the decay model corresponds to neutral TCPP form ($9.84 \pm 0.32 \text{ ns}$). At pH lower than the equivalence point ($\text{pH} < 5.54$), the fluorescence decay curves were best fit to a bi-exponential decay model having a short component (from the protonated form, $3.52 \pm 0.57 \text{ ns}$) and a longer component (from the neutral form, $9.72 \pm 0.41 \text{ ns}$) (SI, Table 2). A gradual rise in the contribution of the shorter component was observed as the pH of solution was decreased from 5.5 to 3.5, suggesting that the lifetime is sensitive to the relative concentrations of protonated and neutral forms of TCPP in solution.

Time resolved fluorescence measurements on PCN-223(fb) ($\lambda_{\text{excitation}} = 415 \text{ nm}$, $\lambda_{\text{emission}} = 645 \text{ nm}$) offered great insight into its energy transfer characteristics (Figure 6b). PCN-223(fb) exhibits monoexponential decay kinetics in the pH range of 5.75 to 8.5 with a lifetime similar to that of neutral TCPP form in solution. The absence of shorter component of lifetime indicates that the population of protonated TCPP linkers in this pH range is negligible. At pH lower than the equivalence ($\text{pH} < 5.70$), the fluorescence lifetimes of MOF suspensions were very short and beyond the resolution of the fluorimeter ($t < 200 \text{ ps}$). The highly diminished lifetime of the MOF in acidic conditions provides evidence in support of intermolecular energy transfer between TCPP linkers. We propose that upon photo-excitation, the excitation energy migrates across neutral TCPP linkers until it is quenched by a protonated linker. Protonated linkers act as dark quenchers that deactivate the excited state to the ground state via non-radiative decay pathways, without the emission of light. It is worth noting that at $\text{pH} = 5.5$, the population of protonated linkers in the MOF is expected to be very small (as the pH is close to the equivalence point). Despite their small

population, protonated TCPP linkers are still capable of significantly quenching the fluorescence intensity and drastically reducing the lifetime of MOF. The remarkable quenching abilities of protonated TCPP linker in the MOF point towards a very efficient energy transfer process.

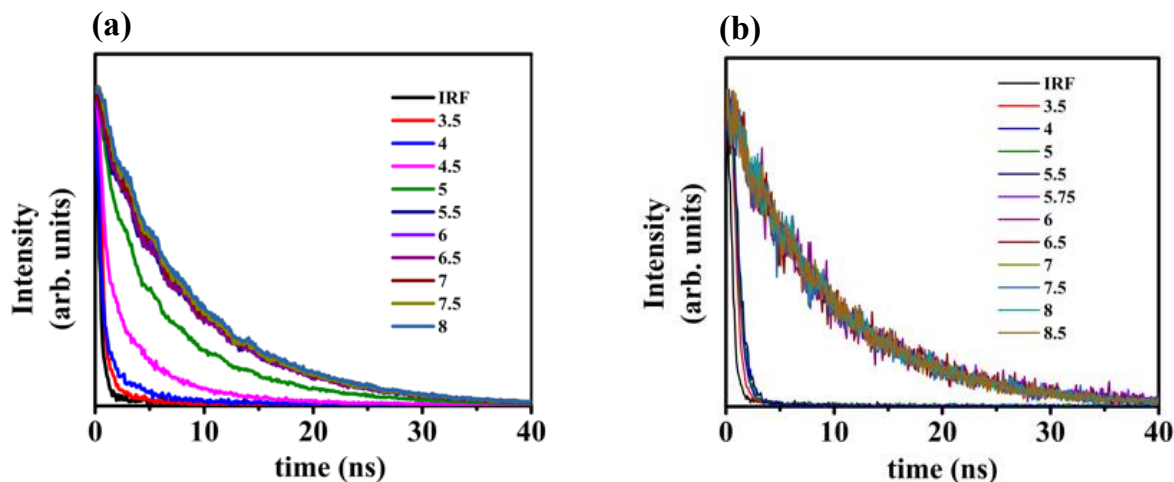


Figure 6. (a) pH dependence of the observed fluorescence lifetimes of TCPP in water (10^{-6} M) (b) pH dependence of the observed fluorescence lifetimes of PCN-223(fb) in water

Temperature dependence of the fluorescence decay rates (k_{obs}) of an emissive MOF can give insight into the mechanism of energy transfer.²⁵ At room temperature, there are various vibrational degrees of freedom that allow the excited state to fully relax between excitation energy transfer events. However, at low temperatures ($\sim 77\text{K}$) some of the vibrational degrees of freedom are frozen out. If the electronic interactions between the linkers in a MOF are very strong (strong coupling regime), then at low temperatures the rate of energy transfer can exceed that of vibrational relaxation. In such a scenario, the excitation energy can move as an exciton that is delocalized over the whole system.^{1,26} The MOF behaves as an “aggregate” and the energy transfer process is termed as “coherent”. In contrast, if the electronic interactions between the linkers in a MOF are weak (weak coupling regime), then vibrational relaxation dominates at all temperatures. At a given time “ t ”, the excitation energy remains localized on a linker. The MOF behaves as a “monomer” and the excitation energy transfer is termed as “incoherent”.

To determine whether PCN-223(fb) belongs to the strong coupling regime or the weak coupling regime, the temperature-dependent fluorescence decay kinetics of TCPP and PCN-223(fb) were compared. The fluorescence decay rates of TCPP and PCN-223(fb) were obtained at temperatures ranging from 77K to 333K (Fig. 7a and 7b). The experimental decay rates were fit to Eqn. 1 to plot the temperature dependence curves.

$$k_{\text{obs}} = k_0 + k_1 e^{-\Delta E/k_B T} \quad (\text{Equation 1})$$

where k_0 is the temperature independent term and the Arrhenius term describes the temperature dependence of k_{obs} .^{27,28} The parameters extracted from the fits are reported in Table 1.

Table 1. Experimental parameters associated with TCPP and PCN-223(fb)

	k_0 (s ⁻¹)	k_1 (s ⁻¹)	ΔE (J/molecule)
TCPP	$6.66 * 10^7 \pm 0.07 \times 10^7$	$4.02 * 10^7 \pm 0.022 \times 10^7$	$7.34 * 10^{-21} \pm 0.19 \times 10^{-21}$
PCN-223(fb)	$6.36 * 10^7 \pm 0.21 \times 10^7$	$3.33 * 10^7 \pm 0.60 \times 10^7$	$8.31 * 10^{-21} \pm 0.53 \times 10^{-21}$

The pre-exponential factor or the frequency factor (k_1) and the activation energy for transitioning from the ground state to the excited state (ΔE) of TCPP and PCN-223(fb) are very similar, suggesting that the temperature-dependent fluorescence behavior of the MOF is comparable to that of monomer TCPP units. This result implies that PCN-223(fb) belongs to the weak coupling regime. Therefore, we propose an incoherent mechanism for EET in PCN-223(fb) MOF.

In the weak coupling regime, excitation energy transfer primarily occurs through two coupling mechanisms: Dexter exchange mechanism and Förster dipole-dipole mechanism.²⁶ The Dexter mechanism requires the presence of electronic communication between the donor and acceptor via orbital overlap.^{29,30} Since the orbital overlap between adjacent porphyrin struts in Zr-based MOFs with porphyrin linkers is poor, the Dexter mechanism may not be suitable to describe energy

transfer in these MOFs.²⁵ The Förster mechanism, on the other hand, adequately describes the “through space” energy migration in these MOFs. Conventionally, Förster mechanism is applicable only when an excitation from an electronically excited donor in a singlet state is transferred to produce an electronically excited acceptor in a singlet state.³¹ Triplet states are typically not involved in the energy transfer processes governed by Förster mechanism. So far, we have only investigated the singlet excited states of TCPP and PCN-223(fb). To probe the triplet state of TCPP and PCN-223(fb), transient absorption spectroscopy was employed.

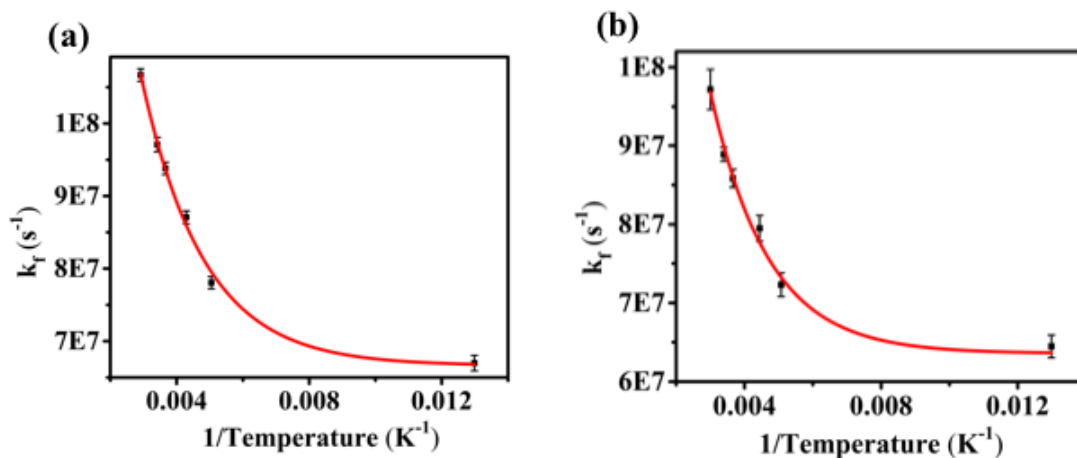


Figure 7. (a) Temperature dependence of the observed emission decay rates of TCPP in MeOH-EtOH (3:1 v/v) mixture (pH \approx 8) (b) Temperature dependence of the observed emission decay rates of PCN-223(fb) suspension (3:1 v/v) mixture (pH \approx 8)

Nanosecond transient absorption difference spectra for TCPP solution and PCN-223(fb) suspension were acquired in water at pH 8 (Fig 8a and 8b). The difference spectra for TCPP and PCN-223(fb) were almost identical, having an intense bleach at \sim 420 nm and excited state absorption centered near 470 nm. The bleach at 420 nm indicates the depletion of ground state of TCPP while the absorption maximum at 470 nm can be ascribed to triplet–triplet absorption. The transient absorption decays of TCPP and PCN-223(fb) at 470 nm exhibited single-exponential

kinetics. The triplet lifetimes of TCPP and PCN-223(fb) were found to be 267 μs and 220 μs respectively. The shorter triplet lifetime of PCN-223(fb) can be attributed to several factors, such as (a) scattering of excitation beam by macroscopic MOF particles (in suspension), (b) triple state quenching by trace amounts of oxygen trapped in MOF suspension, (c) triple state quenching via energy transfer to protonated TCPP units, and (d) triplet state quenching due to electron injection from TCPP into the Zr_6 node. Further research efforts are needed to determine which of these factors is predominantly responsible for the quenching of triplet state of PCN-223(fb).

(a)

(b)

(c)

(d)

Figure 8. Transient absorption difference spectra of (a) TCPP and (b) PCN-223(fb) measured in degassed water at room temperature following 532 nm pulsed laser excitation (12-15 mJ/pulse, 5–7 ns fwhm). Both difference spectra represent an average of 30 transients. (c) Fitted transient absorption decays of TCPP along with the residual (green colored). (d) Fitted transient absorption decays of PCN-223(fb) along with the residual (green colored).

By quantifying the energy transfer efficiency of PCN-223(fb), we can compare its EET performance with other porphyrin-based MOFs reported in literature.^{25,32,33} Son et al. has shown that energy transfer efficiency of a MOF can be evaluated by relating the amount of quencher to the extent of quenching in MOFs.^{34,35} The relationship between the quencher concentration and extent of quenching is provided by Stern-Volmer equation (Eqn. 2), where I_0 is the fluorescence intensity without the presence of quencher, I is the fluorescence intensity at a particular concentration of quencher, K_{SV} is the Stern-Volmer quenching constant, and $[Q]$ is the quencher concentration.

$$\frac{I_0}{I} = 1 + K_{SV}[Q] \quad (\text{Equation 2})$$

The quenching rate k_Q can be calculated by dividing K_{SV} with the fluorescence lifetime in the absence of quencher (τ_0). A higher k_Q value translates into higher EET efficiency. Stern-Volmer plots of TCPP and PCN-223(fb) were obtained using potassium ferricyanide as the quencher (Fig. 8). Upon complexation with TCPP, potassium ferricyanide is known to quench its singlet excited state via reductive electron transfer.³⁶

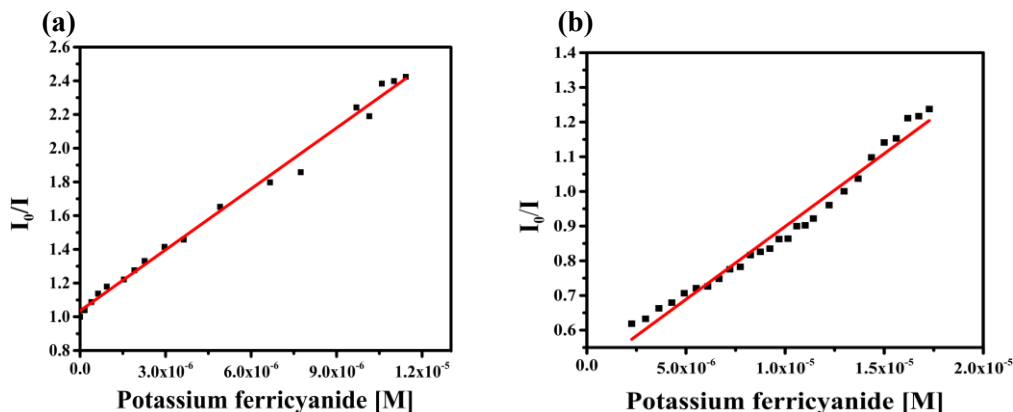


Figure 8. (a) Stern-Volmer plot of TCPP (10^{-6} M) (b) Stern-Volmer plot of PCN-223(fb)

The Stern-Volmer rate constants and quenching rate constants of TCPP and PCN-223(fb) are provided in Table 2. Interestingly, the Stern-Volmer rate constants and quenching rate constants

indicate that MOF is quenched to a lesser extent than monomeric TCPP. This may be due to the binding (association) constant of TCPP-Ferricyanide complex being higher in solution than in suspension (with MOF).³⁷ It is also possible that potassium ferricyanide selectively adsorbs on the surface of the MOF and does not penetrate inside the pores, which lowers the number of TCPP linkers that can directly interact with ferricyanide. Efforts to identify quenchers that can penetrate the surface of PCN-223(fb) and quench the excited state of TCPP via an energy transfer process are currently in progress.

Table 2. Stern-Volmer rate constant and quenching rate constants of TCPP and PCN-223(fb)

	$K_{sv} (M^{-1})$	$k_q (M^{-1}s^{-1})$
TCPP	120558	$1.19 * 10^{13}$
PCN-223(fb)	43328	$4.8 * 10^{12}$

3.4 Conclusion

Photophysical characterization of PCN-223(fb) was carried out with the help of diffuse reflectance spectroscopy, steady-state emission spectroscopy, time resolved fluorescence spectroscopy and nanosecond transient absorption spectroscopy. The pH dependence of the fluorescence decay kinetics of PCN-223(fb) revealed that protonated TCPP linkers act as energy traps that deactivate the excited state in a very efficient manner. Temperature dependence of the observed fluorescence decay rates of PCN-223(fb) was comparable to that of monomeric TCPP units, suggesting that the interchromophoric interactions between TCPP linkers belong to the weak coupling regime. Therefore, an incoherent, hopping type mechanism was proposed for EET in PCN-223(fb). Fluorescence quenching experiments with potassium ferricyanide as the quencher showed that PCN-223(fb) (in suspension) is quenched to a lesser extent than ligand (in solution). This can be

attributed either to lower binding constants of TCPP-Ferricyanide complex in PCN-223(fb) or to the inability of potassium ferricyanide to access the pores of MOF.

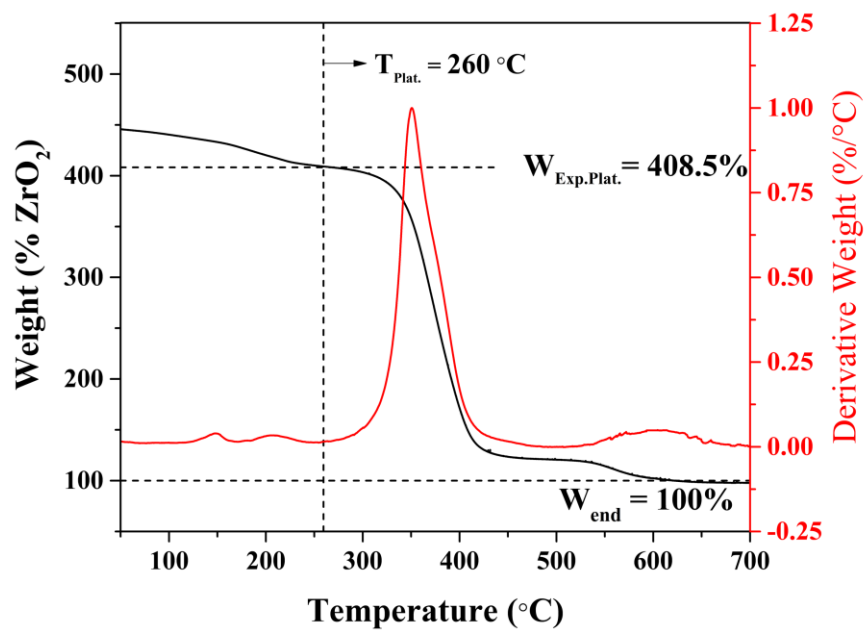
3.5 Bibliography

- (1) Renger, T. *Photosynth. Res.* **2009**, *102* (2), 471–485.
- (2) Yang, J.; Yoon, M.-C.; Yoo, H.; Kim, P.; Kim, D. *Chem. Soc. Rev.* **2012**, *41* (14), 4808–4826.
- (3) Li, Y.; Xu, H.; Ouyang, S.; Ye, J. *Phys. Chem. Chem. Phys.* **2016**, *18* (11), 7563–7572.
- (4) So, M. C.; Wiederrecht, G. P.; Mondloch, J. E.; Hupp, J. T.; Farha, O. K. *Chem. Commun.* **2015**, *51* (17), 3501–3510.
- (5) Furukawa, H.; Cordova, K. E.; O’Keeffe, M.; Yaghi, O. M. *Science* (80-.). **2013**, *341* (August), 974.
- (6) Kuc, A.; Enyashin, A.; Seifert, G. *J. Phys. Chem. B* **2007**, *111* (28), 8179–8186.
- (7) Feng, D.; Gu, Z.-Y.; Li, J.-R.; Jiang, H.-L.; Wei, Z.; Zhou, H.-C. *Angew. Chemie Int. Ed.* **2012**, *51* (41), 10307–10310.
- (8) Jiang, H.-L.; Feng, D.; Wang, K.; Gu, Z.-Y.; Wei, Z.; Chen, Y.-P.; Zhou, H.-C. *J. Am. Chem. Soc.* **2013**, *135* (37), 13934–13938.
- (9) Morris, W.; Voloskiy, B.; Demir, S.; Gándara, F.; McGrier, P. L.; Furukawa, H.; Cascio, D.; Stoddart, J. F.; Yaghi, O. M. *Inorg. Chem.* **2012**, *51* (12), 6443–6445.
- (10) Feng, D.; Gu, Z.-Y.; Chen, Y.-P.; Park, J.; Wei, Z.; Sun, Y.; Bosch, M.; Yuan, S.; Zhou, H.-C. *J. Am. Chem. Soc.* **2014**, *136* (51), 17714–17717.
- (11) Feng, D.; Jiang, H.-L.; Chen, Y.-P.; Gu, Z.-Y.; Wei, Z.; Zhou, H.-C. *Inorg. Chem.* **2013**, *52* (21), 12661–12667.

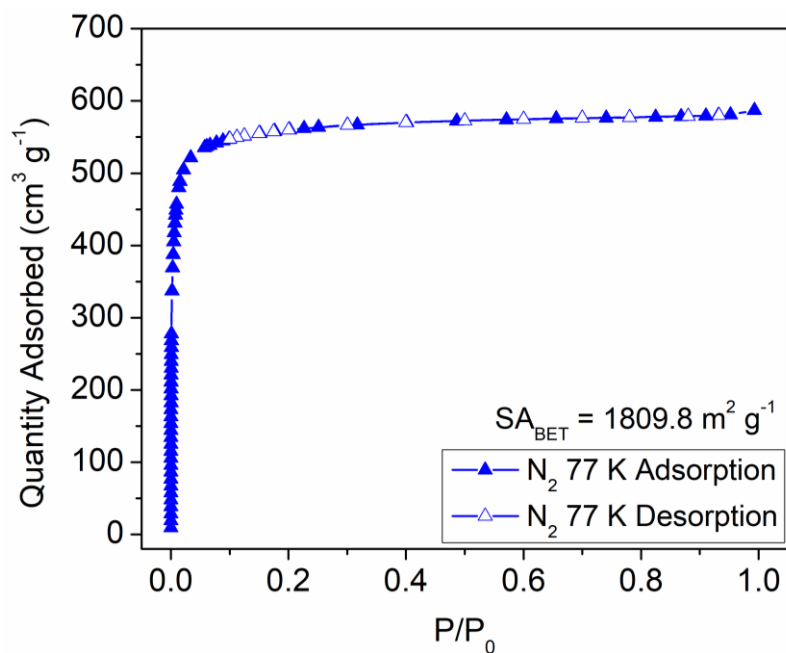
- (12) Deria, P.; Gómez-Gualdrón, D. A.; Hod, I.; Snurr, R. Q.; Hupp, J. T.; Farha, O. K. *J. Am. Chem. Soc.* **2016**, *138* (43), 14449–14457.
- (13) Deria, P.; Yu, J.; Balaraman, R. P.; Mashni, J.; White, S. N. *Chem. Commun.* **2016**, 52 (88), 13031–13034.
- (14) Shaunak M. Shaikh, Pavel Usov, Jie Zhu, Meng Cai, James Alatis, A. J. M. **2018**.
- (15) Seybold, P. G.; Gouterman, M. *J. Mol. Spectrosc.* **1969**, *31* (1–13), 1–13.
- (16) Biesaga, M.; Pyrżyńska, K.; Trojanowicz, M. *Talanta* **2000**, *51* (2), 209–224.
- (17) Lo, P.-C.; Leng, X.; Ng, D. K. P. *Coord. Chem. Rev.* **2007**, *251* (17), 2334–2353.
- (18) Rudine, A. B.; DelFatti, B. D.; Wamser, C. C. *J. Org. Chem.* **2013**, *78* (12), 6040–6049.
- (19) Hynninen, P. H. *J. Chem. Soc. Perkin Trans. 2* **1991**, No. 5, 669–678.
- (20) Kruk, M. M.; Starukhin, A. S.; Maes, W. *Macroheterocycles* **2011**, *4* (2), 69–79.
- (21) Gouterman, M. *J. Mol. Spectrosc.* **1961**, *6*, 138–163.
- (22) Wagniere, G. and M. G. 1963.
- (23) Faraday, D. **1985**, *76* (ii), 1978–1985.
- (24) Harriman, A.; Richoux, M.-C. *J. Photochem.* **1984**, *27* (2), 205–214.
- (25) Zhu, J.; Shaikh, S.; Mayhall, N. J.; Morris, A. J. In *Elaboration and Applications of Metal-Organic Frameworks*; Series on Chemistry, Energy and the Environment; WORLD SCIENTIFIC, 2017; Vol. Volume 2, pp 581–654.
- (26) Valeur, B.; Berberan-Santos, M. N. *Excitation Energy Transfer*; 2012.
- (27) Abrahamsson, M.; Becker, H.-C.; Hammarström, L.; Bonnefous, C.; Chamchoumis, C.; Thummel, R. P. *Inorg. Chem.* **2007**, *46* (24), 10354–10364.
- (28) Abrahamsson, M.; Becker, H.-C.; Hammarström, L. *Dalt. Trans.* **2017**, *46* (39), 13314–13321.

- (29) Dexter, D. L. *J. Chem. Phys.* **1953**, *21* (5), 836.
- (30) Lin, J.; Hu, X.; Zhang, P.; Van Rynbach, A.; Beratan, D. N.; Kent, C. A.; Mehl, B. P.; Papanikolas, J. M.; Meyer, T. J.; Lin, W.; Skourtis, S. S.; Constantinou, M. *J. Phys. Chem. C* **2013**, *117* (43), 22250–22259.
- (31) Andrews, D. L. *Chem. Phys.* **1989**, *135* (2), 195–201.
- (32) Maligaspe, E.; Kumpulainen, T.; Lemmetyinen, H.; Tkachenko, N. V.; Subbaiyan, N. K.; Zandler, M. E.; D'Souza, F. *J. Phys. Chem. A* **2010**, *114* (1), 268–277.
- (33) Lee, C. Y.; Farha, O. K.; Hong, B. J.; Sarjeant, A. A.; Nguyen, S. T.; Hupp, J. T. *J. Am. Chem. Soc.* **2011**, *133* (40), 15858–15861.
- (34) Son, H. J.; Jin, S.; Patwardhan, S.; Wezenberg, S. J.; Jeong, N. C.; So, M.; Wilmer, C. E.; Sarjeant, A. A.; Schatz, G. C.; Snurr, R. Q.; Farha, O. K.; Wiederrecht, G. P.; Hupp, J. T. *J. Am. Chem. Soc.* **2013**, *135* (2), 862–869.
- (35) Patwardhan, S.; Jin, S.; Son, H.-J.; Schatz, G. C. *Mater. Res. Soc. Symp. Proc.* **2013**, *1539*, 22–27.
- (36) D'souza, F.; Krishnan, V. *Proc. Indian Acad. Sci. - Chem. Sci.* **1990**, *102* (2), 131–146.
- (37) Makarska-Bialokoz, M. *Spectroscopic Study of Porphyrin-Caffeine Interactions*; 2012; Vol. 22.

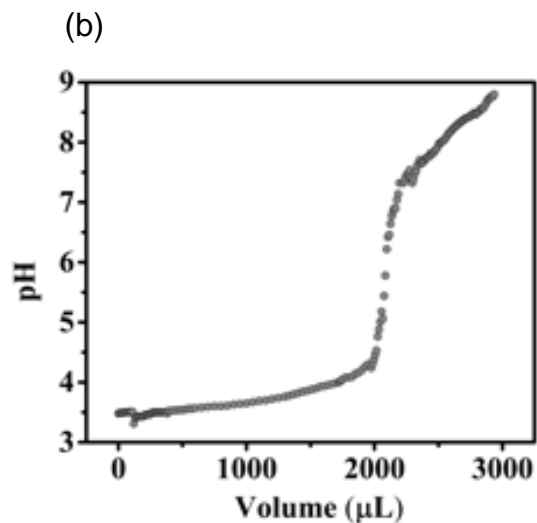
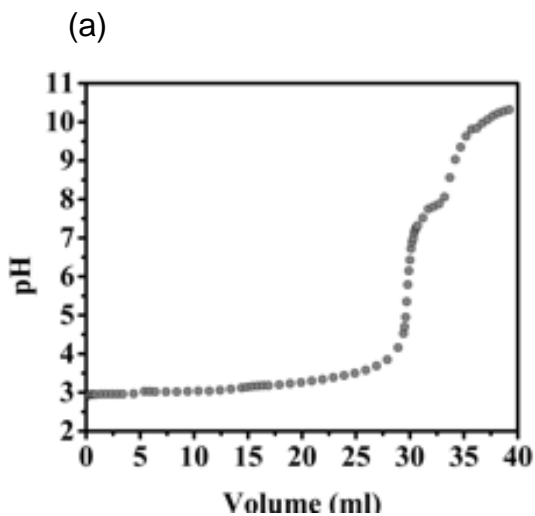
3.6 Supplementary information



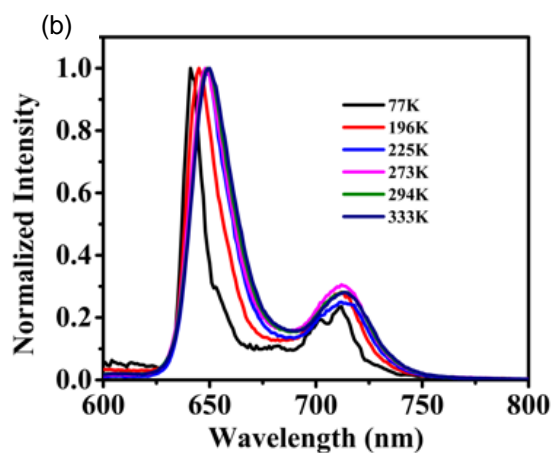
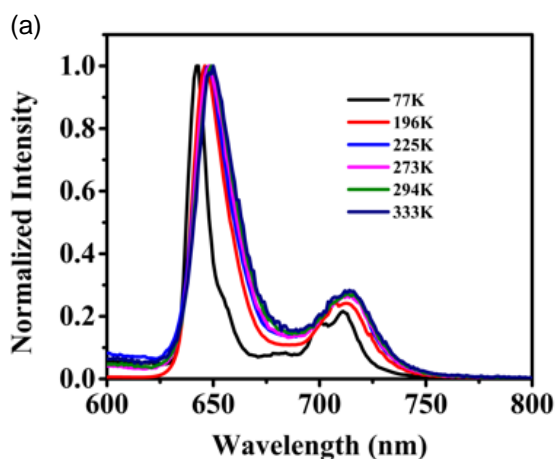
S1. TGA plot of PCN-223(fb)



S2. N₂ gas adsorption isotherm of PCN-223(fb)



S3. (a) Titration curve of TCPP in water (10^{-6}M) against 0.01 M NaOH solution. The first and second equivalence points of titration are around pH 5.54 and 7.5 respectively (b) Titration curve of PCN-223(fb) in water (10^{-6}M) against 0.01 M NaOH solution. The equivalence point of titration is around pH 5.70



S4. (a) Steady-state spectra of TCPP as a function of temperature (b) Steady-state spectra of PCN-223(fb) as a function of temperature

Table 1. Absorption data measured for TCPP and PCN-223(fb)

	B(Soret)	Q _y (1,0)	Q _y (0,0)	Q _x (1,0)	Q _x (0,0)
TCPP	425nm	525nm	561nm	597nm	652nm
PCN-223(fb)	412nm	524nm	561nm	595nm	652nm

Table 2. Fluorescence lifetimes of TCPP as a function of pH

pH	Short component, τ_1 (ns) (% contribution)	Long component, τ_2 (ns) (% contribution)
3.5	3.1 ± 0.31	-
4	4.7 ± 0.41 (80.23%)	9.23 ± 0.22 (19.77%)
4.5	4.40 ± 0.19 (55.56%)	9.65 ± 0.87 (44.4%)
5	4.01 ± 0.29 (22.23%)	10.17 ± 0.45 (77.77%)
5.5	4.43 ± 0.55 (14.36%)	9.80 ± 0.63 (85.64%)
6	-	9.34 ± 0.37
6.5	-	9.55 ± 0.47
7	-	9.50 ± 0.51
7.5	-	9.43 ± 0.36
8	-	9.67 ± 0.39

Table 3. Fluorescence lifetimes of PCN-223(fb) as a function of pH

pH	Short component, τ_1 (ns) (% contribution)	Long component, τ_2 (ns) (% contribution)
3.5	-	-
4	-	-
5	-	-
5.5	-	-
5.75	-	8.75 ± 0.14
6	-	8.99 ± 0.28
6.5	-	9.04 ± 0.48
7	-	9.01 ± 0.26
7.5	-	9.23 ± 0.69
8	-	9.26 ± 0.78
8.5	-	9.19 ± 0.32

Chapter 4

Energy Transfer in Metal-Organic Frameworks

4.1 Background information about energy transfer

In order to create technologies based on excitation energy transfer (enhanced photovoltaic cells, more efficient photocatalytic reactors, etc.), one must first have a firm understanding of the underlying quantum mechanical mechanisms. In other words, how does energy in the form of an initially excited chromophore (donor) transfer to a different chromophore (acceptor)? To answer this question, it is helpful to first consider this as a simple two-state model. In the “initial state”, $|i\rangle$, the donor is excited, and the acceptor is in its ground-state: $|D^*A\rangle$. In the “final state”, $|f\rangle$, the acceptor is excited, while the donor is now in its ground state: $|DA^*\rangle$. This is represented schematically in Figure 1. Assuming the chromophore’s nuclei are frozen and the electronic coupling between the states is static (i.e., $V = \langle i|\widehat{H}|f\rangle \neq V(t)$), the excitation energy will simply oscillate between the two chromophores at a frequency determined by both V and the energy gap between the states, $\omega_{fi} = E_f - E_i/\hbar$. The exact solution to the time-dependent Schrödinger equation is trivially obtained, and the functional form illustrates the oscillatory behavior:

$$P_f(t) = \frac{4|V|^2}{\hbar^2\omega_{fi}^2 + 4|V|^2} \sin^2\left(\sqrt{\frac{\omega_{fi}^2}{4} + \frac{|V|^2}{\hbar^2}} t\right) \quad (1)$$

where $P_f(t)$ is the time-dependent probability that the system is in state $|f\rangle$.^{1,2,3}

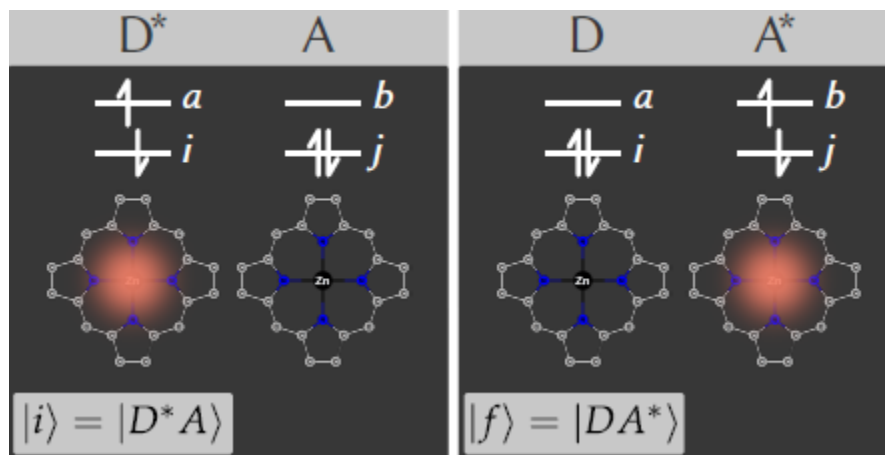


Figure 1: Schematic representation of the initial state and final states of a chromophore dimer. Note, that the actual symmetry adapted combinations of the single particle excitations have been neglected for graphical clarity. The HOMO and LUMO orbitals on Donor and Acceptor are labelled by the letters, i , a , j , and b , respectively.

4.1.1 Coupling Regimes

In reality, these two electronic states are not completely insulated from the rest of the molecule. As time evolves, so too do the chromophores' nuclei, and we must take into account the interactions between the electronic and nuclear degrees of freedom. To incorporate this nuclear motion, one usually categorizes a problem as existing in one of two limiting cases: 1) strong chromophore coupling, and 2) weak chromophore coupling.

4.1.1.1 Strong Coupling:

For very strong chromophore interactions, V , the oscillations occur very quickly, much quicker than the heavy nuclei move, and we say that the excitation energy transfers coherently. This language implies that it is more appropriate to describe this system as existing in coherent superpositions of the $|i\rangle$ and $|f\rangle$ states. As such, the $|i\rangle$ and $|f\rangle$ states are quantum mechanically entangled, and thus behave somewhat like a two-level system (at least at very short times), with populations oscillating quickly between the two chromophores. As a result of the coherent

superposition of states occurring at different positions in space, the strongly coupled regime leads to states which are delocalized in space. In order to model the time evolution of both the electronic and nuclear degrees of freedom, density matrix approaches are often used,^{4,5} and one attempts to numerically integrate the Louisville-von Neumann equation.

4.1.1.2 Weak Coupling:

In contrast, if the coupling between the two states is weak such that the rate of state-to-state oscillation is slow compared to the nuclear motion, we can assume that the vibrational state fully relaxes between excitation energy transfer events, and we label this excitation energy transfer as incoherent. The metal organic frameworks (MOFs) discussed in this chapter are found to exist in this regime, and thus incoherent mechanisms will be solely discussed. In order to make progress towards understanding excitation energy transfer in the weakly coupled regime, we will make use of the fact that V is small and then employ perturbation theory. Applying first-order perturbation theory to the time-dependent Schrödinger equation, one finds the probability of populating the final state, $|f\rangle$, to be:

$$P_f(t) = \frac{4|V|^2}{\hbar^2\omega_{fi}^2} \sin^2\left(\frac{\omega_{fi}}{2}t\right), \quad (2)$$

which is a direct simplification of Equation 1.

This rate does not yet include any coupling to the nuclear motion, which has the effect of “smearing” out the state energies. As a consequence, at any given time the initial state $|i\rangle$ has the opportunity to transfer to an effectively different final state (since the nuclear motion continually changes the electronic environment). This probability becomes sharply peaked around values where the initial and final states are degenerate, such that if the long-time limit is considered, the probability of the system transitioning to the final state is only non-zero when the two states have

equal energy. The equation which summarizes this is the state-to-state form of the famous Fermi's golden rule¹:

$$P_f(t) = \frac{2\pi}{\hbar^2} |V|^2 \delta(E_f - E_i) t \quad (3)$$

In this form, the delta function, is the resonance condition. And the rate, of this process is simply the time derivative of Equation. 3,

$$k_f = \frac{2\pi}{\hbar^2} |V|^2 \delta(E_f - E_i) \quad (4)$$

Note that one of the key features of Fermi's Golden Rule, is that the rate of transition is not a function of time. In order to obtain the actual rate from this equation, one must of course be able to compute the electronic matrix element, $V = \langle i | \hat{H} | f \rangle$. This is the topic of the next section.

4.1.2 Coupling Mechanisms

If we take Figure 1 literally and assume¹ that each chromophore's excited state involves only a pair of symmetry adapted excitations between a single occupied and a single virtual orbital, the two states very simply can be written:

$$|i\rangle = \frac{1}{\sqrt{2}} (|\psi_i^a\rangle \pm |\psi_i^{\bar{a}}\rangle) \quad (5)$$

$$|f\rangle = \frac{1}{\sqrt{2}} (|\psi_j^b\rangle \pm |\psi_j^{\bar{b}}\rangle) \quad (6)$$

where, the bar above orbital indices denote electrons with β spin. For positive and negative superpositions (spin singlet and triplet states, respectively), the Hamiltonian matrix elements are:

¹ This assumption is only used to simplify discussion, and is not needed in a full treatment. However, if natural transition orbitals (instead of the canonical Hartree-Fock orbitals) are used to define these orbitals, then this minimal picture becomes much more realistic.

$$\langle i^1 | \hat{H} | f^1 \rangle = 2(ai|jb) - (ab|ji) \quad \text{Singlet Coupling} \quad (7)$$

$$\langle i^3 | \hat{H} | f^3 \rangle = -(ab|ji) \quad \text{Triplet Coupling} \quad (8)$$

These two distinct types of electron repulsion integrals $(ai|jb)$ and $(ab|ji)$ are associated with the conceptual mechanisms illustrated in Figure 2. From here, it is clear that singlet states have two distinct mechanisms of energy transfer, Förster and Dexter, while triplet states have only one mechanism, Dexter.

4.1.2.1 Distance dependence of coupling mechanisms

As illustrated in Figure 2, the two types of integrals coupling the excited states have different qualitative interpretations. Förster type coupling involves only intra-chromophore electron transitions, whereas Dexter type coupling has only inter-chromophore electron transitions. Intuitively, we should then expect to see different behaviors between the two mechanisms when the chromophore-chromophore distance changes. This is indeed the case. The distance dependence of the Dexter and Förster integrals will be inspected in the following two subsections.

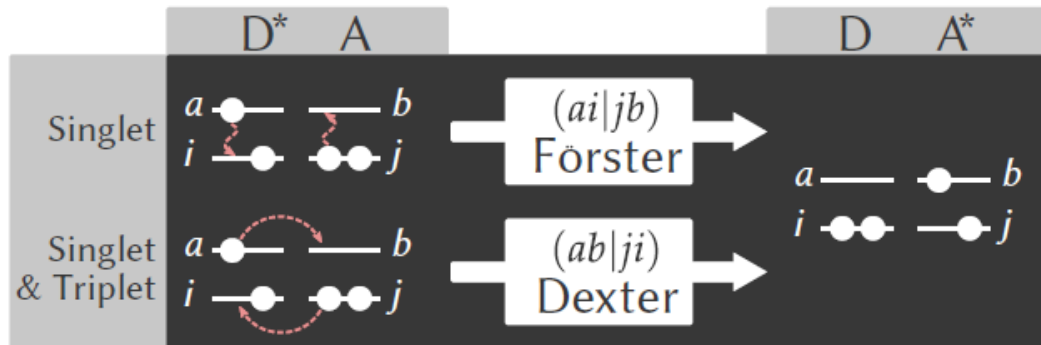


Figure 2: Connection between the conceptual transfer mechanisms and the mathematical description present in the electron repulsion integrals of the Hamiltonian matrix elements. $(ai|jb)$ contribute to Förster type coupling between singlet states, while $(ab|ji)$ contributes to Dexter type coupling between both singlet and triplets.

4.1.2.2 Dexter type integral, ($ab|ji$): To understand the nature of the Dexter (or exchange) interaction, we write out the integral explicitly:

$$(ab|ji) = \int dr_A dr_D \phi_a(r_A) \phi_b(r_A) \frac{1}{r_{DA}} \phi_j(r_D) \phi_i(r_D) \quad (9)$$

The only time that the product of molecular orbitals, $\phi_a(r)\phi_b(r)$ or $\phi_j(r)\phi_i(r)$, can be non-zero is if there is spatial overlap between the pairs. Note, that this is not a statement about orbital orthogonality, as all orbitals are assumed orthogonal. Since orbitals i and a are on the donor, and j and b on the acceptor, this requires the two chromophores to be close to one another. Because of the exponential decay of the wavefunction in free space, the overlap between these orbitals decays exponentially. Consequently, the Dexter type interaction also decays exponentially with increasing inter-chromophore distance. This means that at long distances, only singlet states can undergo excitation energy transfer, since the Dexter (or exchange) pathway is closed. However, through indirect coupling with intermediate states, more complicated Dexter pathways can also exist, which relax this constraint somewhat^{6,7}. The short-range nature of Dexter type interaction makes it strongly sensitive to the chemical structure between the chromophores and may potentially be helpful in directing energy into spatially localized energy transfer conduits or pathways. One dimensional (1D) energy transfer networks maybe particularly desirable for solar energy capture and conversion because they can direct energy in a specific direction towards a catalyst. Fine-tuning the directionality of such energy transfer pathways by manipulating the intervening molecular structure and inter-chromophore distances can enable the design of smart energy collecting materials.⁸

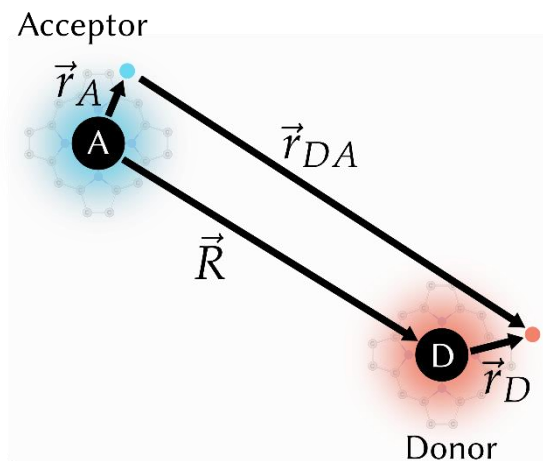


Figure 3: Illustration of the coordinate system used for expressing the two electron repulsion integrals as a dipole-dipole interaction

4.1.2.3 Förster type integral, $(ai|jb)$: For the Förster (or coulomb) term, the explicit forms of this integral is

$$(ai|jb) = \int dr_A dr_D \phi_a(r_A) \phi_i(r_A) \frac{1}{r_{DA}} \phi_j(r_D) \phi_b(r_D) \quad (10)$$

Unlike with the Dexter integral, the orbital products occur between orbitals on the same chromophore, and so no overlap dependence arises. To understand the distance dependence of this integral, it is helpful to focus on the $\frac{1}{r_{DA}}$ part. Referring to Figure 3, the following substitution can be made to remove the explicit inter-electron coordinate:

$$\begin{aligned} \vec{r}_{DA} &= \vec{R} + \vec{r}_D - \vec{r}_A \\ &= \vec{R} + \vec{r}, \end{aligned} \quad (11)$$

where, $\vec{r} = \vec{r}_D - \vec{r}_A$.

Considering the fact that the inter-chromophore distance is typically much larger than the fluctuations of the electrons about each chromophore, leading to a binomial expansion,

$$\frac{1}{(1+x)^\alpha} = \sum_{k=0}^{\infty} \binom{\alpha}{k} x^k \quad (12)$$

This expansion is rapidly convergent (only a few k values needed) when $x \ll 1$, which happens to be true in our case since,

$$x = \frac{(r^2 + 2\vec{r} \cdot \vec{R})}{R^2} \quad (13)$$

and R is much larger than r . Using this expansion, we obtain,

$$\frac{1}{r_{DA}} = \frac{1}{R} - \frac{\vec{r}_D \cdot \vec{n}_R - \vec{r}_A \cdot \vec{n}_R}{R^2} + \frac{3(\vec{r} \cdot \vec{n}_R)^2 - r^2}{2R^3} + \text{Higher-order terms}, \quad (14)$$

where, \vec{n}_R is the unit vector pointing along R . It is easy to see that, because the molecular orbitals are orthogonal, the first term does not contribute to the $(ai|jb)$ integral.

$$\begin{aligned} (ai|jb) &\Leftarrow \int dr_A dr_D \phi_a(r_A) \phi_i(r_A) \frac{1}{R} \phi_j(r_D) \phi_b(r_D) \\ &= \frac{1}{R} \int dr_A \phi_a(r_A) \phi_i(r_A) \int dr_D \phi_j(r_D) \phi_b(r_D) \\ &= \frac{1}{R} (0)(0) = 0 \end{aligned}$$

The same is readily seen for the second order-term. One then finds that the first non-zero term is the third-order term, which decays with $\frac{1}{R^3}$,

$$(ai|jb) = \frac{\vec{d}_A \cdot \vec{d}_D - 3(\vec{d}_D \cdot \vec{n}_R)(\vec{d}_A \cdot \vec{n}_R)}{R^3} + \text{Higher-order terms}, \quad (15)$$

where definition of the *transition dipole moment*, \vec{d}_A or \vec{d}_D , has been introduced,

$$\vec{d}_A = \int dr_A \phi_j(r_A) \phi_b(r_A) \vec{r}_A. \quad (16)$$

Thus, the Förster type integral, $(ai|jb)$, has an R^{-3} dependence on the *inter*-chromophore distance. This allows this mechanism to occur at rather long distances. For convenience, one often

defines a unit vector \vec{n}_A in the direction of the dipole transition moment such that $\vec{d}_A = |\mu_A|\vec{n}_A$, to isolate all the orientational dependence into a single constant, κ :

$$\kappa = \vec{n}_A \cdot \vec{n}_D - 3(\vec{n}_D \cdot \vec{n}_R)(\vec{n}_A \cdot \vec{n}_R), \quad (17)$$

which leads to,

$$(ai|jb) \approx \frac{|\mu_A||\mu_D|\kappa}{R^3} \quad (18)$$

Substituting this into Fermi's Golden Rule, Equation 4, we see the characteristic R^{-6} distance dependence of Förster energy transfer,

$$k_{if}^{\text{Förster}} = \frac{2\pi}{\hbar^2} \frac{|\mu_A|^2 |\mu_D|^2 \kappa^2}{R^6} \delta(E_f - E_i). \quad (19)$$

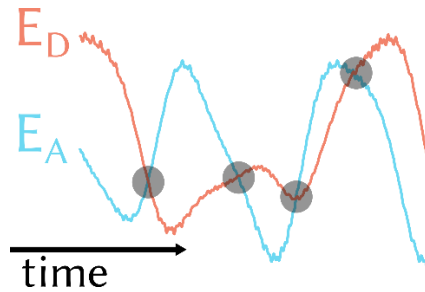


Figure 4: Cartoon representation of the time dependence of the Donor and Acceptor excitation energies. Resonance transitions only occur when the energy gap goes to zero, highlighted in grey.

This, however, is not the typical form of the rate expression used. Because the energy transfer can only occur when the energy gap $E_f - E_i$ goes to zero, a system in state $|i\rangle$ must wait until the thermal motion creates a curve crossing between the chromophore energies, as shown in Figure 4. Thus, the long-time probability of making a transition dependence on how “correlated” the motion of the two chromophores is. Correlation functions are the mathematical way to quantify this “correlation”. By using the integral definition of the delta function,

$$\delta(E_f - E_i) = \frac{1}{2\pi} \int_{-\infty}^{\infty} e^{i(E_f - E_i)t} dt, \quad (20)$$

to define a time propagator and thermally average over final states, one can transform the above rate expression into one which depends on the product of transition dipole moment correlation functions on the donor and the acceptor. Then, taking into account that the absorption or fluorescence spectrum is simply the Fourier transform of the transition dipole-moment correlation functions, and using Parsival's theorem, one can then write the Förster rate expression in terms of the experimentally available normalized absorption and emission spectra,³ $\bar{\sigma}_A(\omega) = \frac{\sigma_A(\omega)}{|\mu_A|}$:

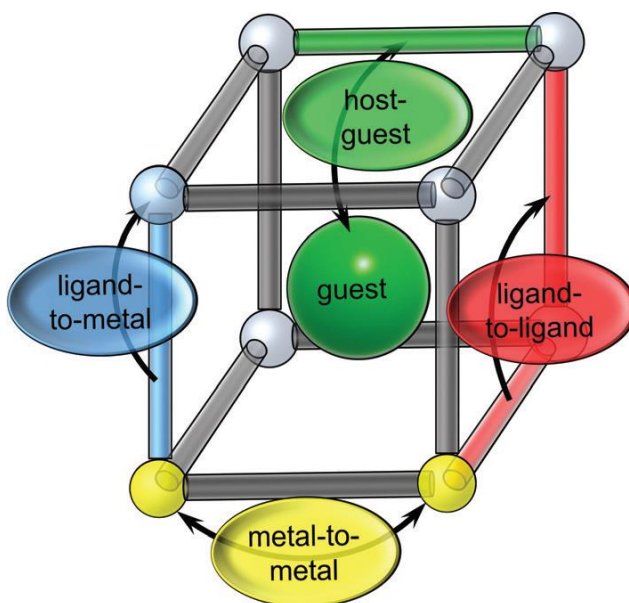
$$k^{\text{Förster}} = \frac{|\mu_A|^2 |\mu_D|^2 \kappa^2}{\hbar^2 R^6} \int_{-\infty}^{\infty} \bar{\sigma}_A(\omega) \bar{\sigma}_D(\omega) d\omega \quad (21)$$

This is the equation typically used for determining the Förster rate, and which is employed throughout the rest of this chapter. As can be seen from Equation 21, optimizing the rate of Förster energy transfer in materials like metal organic frameworks will require careful attention to the choice of chromophore and framework symmetry as well as other parameters like fluorescence quantum yield and chromophore oscillator strength. The key challenge is that all of this must be performed without sacrificing the integrity of MOF structure or introducing defects that may unproductively trap excitons.⁹

4.2 Why MOFs

Metal-Organic Frameworks (MOFs), sometimes referred to as porous coordination polymers, have wide-ranging applications in light-harvesting, luminescence, artificial photosynthesis, photocatalysis and photovoltaic as hybrid materials.⁹⁻¹³ Understanding the exciton transport process within well-defined 3D solid phases will aid in the design of novel materials for highly efficient directional energy transport. MOFs offer a rich diversity of unique platforms to study energy transfer (ET). Highlighted by highly-ordered crystal structure and synthetic tunability via crystal engineering, MOFs allow for precise control of distances and angles between chromophores and their alignment by judicious choice of ligands and metal nodes. The main ET

pathways observed in MOF matrices could occur between different ligands, from ligand to metal centers (or metal to ligand), metal to metal nodes and guest to MOF skeleton, as shown in Scheme 1.¹⁴



Scheme 1. A schematic representation of different ET processes which could occur in a MOF matrix.¹⁴

The aim of this chapter is to give a comprehensive overview of MOF materials for energy transfer. Because the composition of bridging linkers and inorganic nodes can significantly affect the ET process within MOFs, herein, we will discuss ET mechanisms and structural motifs in MOFs based on different types of energy donor/acceptors. In general, four scenarios can be distinguished in reported studies:

1. MOFs containing lanthanide metal ion, either as the metal nodes of the framework or trapped in the MOF pores as guest cations.
2. Doping well-known transition-metal complexes, $\text{Ru}(\text{bpy})_3^{2+}/\text{Os}(\text{bpy})_3^{2+}$ as the chromophores in Zn/Zr based MOFs.

3. MOF materials constructed from porphyrins and metalloporphyrins as crystalline powders or thin films.
4. Using organic chromophores as bridging linkers to prepare designed MOFs.

In summary, to construct a MOF system to probe ET, several criteria need to be considered:

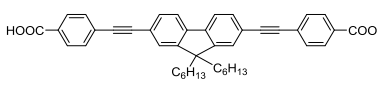
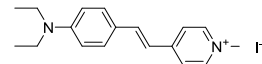
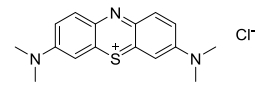
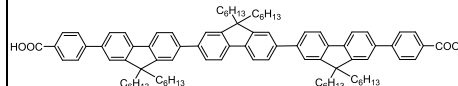
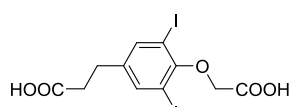
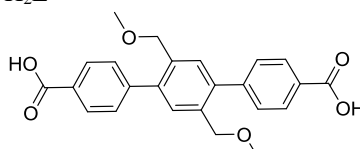
1. The chromophores should have intense absorption and emission bands in UV-Vis range and relatively long emission lifetimes in order for the photoexcitation and excited-state dynamics to be easily probed.
2. Good overlap between the emission spectrum of the donor and the absorption spectrum of acceptor are necessary to favor the ET process.
3. The energy transfer efficiency depends on the donor/acceptor ratios and highly efficient and rapid directional ET is desired for further applications.
4. It is advantageous to choose well-studied molecular chromophores, in which the photophysical and photochemical properties in solution are well established in order to model the more complicated solid-state photodynamic processes and ET mechanisms in a MOF matrix.

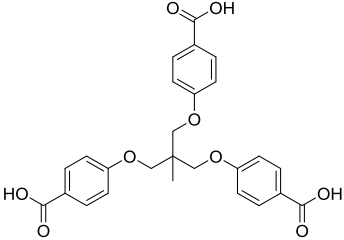
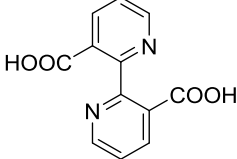
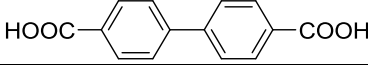
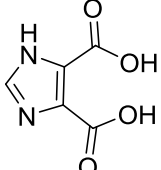
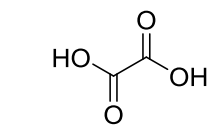
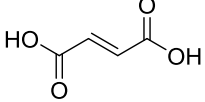
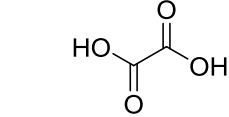
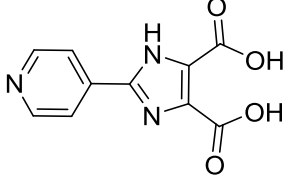
4.3 Lanthanide-based Luminescent MOFs

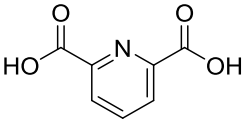
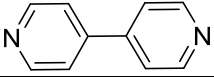
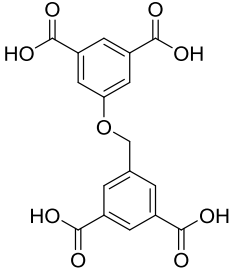
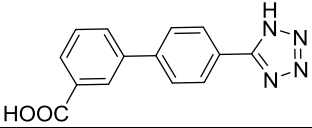
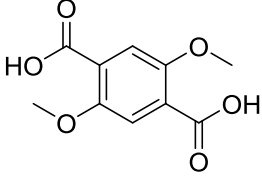
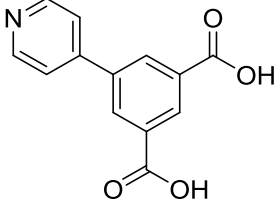
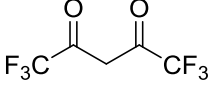
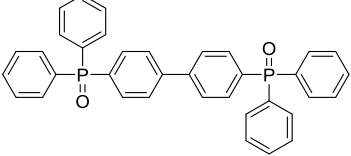
Luminescent lanthanide-based materials have been widely used in light-emitting systems and biological, environmental and clinical analysis owing to the unique luminescence that results from intra-4f transitions of Ln^{3+} . Characterized by sharp emission bands, long excited-state lifetimes and large Stokes shifts,¹⁵ Ln^{3+} ions provide sufficient band gaps between their 4f states. Gd^{3+} can emit in the UV region, Sm^{3+} , Eu^{3+} , Tb^{3+} , Dy^{3+} and Tm^{3+} are useful luminescence centers in visible light range, while Nd^{3+} , Yb^{3+} , Er^{3+} and to a lesser extent Pr^{3+} , Sm^{3+} , Dy^{3+} , Ho^{3+} , Tm^{3+} in near-

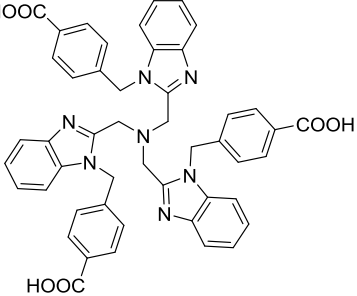
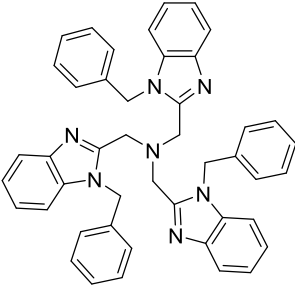
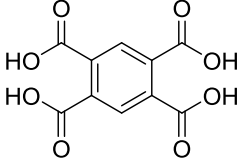
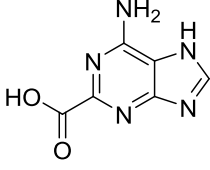
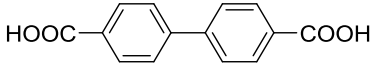
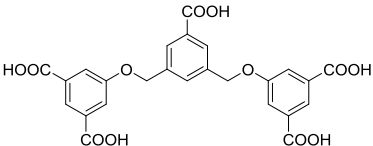
infrared region.¹⁶ Although the photoluminescence of lanthanide ions is an efficient process, intra-4f transitions are “Laporte forbidden”, and therefore, light absorption by direct 4f excitation is weak and results in low intensity luminescence.^{15, 17} This problem can be overcome in Ln-based MOF systems, where the organic ligands can be utilized as antennas for the metal ions. The effect that the organic chromophores absorb the light and funnel the excitation energy to Ln³⁺ is known as antenna effect or sensitization. Furthermore, ET processes from metal-to-metal in heterometallic Ln-MOFs can be used to tune the photoluminescence properties. Overall, two strategies have been used to probe ET in Ln³⁺-MOFs: (1) MOFs with Ln³⁺ metal nodes and (2) MOFs with encapsulated Ln³⁺ in the pores.

Table 1. Summary of chromophores in lanthanide-based MOFs

MOF	Chemical Formula	Ligand Structure	Guest	Ref
Ln(III)-L (Ln=Gd, Eu, Yb)	Gd(L) _{1.5} ·DMF·H ₂ O	L= 	D1=  D2= 	[18]
Ln ₂ (L1) ₃ ·(DMF) _x ·(H ₂ O) _y (x, y=1-2) (Ln=Gd, Eu, Yb)	Eu(L1) _{1.5} ·(DMF) _{1.1} ·(H ₂ O) _{1.7}	H ₂ L1 = 		[19]
Eu-MOF	Eu·L·5H ₂ O	L = 		[20]
Ln-MOF	[Eu ₂ L ₃ (H ₂ O) ₄]·3DMF	H ₂ L = 	DMF (MOF 1) H ₂ O (MOF 2)	[21]

LnL	$\text{Ln}_x\text{Gd}_{1-x}\text{L}$ (Ln = Tb, Yb)	L = 		[22]
Ln-MOFs	$\{[\text{Ln}_4(\mu_3\text{OH})_4(\text{BPDC})_3(\text{BPDCA})_{0.5}(\text{H}_2\text{O})_6]\text{ClO}_4 \cdot 5\text{H}_2\text{O}\}_\infty$ (Ln = Tb, Gd)	BPDC =  BPDCA = 		[23]
	$\text{K}_5[\text{Ln}_5(\text{IDC})_4(\text{ox})_4]$ (Ln = Gd, Tb, Dy)	IDC =  Ox = 		[24]
	$\text{Eu}_2(\text{FMA})_2(\text{OX})(\text{H}_2\text{O})_4 \cdot 4\text{H}_2\text{O}$	FMA =  Ox = 		[25]
	$\{[\text{Tb}_3(\mu_3\text{-HPyIDC})_4(\text{H}_2\text{O})_8] \cdot \text{NO}_3 \cdot 4\text{H}_2\text{O}\}_\infty$	H ₃ PyIDC = 		[26]

$[(\text{Tb}_{1-x}\text{Eu}_x)\text{-(DPA)-}(\text{HDPA})]_{\infty}$	$[(\text{Tb}_{0.95}\text{Eu}_{0.05})(\text{DPA})(\text{HDPA})]_{\infty}$ $[(\text{Tb}_{0.5}\text{Eu}_{0.5})(\text{DPA})(\text{HDPA})]_{\infty}$	$\text{H}_2\text{DPA} =$ 		[27]
${}^2[\text{Ln}_2\text{Cl}_6(\text{bipy})_3]_{\infty} \cdot 2\text{bipy}$	${}^2[\text{Gd}_{2-x}\text{Eu}_x\text{Tb}_y\text{Cl}_6(\text{bipy})_3]_{\infty} \cdot 2\text{bipy}$ $(0 \leq x, y \leq 0.5)$	$\text{bipy} =$ 		[30]
LnL $(\text{Ln} = \text{La}, \text{Ce}, \text{Pr}, \text{Nd}, \text{Sm}, \text{Eu}, \text{Gd}, \text{Tb}, \text{Ho}, \text{Er})$	$\{[\text{Ln}_2(\text{L}_2)] \cdot (\text{H}_2\text{O})_3 \cdot (\text{Me}_2\text{NH}_2)_2\}_{\infty}$	$\text{H}_4\text{L} =$ 		[31]
Ln-Zn $(\text{Ln} = \text{Eu}, \text{Tb})$	$\{[\text{LnOH}(\text{H}_2\text{O})_6][\text{Zn}_2\text{Ln}_4(\text{H-Htbca})_2(4\text{-tbca})_8(\text{H}_2\text{O})_{12}]\}_{\infty} \cdot 6n\text{H}_2\text{O}$	$4\text{-H}_2\text{tbca} =$ 		[32]
Ln-DMBDC $(\text{Ln} = \text{Tb}, \text{Eu})$	$(\text{Eu}_x\text{Tb}_{1-x})_2(\text{DMBDC})_3(\text{H}_2\text{O})_4 \cdot \text{DMF} \cdot \text{H}_2\text{O}$	$\text{DMBDC} =$ 		[33]
LnPIA $(\text{Ln} = \text{Tb}, \text{Eu})$	$(\text{Eu}_x\text{Tb}_{1-x})(\text{PIA})(\text{HPIA})(\text{H}_2\text{O})_{2.5}$	$\text{H}_2\text{PIA} =$ 		[34]
$[\text{Ln}(\text{hfa})_3(\text{dpbp})]_n$ $(\text{Ln} = \text{Tb}, \text{Eu})$	$[\text{Tb}_{0.99}\text{Eu}_{0.01}(\text{hfa})_3(\text{dpbp})]_{\infty}$	$\text{hfa} =$  $\text{dpbp} =$ 		[35]

Eu(III)-MOF (1) Eu(III)-Zn(II)-MOF(2)	[Eu(triCBNTB)] ·DMAc·4H ₂ O (1) [EuZn(triCB-NTB) (H ₂ O)(Cl) ₂]·2DMAc·H ₂ O (2)	triCB-NTB = 		[36]
2-Ln-Ag (Ln=Gd, Eu)	[LnAg ₃ (3-TPyMNTB) ₂ (H ₂ O)(MeCN)](ClO ₄) ₆ · 4MeCN Ln=Gd, Eu	TPyMNTB = 		[37]
	[NH ₄] ₂ [ZnL]·6H ₂ O	L = 	Ln = Eu ³⁺ , Tb ³⁺	[38]
Ln ³⁺ @bio-MOF-1 Ln=Tb, Sm, Eu, Yb	[Zn ₈ (ad) ₄ (BPDC) ₆ O· 2Me ₂ NH ₂ , 8DMF, 11H ₂ O]	ad =  BPDC = 	Ln=Tb, Sm, Eu, Yb	[39]
Ln ³⁺ @Zn(II)-MOF Ln = Tb, Eu	[Zn ₂ (L)·H ₂ O]·3H ₂ O· 3DMAc·NH ₂ (CH ₃) ₂ ∞	L = 	Ln = Tb, Eu	[40]

4.3.1 Energy transfer in Ln-node based MOF

The long-range ordered organization of photophysically active units at supramolecular level on nano- to micrometer scale is important in energy-transfer processes in photosynthetic systems, as well as electronic devices based on organic compounds. Self-assembly provides an efficient and inexpensive way for assembling large numbers of molecules into structures that can bridge length

scales from nanometers to macroscopic dimensions. Two examples of Ln-node based MOFs constructed by self-assembly exhibited efficient light-harvesting properties by using linear π -conjugated ligand with high fluorescence quantum yield.¹⁸⁻¹⁹ In these MOFs, ligand-to-ligand energy transfer (LLET) was exploited to extend the absorption spectrum of the MOFs and tune the emission properties.

Uvdal and coworkers prepared MOFs that display 1D channels through the self-assembly of π -conjugated dicarboxylate linkers (L) and $\text{Ln}(\text{OAc})_3$ ($\text{Ln} = \text{Gd}, \text{Eu}, \text{Yb}$) in DMF.¹⁸ These nanoscale MOFs have Ln^{3+} metal clusters that can bind to solvent or small anions when the main ligands do not saturate the high coordination number of the lanthanide ion. This results in a negatively charged local environment around the metal node. Therefore, cationic guest molecules such as trans-4-[4'-(N,N- diethylamino)styryl]-N-methyl pyridinium iodide (D1) and methylene blue (MB^+) (D2) can be encapsulated into the MOF channels and the loading amount can be controlled by reaction temperature. For example, in the Gd^{3+} -L MOF, the guest loading amount based on ligand L can be up to ~6.7 mol% for D1 and ~2.8 mol% for D2 at 140 °C. More interestingly, the guest encapsulated in MOFs at 140 °C can be released gradually at room temperature in DMF and this process is reversible (Scheme 2).¹² Photoluminescence and fluorescence lifetime decay studies showed that the D1-loaded MOFs exhibit efficient light harvesting with ET from the framework to the guest molecule. As shown in Figure 5, the emission peak of L has large overlap with the absorption spectrum of D1. When L mixed with D1 in a homogeneous DMF solution at a molar ratio of 1:2, the emission of L was quenched but no ET could be observed (Figure 5, curve b). The authors postulate that this was due to favorable collisional electron transfer and/or the formation of nonemissive aggregates. With the addition of $\text{Gd}(\text{OAc})_3$ and MOF self-assembly, emission from D1 at ~580 nm appeared upon MOF excitation at 365 nm, which is optimal

excitation of L (Figure 5, curves c and d). Therefore, MOF incorporation and chromophore isolation led to efficient ET between the donor L with the acceptor D1, not observed in homogeneous solution. It is important to note that in this case the Gd^{3+} did not play an active role in the ET chain. The main role of the Gd^{3+} was to organize and isolate the chromophores in 3D space, thus preventing electron transfer and/or the formation of nonemissive aggregates.

Scheme 2. Schematic illustration of the light-harvesting lanthanide MOFs with L that exhibit reversible temperature-dependent encapsulation and release of acceptor molecules D1.¹²

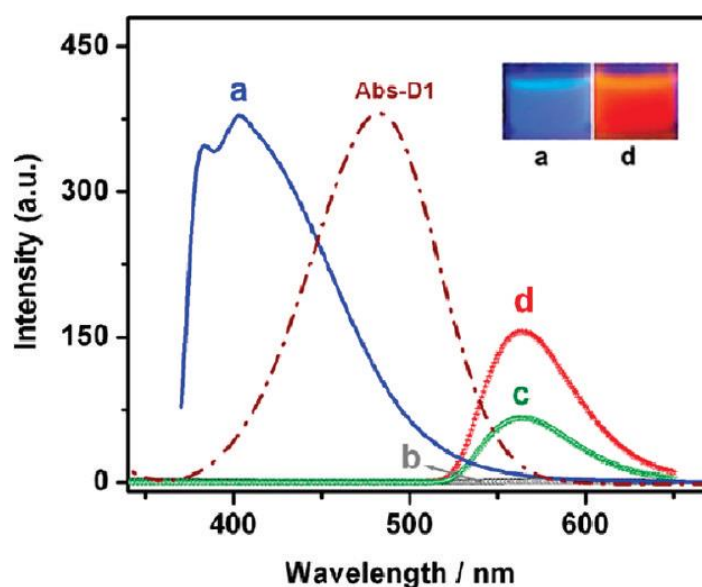


Figure 5. PL spectra of L (a), L + D1 (b), and L + D1 + $Gd(OAc)_3$ prepared at 20 °C (c) and 140 °C (d) in DMF. All of the samples have the same concentrations of L; samples b, c, and d have the same concentration of D1. The dotted line is a UV-vis spectrum of D1 in DMF. Inset: photo images of samples (a) and (d) under UV light (365 nm).¹⁸

LLET is not only limited in the host-guest system, but also can be observed in the frameworks with mixed ligand. Compared with encapsulation, which occurs by weak noncovalent interactions, strong coordination between metal and ligand can preferentially orient the linker components to enhance ET efficiency. Stable 3D networks were constructed by lanthanide ions ($Ln = Gd, Eu, Yb$) and a series of different π -conjugated dicarboxylate ligands with different side-chain lengths

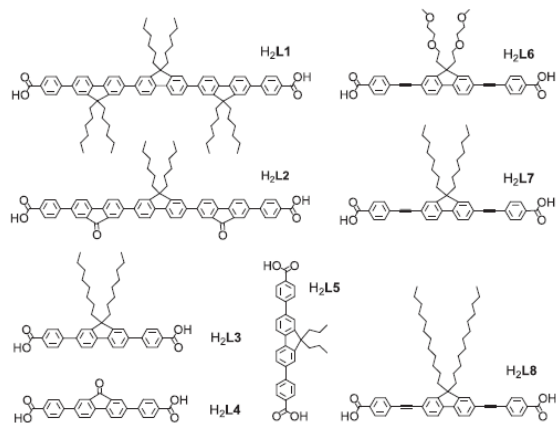


Figure 6. Chemical structures of the ligands with different -conjugation lengths and differing side chains.¹⁹

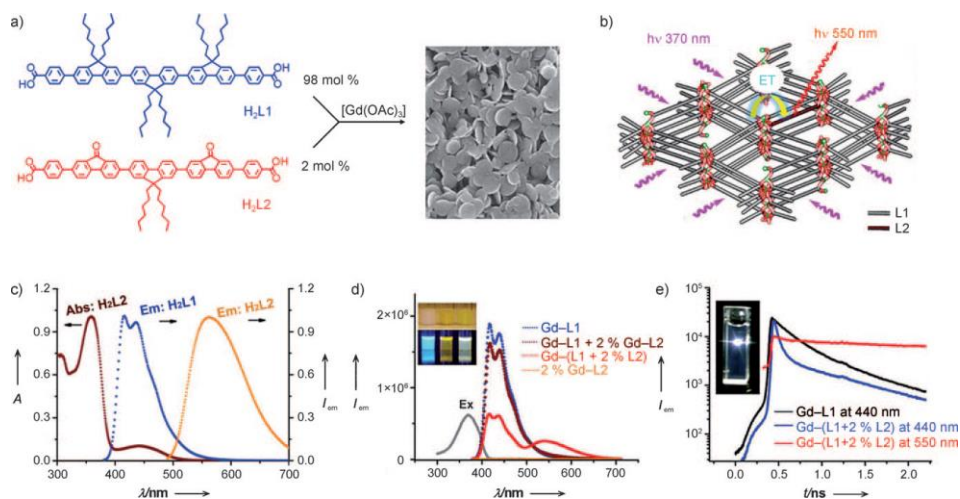


Figure 7. Synthesis and light harvesting study of multicomponent nanoparticles: a) Illustration showing the preparation of Gd-L1-L2 multicomponent nanoparticles. b) Schematic representation of the energy transfer in long-range ordered MOFs. c) Normalized absorption and emission spectra of H₂L1 and H₂L2 in DMF. d) Emission spectra of Gd-L1, Gd-L1 mixed with 2 mol% Gd-L2, Gd-(L1+2 mol% L2), and Gd-L2 nanoparticles. The gray curve is the excitation spectrum of Gd-(L1+2 mol% L2) nanoparticles; inset (from left to right): photo-images of Gd-L1, Gd-L2, and Gd-L1-L2 nanoparticles in daylight (upper row) and under an ultraviolet lamp (365 nm; bottom row). e) Time-resolved fluorescence decay of Gd-L1, Gd-L2, and Gd-(L1+2 mol% L2). Inset: photo-image of Gd-(L1+2 mol% L2) nanoparticles under excitation by laser (370 nm).¹⁹

(Figure 6).¹⁹ The long alkyl chains in the ligand prevent aggregation of the nanoparticles, while the absorption and fluorescence of the MOFs can be tuned by using different monomeric units.

The structural similarity in the main chain of the ligands ensured that the forces between dicarboxylate linkers and Ln metal ions are approximately similar and lead to the same crystal structure for designed MOFs. Doping H₂L₂ into Ln-L₁ MOFs afforded efficient Förster resonance ET (FRET) from L₁ to L₂ within the framework, and did not alter the MOF structure (Figure 7). The excitation spectrum and time-resolved fluorescence decay of Gd-L₁-L₂ nanoparticle dispersions in DMF confirmed the ET from L₁ to L₂ under the photo-irradiation at 365/370 nm. The ET from L₁ to L₂ is evidenced by the apparent quenching for strong emission of Gd-L₁ and the concomitant increase in the acceptor emission L₂ at 550 nm when excited at the 365 nm (the absorption maximum of donor L₁) (Figure 7d). Similar FRET process from L₃ to L₄ can be observed in Gd-L₃-L₄ system where 1% mol of H₂L₄ was doped in Gd-L₃ MOF. Moreover, very efficient sensitization of Eu(III) has also been observed by replacing Gd with Eu in Gd-L₃ MOF, characterized by the efficient emission quenching of L₃ by Eu(III). In a model MOF, Gd(III)_{0.95}-Eu(III)_{0.05}-L₃_{1.47}-L₄_{0.03}, the acceptor ligand, L₄, and the Eu³⁺ ion can be co-sensitized by the same donor, L₃, revealed by multiband emissions which covered the characteristic emission band from Eu³⁺ and L₄ under the excitation of L₃. The multicomponent nano-MOFs could potentially be used for barcodes and FRET-based sensors.

To further enhance the efficiency of LMET, photophysical properties can be modulated through the heavy atom effect (HAE). To briefly introduce this concept, the spin configuration of ligand and Ln³⁺ excited states must be considered. Upon the irradiation of light, organic chromophores form singlet excited states. The excited states of Ln³⁺ ions are formally triplets. Therefore, to promote efficient ET between spin-conserved states, the organic chromophore must first intersystem cross (ISC) to its triplet state. When the energy gap between singlet excited and triplet excited states of the ligand is greater than 5000 cm⁻¹, the ISC process will be effective in

accordance with Reinholdt's empirical rule. The HAE enhances spin-orbit coupling between the singlet and triplet states. Therefore, ISC is favored in the presence of heavy atoms, such as iodine or bromine. Jayakannan and coworkers investigated the HAE concept using iodo-substituted carboxylic ligands to build 1D and 3D MOFs with Eu^{3+} .²⁰ Close packing of the bisiodo ligand in the solid state through π - π stacking restricted vibrational relaxation, reduced the radiative decay through S_1 to S_0 transition and promoted the population of triplet states by ISC, which further facilitated LMET from the ligand triplet excited state (T) to the metal ion ($5D_0$ for Eu^{3+}) in the Eu-MOFs (Figure 8).

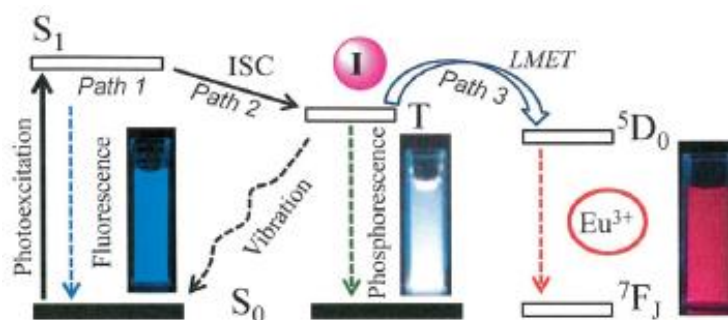


Figure 8. The HAE-assisted ligand to metal energy transfer (LMET) concept.²⁰

The efficiency of LMET in Ln-based MOFs could be modulated by small guest molecules and ions in the pores of the MOF matrix, leading to the change of its luminescence properties, making these materials promising platforms for sensing applications. The interaction between the guest molecules with the ligand could either enhance or quench the luminescence of the MOF, which provides a significant difference for desired detection. Song and coworkers prepared a luminescent lanthanide MOF, which can selectively detect DMF vapor. The 3D MOF $[\text{Eu}_2\text{L}_3(\text{H}_2\text{O})_4] \cdot 3\text{DMF}$ was synthesized by heating of 2',5'-bis(methoxymethyl)-[1,1':4',1''-terphenyl]-4,4''-dicarboxylate and $\text{Eu}(\text{NO}_3)_3$ in DMF/ H_2O .²¹ As shown by X-ray crystal analysis, DMF is located in the solvent channel along the a-axis in the framework, which can be replaced by water to form an isostructural

MOF. The MOF with H₂O in the pores exhibited fast response rates to DMF, revealed by the significant increase of luminescence intensity. This DMF sensitization is caused by DMF-ligand interactions that presumably shift the energy level of excited ligand and facilitates the LMET process. Similarly, a family of Ln-MOFs can effectively sense acetone molecules based on fluorescence quenching.²² Ln-MOF {[Tb₄(μ₃-OH)₄(BPDC)₃(BPDCA)_{0.5}(H₂O)₆]ClO₄·5H₂O}_∞, where BPDC²⁻ = 3,3'-dicarboxylate-2,2'-dipyridine anion and BPDCA²⁻ = biphenyl-4,4'-dicarboxylate anion, could sensitively detect small molecules and ions especially benzene, acetone, Cu²⁺ and CrO₄²⁻.²³ An anionic MOF K₅[Tb₅(IDC)₄(ox)₄] (IDC, imidazole-4,5-dicarboxylate, ox, oxalate) had a selective response with enhanced emission when guest K⁺ exchanged with Ca²⁺.²³ Qian and coworkers reported a microporous luminescent MOF, Eu₂(FMA)₂(OX)-(H₂O)₄·4H₂O (FMA, fumarate; OX, oxalate) that exhibited highly selective and sensitive sensing of Cu²⁺ in aqueous solution (Figure 9).²⁴ Zhang and coworkers prepared Tb(III)-based MOF using a blue emitting ligand 2-(4-pyridyl)-1H-imidazole-4,5-dicarboxylic acid (H₃PyIDC), which showed good selectivity and sensitivity toward Fe³⁺ in water.²⁵ Finally, as an example of competitive absorption, a family of Ln-MOFs has been shown to effectively sense acetone molecules based on fluorescence attenuation caused by the overlap absorption between acetone and the ligand.²⁶

Synthetically, it is easy to get isostructural Ln-based MOF using mixed lanthanide metal ion. Therefore, metal-to-metal energy transfer (MMET) has been widely used to tune the emission color of designed MOFs without altering the structure, especially the MMET between Tb³⁺ and Eu³⁺. The emission color can be quantitatively characterized by using the color coordinates according to the Commission Internationale de L'Eclairage (CIE) 1931 diagram.²⁷⁻²⁸ The CIE

XYZ color space was derived from a series of experiments done in the late 1920s by William²⁷ and John²⁸, and the coordinates x and y represent red and green color components, respectively.

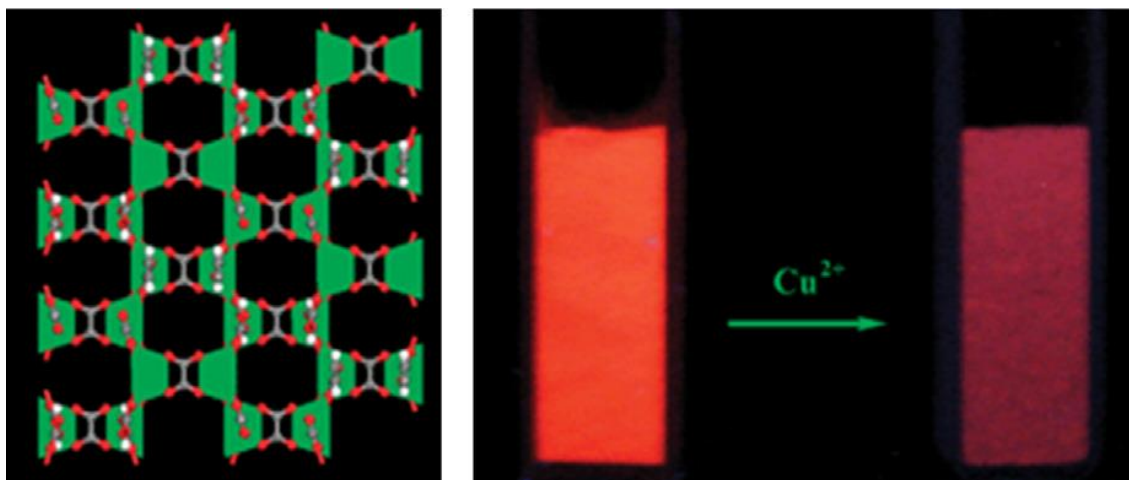


Figure 9. (Left) X-ray single crystal structure of MOF $\text{Eu}_2(\text{FMA})_2(\text{OX})(\text{H}_2\text{O})_4 \cdot 4\text{H}_2\text{O}$. (Right) The luminescence change after the addition of Cu^{2+} (10^{-2} M) on MOF under UV light.²⁵

Rodrigues *et al.* reported a complementary experimental and theoretical investigation of the ET mechanism between $\text{Tb}^{3+} \rightarrow \text{Eu}^{3+}$ in two isomorphous 2D heterometallic lanthanide-organic frameworks,²⁹ $[(\text{Tb}_{0.95}\text{Eu}_{0.05})(\text{DPA})(\text{HDPA})]_{\infty}$ (1) and $[(\text{Tb}_{0.5}\text{Eu}_{0.5})(\text{DPA})(\text{HDPA})]_{\infty}$ (2), where H_2DPA is pyridine 2,6-dicarboxylic acid. Steady-state emission spectra of both MOF samples showed the high quenching effect on Tb^{3+} emission caused by Eu^{3+} ion indicating an efficient $\text{Tb}^{3+} \rightarrow \text{Eu}^{3+}$ ET. The $\text{Tb}^{3+} \rightarrow \text{Eu}^{3+}$ ET rates (k_{ET}) for (1) and (2) and rise rates (kr) of the Eu^{3+} ion for (1) were investigated at different temperatures. kr and k_{ET} for (1) were on same order of magnitude, indicating that the sensitization of the $\text{Eu}^{3+} {}^5\text{D}_0$ level is driven by the ET from ${}^5\text{D}_4$ of Tb^{3+} ion. The $\text{Tb}^{3+} \rightarrow \text{Eu}^{3+}$ ET efficiency η_{ET} and R_0 values in (1) varied between 67~79% and in between 7.15~7.93 Å, whereas for (2) the ET occurs on average with η_{ET} and R_0 of 97% and ca. 31 Å, respectively. The role of the dipole–dipole (d–d), dipole–quadrupole (d–q), quadrupole–quadrupole (q–q), and exchange (Ex) mechanisms in ET processes were estimated by Malta’s

model. ET rate values for a single $\text{Tb}^{3+} \rightarrow \text{Eu}^{3+}$ process are lower than those experimentally obtained; however, it may be justified by the fact that theoretical model that does not consider the role of phonon assistance in the $\text{Tb}^{3+} \rightarrow \text{Eu}^{3+}$ ET. The ET processes investigated were predominantly governed by d-d and d-q mechanisms.

In a series of isotopic, 2D MOFs, $[\text{Gd}_{2-x}\text{Eu}_x\text{Tb}_y\text{Cl}_6(\text{bipy})_3] \cdot 2\text{bipy}$ (Figure 10A), where $0 \leq x, y \leq 0.5$, $\text{bipy} = 4,4'$ -bipyridine, the emission color in-between green and red can be tuned.³⁰ Specifically, 4,4'-bipyridine functions as an antenna, providing the $\text{T}_1 \rightarrow 4\text{f}$ LMET to Eu^{3+} and Tb^{3+} , giving a red luminescence for Eu^{3+} and a green luminescence for Tb^{3+} , respectively. Since the $^5\text{D}_x$ excited states of Eu^{3+} and Tb^{3+} are very close to the T_1 state of the ligand, efficient ET from T_1 to $^5\text{D}_x$ through non-radiative relaxation significantly reduced the energy back-transfer (Figure 11). Different ratios of Eu^{3+} and Tb^{3+} can be incorporated into the MOF by mixing their metal salts with GdCl_3 under solvent-free melt conditions of 4,4'-bipyridine. The introduction of Gd^{3+} into the MOF matrix hindered back energy transfer due to the large energy gap between the excited state and ground state of Gd^{3+} (Figure 10B & C). The combination of Eu^{3+} and Tb^{3+} lead to MMET from $\text{Tb}^{3+} \rightarrow \text{Eu}^{3+}$, which could tune the emission color (Figure 10D).

Zang's group synthesized a series of isostructural lanthanide MOFs, LnL ($\text{Ln} = \text{La}, \text{Ce}, \text{Pr}, \text{Nd}, \text{Sm}, \text{Eu}, \text{Gd}, \text{Tb}, \text{Ho}, \text{Er}$), under solvothermal conditions using flexible multicarboxylic acid ($\text{H}_4\text{L} = 5$ -(3,5-dicarboxybenzyloxy)-isophthalic acid). Efficient ET from the ligand to Tb^{3+} or Eu^{3+} was observed.³¹ The emission from the Eu^{3+} center was further sensitized by Tb^{3+} and the colors can be controlled by adjusting the molar ratio between them. White light emission was achieved by combination of the blue emission of the ligand and the intense emissions of lanthanide ions (Figure 12). The corresponding international commission on illumination (CIE) coordinates of the MOFs,

(0.330, 0.334) and (0.332, 0.338), for $\text{Eu}_{0.17}\text{Tb}_{0.18}\text{La}_{0.65}\text{L}$ and $\text{Eu}_{0.16}\text{Tb}_{0.19}\text{La}_{0.65}\text{L}$, respectively, are very close to the coordinates for ideal white-light (0.333, 0.333).

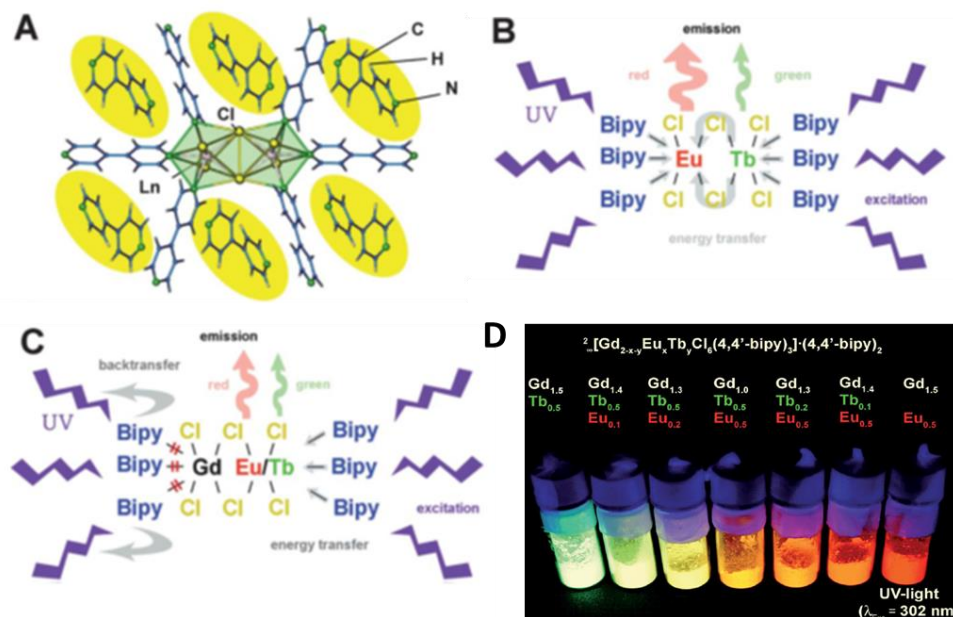


Figure 10. A. Depiction of the connectivity in the 2D layer structure of $^2[\text{Ln}_2\text{Cl}_6(\text{bipy})_3] \cdot 2\text{bipy}$. B & C. Schematic depiction of the energy transfer processes between metal ions and ligands. D. Photoluminescence of the series of solid solutions of $^2[\text{Gd}_{2-x-y}\text{Eu}_x\text{Tb}_y\text{Cl}_6(\text{bipy})_3] \cdot 2\text{bipy}$ under UV light ($\lambda = 302 \text{ nm}$).³⁰

Similarly, two novel isostructural Ln-Zn (Ln=Eu and Tb) heterometallic frameworks have been prepared by 4-(1H-tetrazol-5-yl)-biphenyl-3-carboxylic acid (4-H₂tbca) under hydrothermal conditions.³² Both Eu-Zn and Tb-Zn MOFs showed characteristic red and green luminescence, respectively, due to antenna effect from the ligand. Remarkably, the photoluminescence spectra indicated that, not only can the ligand in Tb-Zn MOF transfer energy to Tb³⁺ centers to emit green light, but it can also maintain effective blue luminescent properties of the 4-H₂tbca ligand. Therefore, additional doping of Eu³⁺ into Tb-Zn MOF can tune the luminescence from green to red towards white. The CIE coordinates of the emission spectra of 0.4% to 1.5% Eu³⁺-doped Tb³⁺ MOFs fall in the white-region. When the doped ratio of Eu³⁺ is 0.5%, nearly ideal white light

emission with the CIE coordinate of (0.331, 0.328), a high color rendering index (CRI) value of 81.7 and a favorable correlated color temperature (CCT) magnitude of 5562K was achieved.

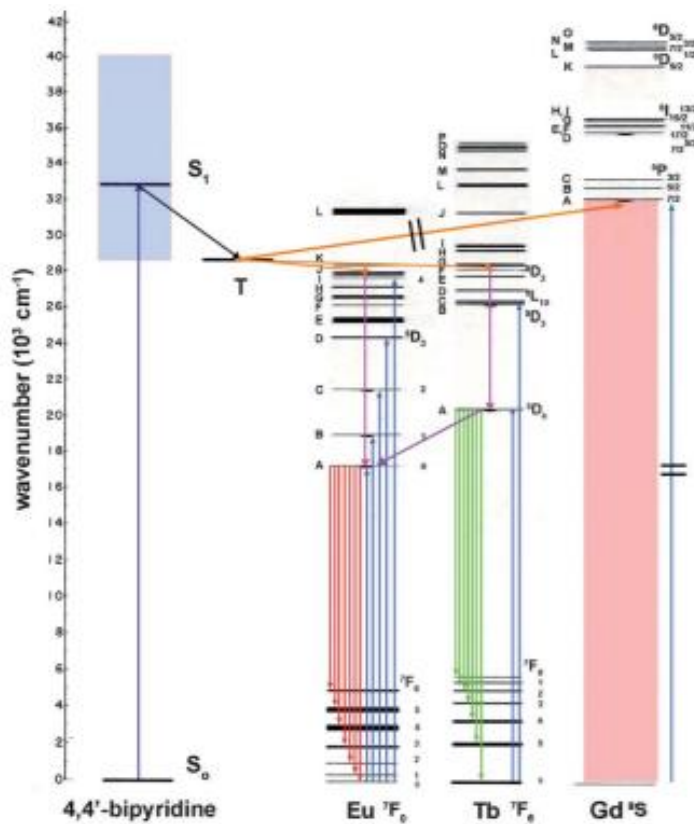


Figure 11. Excitation and emission process between metal ions and ligands in ${}^2[\text{Gd}_{2-x}\text{Eu}_x\text{Tb}_y\text{Cl}_6(\text{bipy})_3] \cdot 2\text{bipy}$.³⁰

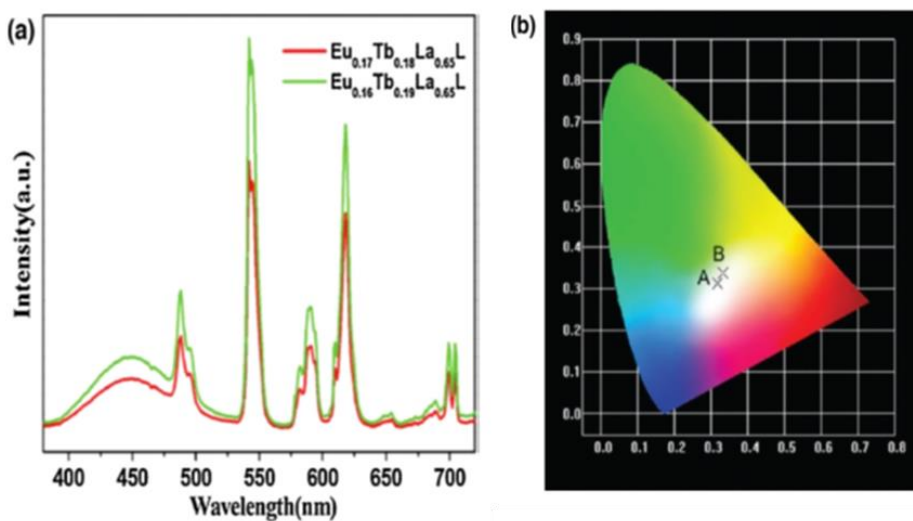


Figure 12. (a) PL emission spectra of the Eu/Tb doped La compound ($\lambda_{\text{ex}} = 367$ nm, solid samples). (b) CIE chromaticity diagram for $\text{Eu}_{0.17}\text{Tb}_{0.18}\text{La}_{0.65}\text{L}$ (A) and $\text{Eu}_{0.16}\text{Tb}_{0.19}\text{La}_{0.65}\text{L}$ (B).³¹

Mixed lanthanide MOFs can also act as luminescent thermometer since some of those frameworks exhibited temperature-dependent luminescence. Qian, Chen and coworkers reported two isostructural 3D MOFs Tb-DMBDC and Eu-DMBDC using 2,5-dimethoxy-1,4-benzenedicarboxylate (DMBDC) as the organic linker.³³ Owing to the sensitization effect from DMBDC, LMET to Tb^{3+} lead to green emission at 545 nm and LMET to Eu^{3+} lead to red emission at 613 nm. By increasing the temperature from 10 K to 300 K, the emission intensities gradually decreased due to the thermal activation of non-radiative decay. Intriguingly, the mixed doped MOF $\text{Eu}_{0.0069}\text{Tb}_{0.9931}$ -DMBDC exhibited unique temperature-dependent luminescence behavior that differed from Tb-DMBDC and Eu-DMBDC. With the increase of temperature, the probability of $\text{Tb}^{3+} \rightarrow \text{Eu}^{3+}$ ET was significantly enhanced. Therefore, at 10 K, the emission bands of Eu^{3+} and Tb^{3+} have comparable intensity, while at 300 K, the emission of Eu^{3+} dominates the overall luminescence color. Additionally, a linear correlation between temperature and emission intensity ratio in $\text{Eu}_{0.0069}\text{Tb}_{0.9931}$ -DMBDC was observed from 50 to 200 K, which indicated that the MOF is an excellent candidate for self-referencing luminescent thermometers (Figure 13). A follow up study reported $\text{Tb}_{0.9}\text{Eu}_{0.1}\text{PIA}$ ($\text{H}_2\text{PIA} = 5$ -(pyridin-4-yl)isophthalic acid) as a luminescent thermometer whose sensitivity is more than nine times higher than $\text{Eu}_{0.0069}\text{Tb}_{0.9931}$ -DMBDC in an even boarder temperature range of 100 to 300 K, due to the higher triplet-state energy of the ligand.³⁴ Similarly, Hasegawa and coworkers reported $[\text{Tb}_{0.99}\text{Eu}_{0.01}(\text{hfa})_3(\text{dpbp})]_n$ (dpbp: 4,4'-bis(diphenylphosphoryl) biphenyl) as a novel thermosensor over a wide range of 200 to 500 K with high sensitivity ($0.83\% \text{ } ^\circ\text{C}^{-1}$).³⁵

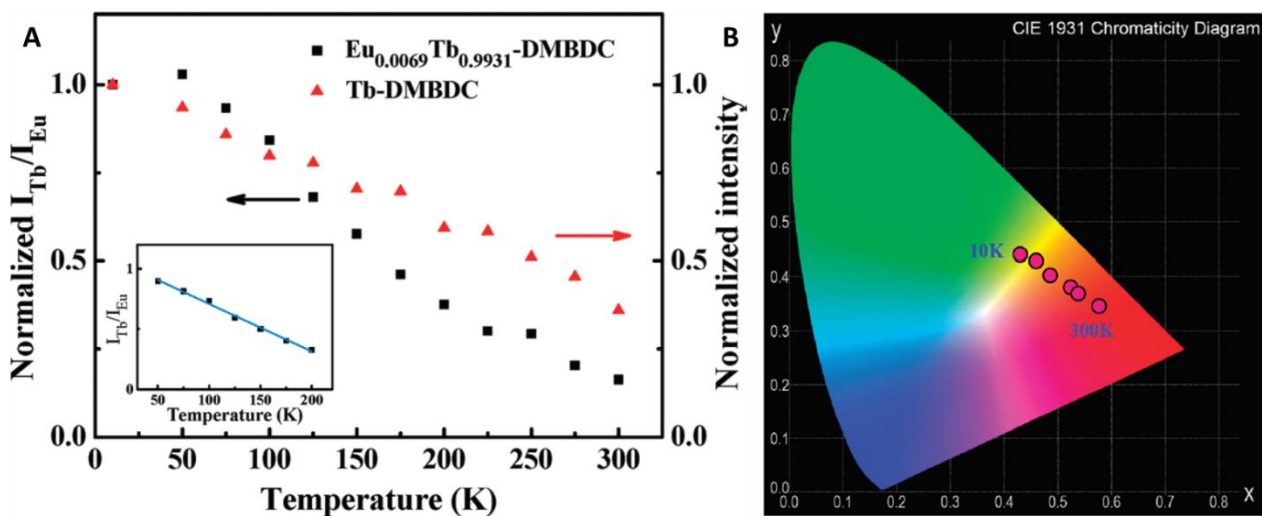
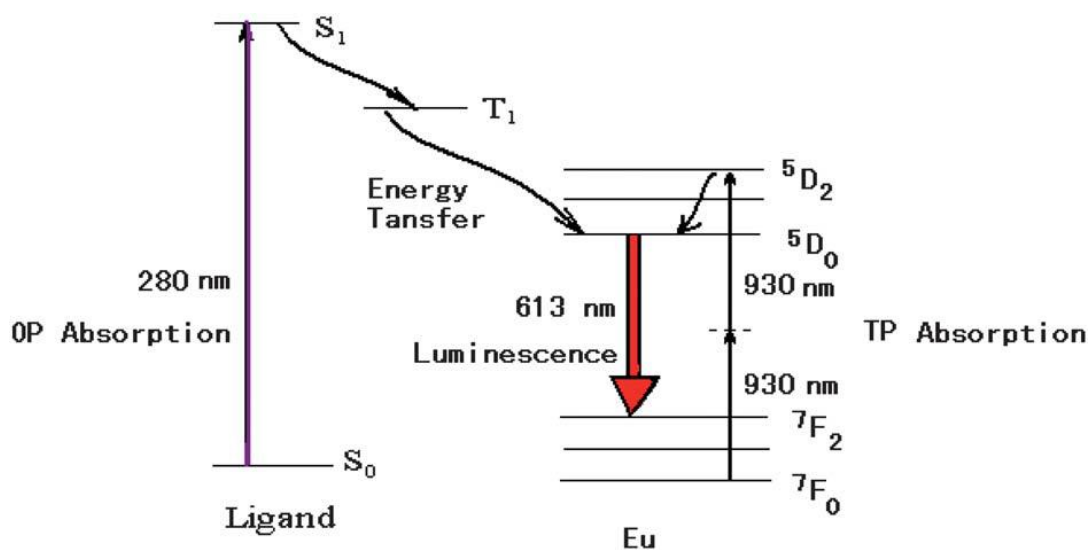


Figure 13. A. Temperature dependence of the integrated intensity ratio of Tb^{3+} (545 nm) to Eu^{3+} (613 nm) for $\text{Eu}_{0.0069}\text{Tb}_{0.9931}\text{-DMBDC}$ (black squares), and temperature dependence of integrated intensity of Tb^{3+} (545 nm) for Tb-DMBDC (red triangles). (Inset) Fitted curves of the integrated intensity ratio for $\text{Eu}_{0.0069}\text{Tb}_{0.9931}\text{-DMBDC}$ from 50 to 200 K. B. CIE chromaticity diagram showing the luminescence color of $\text{Eu}_{0.0069}\text{Tb}_{0.9931}\text{-DMBDC}$ at different temperatures.³³

The two-photon (TP) sensitization in lanthanide complexes provides opportunities to develop better bioimaging materials. This technique uses the lower-energy excitation in the near-infrared region (700-900 nm) to emit higher-energy photons with shorter wavelength in the visible region. Su and coworkers synthesized lanthanide homometallic and d-f heterometallic Eu(III) -based MOFs containing a functionalized tripodal ligand, triCB-NTB (4,4',4''-(2,2',2''-nitriлотris-(methylene)tris(1H-benzo[d]imidazole-2,1-diyl)tris(methylene))tribenzoic acid).³⁶ Due to the non-inversion symmetry imposed on the central Eu(III) and the large polarizability of the ligand, one-photon (OP) luminescence, based on the ET from ligand to Eu^{3+} and two-photon (TP) luminescence, based on the hypersensitive transition of the Eu^{3+} ions are observed in the MOFs. As shown in scheme 3, for OP luminescence, the ligand absorbs the UV light to S_1 state and then populates T_1 state through ISC. LMET forms the excited state of Eu^{3+} ($^5\text{D}_0$) and the OP luminescence is observed when the $^5\text{D}_0$ converts to $^7\text{F}_0$ ground state through radiative decay. While



Scheme 3. Mechanism of OP and TP emissions in the reported Eu(III)-based MOFs.³⁶

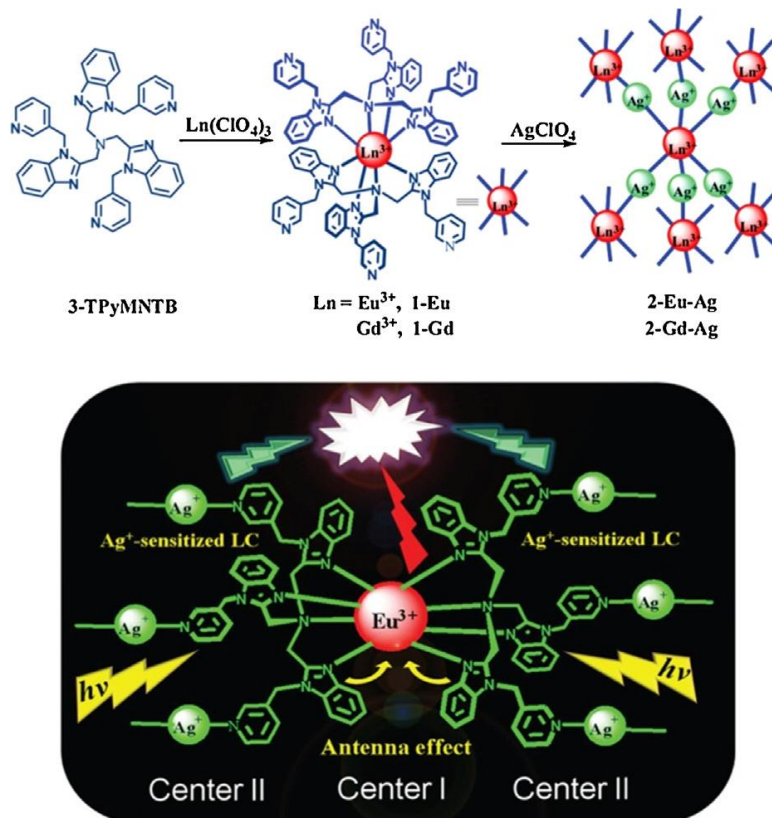


Figure 14. Stepwise assembly of MOFs 2-Ln-Ag (top) and representation of dual-emitting pathways in 2-Eu-Ag generating white-light emission (bottom).³⁷

for the TP process, the ground state 7F_0 of Eu^{3+} absorbs two photons and is excited to the hypersensitive transition state 5D_2 which is sensitized in reported two MOFs due to their spatial and electronic structures. Then, the energy is relaxed to the emitting 5D_0 state and finally returns to the ground state 7F_0 , characteristic red emission is observed. The parallel study from same group synthesized a single-phase Eu-Ag MOF that exhibits dual emission.³⁷ A bifunctional NTB (tris(benzimidazol-2-ylmethyl)amine)-type ligand, containing coordination discriminable tripodal benzimidazolyl and monodentate pyridyl groups, tris((pyridin-3-ylmethyl)benzimidazol-2-ylmethyl)amine (3-TPyMNTB), was used to assemble 4d–4f heterometallic three-dimensional MOFs in a stepwise method. In the Eu-based MOF, the ligand acts as an antenna to transfer absorbed energy to the Eu^{3+} center, resulting in characteristic red luminescence. Remarkably, in heterometallic MOF 2-Eu-Ag, the ligand-centered emission was resensitized by Ag^+ ions to generate dual emission, resulting in white-light emission from a single crystal (Figure 14). The heterometallic MOF material showed a new design strategy for the multicomponent white-light materials.

4.3.2 Ln@MOF

The luminescence intensities of lanthanide cations are often limited in aqueous media due to the low quantum yields. MOFs provide a rigid scaffold that can serve as the host for protecting the Ln cations from solvent quenching. Therefore, encapsulation of Ln within MOFs is an alternative strategy to probe the ET process for Ln-MOFs. Moreover, the trapped Ln cations in the porous framework could enhance the biocompatibility of lanthanide molecular complexes, which further extend their biomedical applications.

Luo *et al.* prepared microporous MOF $[\text{NH}_4]_2[\text{ZnL}]\cdot 6\text{H}_2\text{O}$ ($\text{L} = 1,2,4,5\text{-benzenetetra-carboxylate}$) with regular one dimensional channels, which were occupied by $[\text{NH}_4]^+$ counter

ions.³⁸ The lanthanide (III)-trapped MOF can be simply generated by using lanthanide ions replace counter ions in water. It is interesting that the original blue emission of the MOF can be easily tuned by doping the framework with Eu^{3+} or Tb^{3+} to produce red or green emission, respectively. Different transition-metal ions have a range of effects on the luminescence intensity, in particular, Cu^{2+} and Co^{2+} showed significant effects on the Eu^{3+} and Tb^{3+} doped MOF, respectively. This result indicated that the lanthanide-encapsulated MOF provides a highly selective and sensitive method for Cu^{2+} and Co^{2+} detection in aqueous solutions.

Rosi, Petoud and coworkers prepared a porous anionic MOF, bio-MOF-1 with the structure $[\text{Zn}_8(\text{ad})_4(\text{BPDC})_6\text{O}\cdot 2\text{Me}_2\text{NH}_2, 8\text{DMF}, 11\text{H}_2\text{O}]$ (ad = adeninate; BPDC = biphenyldicarboxylate; DMF = dimethylformamide), that acts as a scaffold for hosting and sensitizing several visible ($\text{Sm}^{3+}, \text{Tb}^{3+}, \text{Eu}^{3+}$) and near-infrared (NIR) emitting (Yb^{3+}) lanthanide cations.³⁹ The loading of lanthanide cations into the pore of bio-MOF-1 can be achieved by a simple cation exchange process and is confirmed by the luminescence properties of the resulting host-guest materials (Figure 15 A, B and C). The powder X-ray diffraction (PXRD) showed that Ln^{3+} loading did not impact the crystalline integrity of bio-MOF-1 (Figure 15 D). Excitation and emission spectra of $\text{Ln}@$ bio-MOF-1 revealed the energy migration from MOF chromophoric structure (BPDC based) to Ln^{3+} guest cation under irradiation at 340 nm (Figure 15 B). Although water is a highly quenching solvent for the emission of lanthanide ion, the bio-MOF-1 could serve as a “lantern” to protect the lanthanide cations and enhance their luminescence in water. Moreover, the preliminary O_2 detection experiments using $\text{Yb}^{3+}@$ bio-MOF-1 demonstrated that $\text{Ln}^{3+}@$ bio-MOF-1 materials can potentially be used as versatile high surface area sensors for small molecules, such as dioxygen.

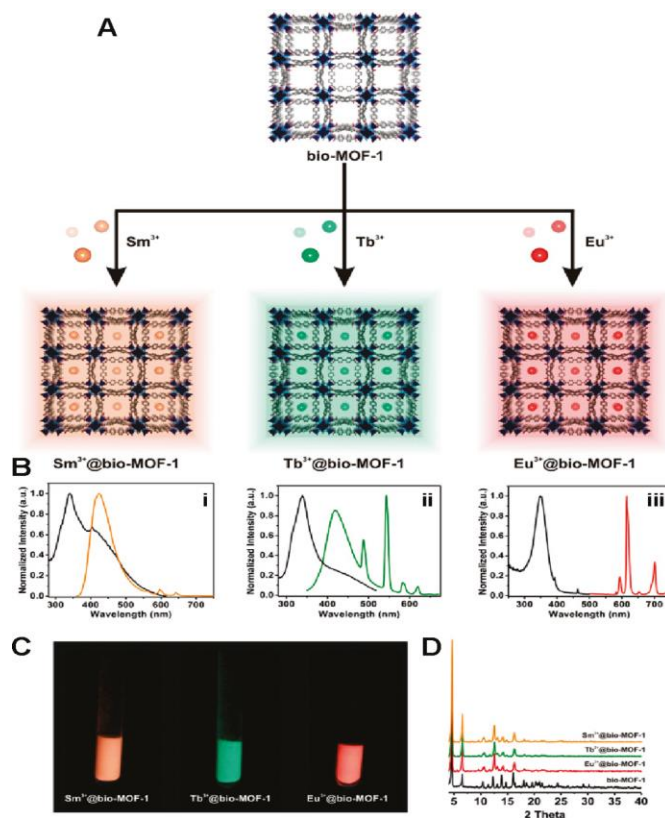


Figure 15. Bio-MOF-1 encapsulation and sensitization of lanthanide cations. (A) Schematic illustration of Ln³⁺ incorporation into bio-MOF-1 and subsequent Ln³⁺ sensitization by the framework. (B) Excitation and emission spectra of Sm³⁺ @bio-MOF-1 (i), Tb³⁺ @bio-MOF-1 (ii), and Eu³⁺ @bio-MOF-1 (iii). (C) Samples of Ln³⁺ @bio-MOF-1 illuminated with 365 nm laboratory UV light. (D) PXRD patterns of Ln³⁺ @bio-MOF-1.³⁹

Zang and coworkers reported a 3D MOF structure, $\{[Zn_2(L)\cdot H_2O]\cdot 3H_2O\cdot 3DMAc\cdot NH_2-(CH_3)_2\}_\infty$ (Zn(II)-MOF), which was prepared from H₅L (3,5-bis(1-methoxy-3,5-benzene dicarboxylic acid)benzoic acid), DMAc (*N,N'*-dimethylacetamide) and ZnCl₂ under solvothermal conditions.⁴⁰ The Zn(II)-MOF is anionic and contains 1D nanotubular channels with dimethylammonium cations. Post-synthetic exchange the dimethylammonium cations with Ln³⁺ ions can trap the Eu³⁺ and Tb³⁺ into the pores of MOF materials, which induced interesting luminescence properties. Again, variation of the dopant amounts of Eu³⁺ and Tb³⁺ could tune the emission bands of MOF materials, which resulted in white light emission. The best combination of Eu³⁺ and Tb³⁺ concentration in the Ln³⁺-exchanged materials for white light emission is

$\text{Eu}^{3+}_{0.127}/\text{Tb}^{3+}_{0.432}@\text{Zn(II)-MOF}$ (the quantum yield is $\eta = 7\%$) and $\text{Eu}^{3+}_{0.183}/\text{Tb}^{3+}_{0.408}@\text{Zn(II)-MOF}$ (the quantum yield is $\eta = 8\%$) with the corresponding CIE coordinates being (0.312, 0.335) and (0.339, 0.327), respectively; both are very close to the coordinates for ideal white-light (0.333, 0.333), according to the 1931 CIE coordinate diagram (Figure 16).

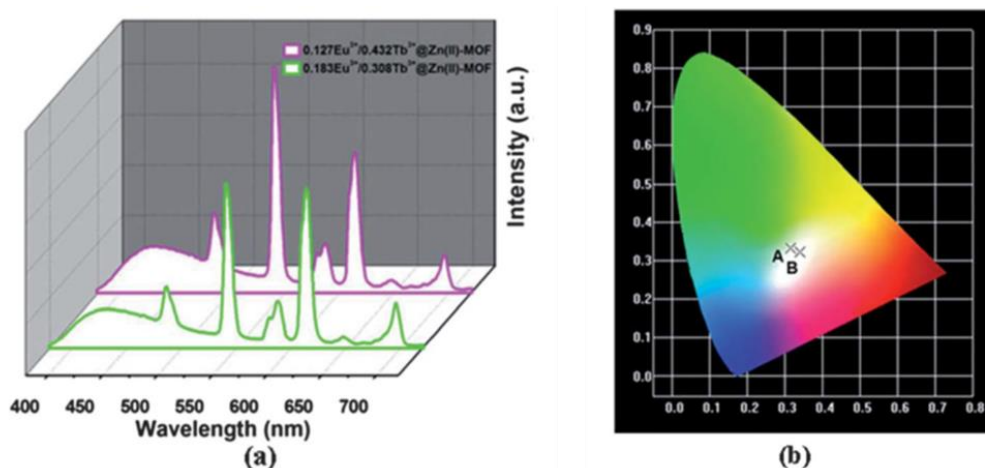


Figure 16. (a) Emission spectra of $0.127\text{Eu}^{3+}/0.432\text{Tb}^{3+}@\text{Zn(II)-MOF}$ and $0.183\text{Eu}^{3+}/0.408\text{Tb}^{3+}@\text{Zn(II)-MOF}$ excitation at 359 nm. (b) CIE chromaticity diagram for the $x\text{Eu}^{3+}/y\text{Tb}^{3+}@\text{Zn(II)-MOF}$ monitored under 359 nm ((A) $x = 0.127$, $y = 0.432$ and (B) $x = 0.183$, $y = 0.408$).⁴⁰

4.3.3 Summary

Lanthanide MOFs provide a versatile platform to exploit different ET processes to tune the resultant luminescent properties. Indeed, ET tuning has led the demonstration of Ln-MOF utility in sensing, luminescence thermometers, and solid-state lighting. Key findings are summarized below:

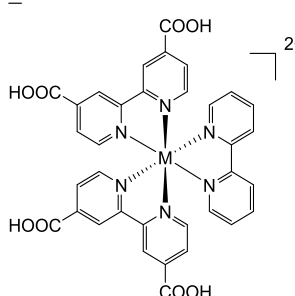
- LLET, LMET, and MMET have been demonstrated in Ln-MOFs.
- The well-known HAE is transferrable to MOF systems and can enhance the efficiency of LMET in MOF constructs.

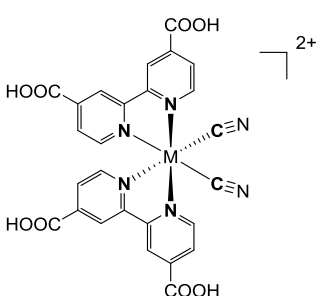
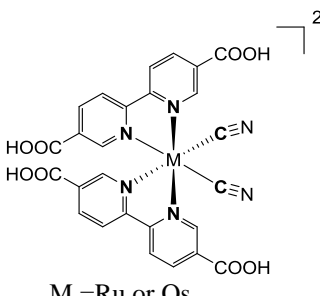
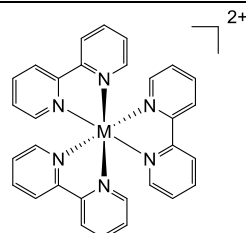
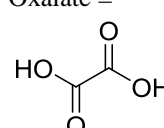
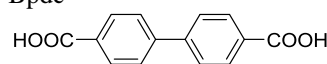
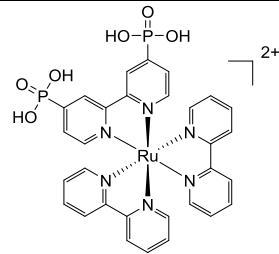
- Near ideal, white-light emission can be achieved through a combination of ligand based sensitization of Ln³⁺ ions (antenna effect/LMET and MMET).
- Encapsulation of Ln³⁺ ions can attenuate the effect of solvent-based luminescence quenching and opens Ln³⁺ materials to application in aqueous media.

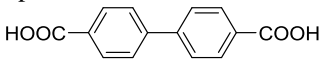
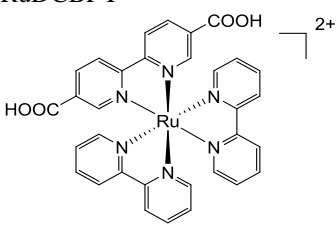
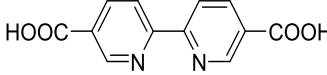
4.4 Ru/Os based MOF

Ru(bpy)₃²⁺ and Os(bpy)₃²⁺ (bpy = bipyridine) are ideal photoactive compounds to dope into a MOF matrix due to their relative long-lived excited states and redox activity. The photochemical and photophysical properties of Ru(bpy)₃²⁺ and Os(bpy)₃²⁺ have been well established in molecular systems. The well-defined crystal structure of the MOFs allows for precise control of interchromophore distances and angles via crystal engineering. Based on the utilization of different MOF matrices, current studies have focused on the incorporation/encapsulation of Ru/Os chromophores in Zn-node or Zr-node based MOFs. The reported MOFs containing Ru/Os chromophores are shown in Table 2.

Table 2. Summary of MOFs containing Ru/Os chromophores

MOF	Chemical Formula	Ligand Structure	Guest	Ref
MOF-1	[ZnL ₁] ₂ ·2DMF·4H ₂ O	L ₁ =  M=Ru or Os		[45]

MOF-2	$[\text{Zn}(\text{H}_2\text{L}_2)] \cdot 3\text{H}_2\text{O}$	$\text{L}_2 =$  $\text{M} = \text{Ru or Os}$		[46]
MOF-3	$[\text{Zn}_5(\text{L}_3)_2 \cdot (\mu\text{OH}) \cdot (\text{HCOO}) \cdot \text{DMF} \cdot 2\text{H}_2\text{O}] \cdot 6\text{H}_2\text{O}$	$\text{L}_3 =$  $\text{M} = \text{Ru or Os}$		[47]
MOF-4	$[\text{M}(\text{bpy})_3^{2+}][\text{Zn}_2(\text{C}_2\text{O}_4)_3]$	Oxalate =	 $\text{M} = \text{Ru or Os}$	[48]
MOF-5	$[\text{M}(\text{bpy})_3^{2+}][\text{NaAl}(\text{C}_2\text{O}_4)_3]$			
Ru@IRMOF-10	$\text{Ru}(\text{bpy})_2(\text{dpbpy})@\text{Zn}_4\text{O}(\text{bpdc})_3$	$\text{Bpdc} =$ 	 $\text{M} = \text{Ru or Os}$	[49]

RuDCBPY-UiO67	$Zr_6O_4(OH)_4(RuDCBPY)_x$ (BPDC) _{6-x}	Bpdc =  RuDCBPY = 		[53]
RuDCBPY-UiO-67-DCBPY	$Zr_6O_4(OH)_4(RuDCBPY)_x$ (DCBPY) _{6-x}	DCBPY = 		[54]

4.4.1 Ru/Os in Zn-node based MOFs

Energy flow from polypyridyl-based metal-to-ligand charge transfer (MLCT) excited states of Ru(II) to Os(II) has been studied in a variety of systems, such as ligand-bridged complexes, supramolecular assemblies,⁴¹ polymers⁴² and crystalline molecular solids,⁴³⁻⁴⁴ in order to elucidate the energy transfer dynamics. The Lin and Meyer groups first observed this classic Ru-to-Os energy transfer process in MOFs using the derivatives of Ru(bpy)₃²⁺/Os(bpy)₃²⁺ as the building units and Zn clusters as metal centers to construct a 2D bilayer structure.⁴⁵ As shown in Scheme 4, the phosphorescent MOF-1, based on Ru(II)(bpy)(4,4'-dcbpy)₂ (L_{1-Ru}), where 4,4'-dcbpy = 2,2'-bipyridine-4,4'-dicarboxylic acid) building blocks, has strong absorption in the visible region and can easily be excited to the long-lived triplet metal-to-ligand charge transfer (³MLCT) states. Upon doping the Os(II) (bpy)(4,4'-dcbpy)₂ (L_{1-Os}) into the framework structure, the mixed-metal MOF-1 was obtained with 0.3, 0.6, 1.4 and 2.6 mol % Os loading. Time-resolved emission studies were performed with a two-photon excitation at 850 nm and energy migration from photoexcited Ru to Os trap sites was observed (Figure 17a). The lifetimes of Ru(II) excited states decreased progressively with the increasing doping of Os from 0.3 to 2.6 mol % (Figure 17b). The sensitization of Os loading was proposed to occur via a Ru-to-Ru energy hopping followed by Ru-

to-Os energy cascade due to the lower energy state of Os acting as a trap site (Figure 17c). Analysis of the crystal structure indicated that the quenching radius of an Os trap site is around ~ 40 Å, based on the assumption of 3D migration pathways.

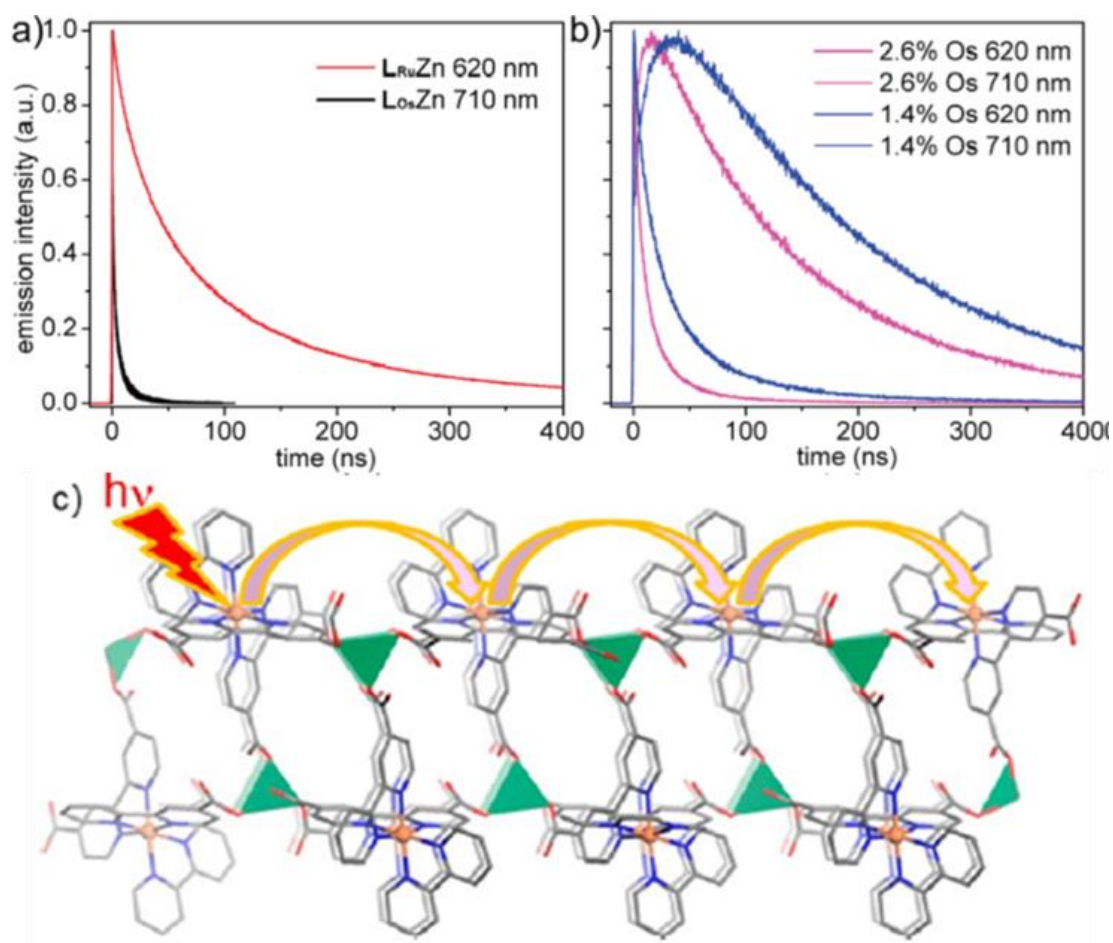
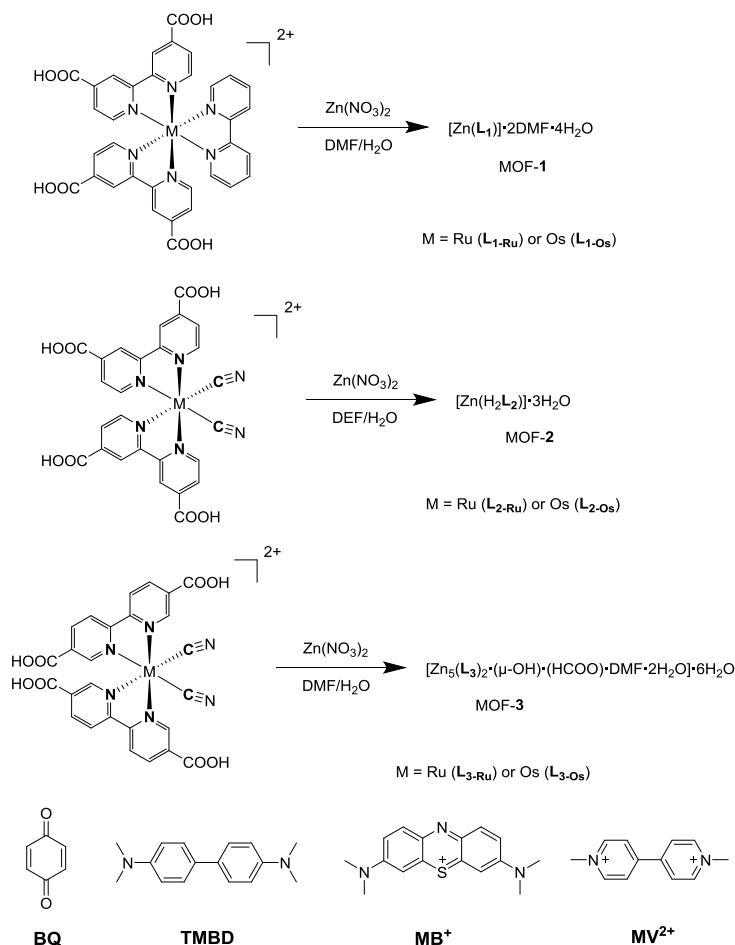


Figure 17. (a) Transient emission decay profiles for L_{Ru} and L_{Os} MOF-1 monitored at 620 and 710 nm respectively following two-photon excitation at 850 nm. (b) Transients for 1.4 and 2.6 mol % Os-doped MOF-1 at 620 and 710 nm with emission at 620 nm dominated by $Ru(II)^*$ and at 710 nm by $Os(II)^*$. (c) Schematic depicting the hopping of the $Ru(II)^*$ -bpy excited states in MOF-1.⁴⁵

Following the energy migration studies, Lin, Meyer and co-workers used redox luminescence quenching to probe the charge separation ability of MOF-1 and MOF-2, which are built from a similar ruthenium-based bridging ligand ($L_{2-Ru} = Ru(4,4'-dcbpy)_2(CN)_2$).⁴⁶ The quenching

experiments were performed with stirred suspension of the MOF microcrystals in degassed acetonitrile in the presence of an oxidative quencher (1,4-benzoquinone, BQ) or a reductive



Scheme 4. Synthesis of phosphorescent MOF-1, MOF-2 and MOF-3 and chemical structure of various redox quenchers.

quencher (N,N,N',N'-tetramethylbenzidine, TMBD). Both MOFs showed that the extent of Ru(II)* emission quenching increases as the quencher concentration is increased. Up to 98% quenching was achieved for MOF-2, with either BQ or TMBD, as a result of rapid energy migration over several hundred nanometers followed by efficient electron transfer quenching (Figure 18). The quenching process was proposed to take place at the MOF/solution interface as the MOF channels are too small to allow the diffusion of quencher molecules. Another study from the same groups

demonstrated an amplified luminescence quenching for MOF-2 with methylene blue (MB^+) as quencher.⁴⁷ Strong non-covalent interactions between the MOF surface and cationic quencher molecules coupled with rapid energy transfer through the MOF microcrystal lead to a 7000-fold enhancement of Stern-Völmer quenching constant compared with the ligand ($\text{L}_2\text{-Ru}$) in solution. It is important to mention that the rate of energy transfer through MOF plays a very important role in changing the quenching efficiency. MOF-3 was synthesized with $\text{L}_3\text{-Ru}$ by changing the $\text{Ru}(4,4'\text{-dcbpy})_2(\text{CN})_2$ in MOF-2 to $\text{Ru}(5,5'\text{-dcbpy})_2(\text{CN})_2$, resulting in a three-dimensional framework. Although similar ionic interaction between the quencher and MOF surface would be expected, emission quenching efficiency saturates at 80% with methyl viologen (MV^{2+}) for MOF-3, mainly due to the competition between excited-state decay process with energy transfer via hopping mechanism. However, for MOF-2, the intra-MOF ET is more rapid than MOF-3, so that the complete emission quenching was achieved with MV^{2+} . These results highlight the effect of 3D structure on ET efficiency. The chromophores in MOF-2 and MOF-3 differ only in the position of the carboxylic acid units. Although, the ET efficiency is drastically different, which may be in part due to the change in angles between interacting chromophores.

Due to their porosity and aperture size tunability, photoactive Ru/Os polypyridyl complexes can also be encapsulated into the MOFs as guest molecules to probe energy transfer. The Lin and Meyer groups synthesized two non-porous MOFs with caged $\text{Ru}(\text{bpy})_3^{2+}/\text{Os}(\text{bpy})_3^{2+}$ chromophores, $[\text{M}(\text{bpy})_3^{2+}]@[\text{Zn}_2(\text{C}_2\text{O}_4)_3]$ (MOF-4) and $[\text{M}(\text{bpy})_3^{2+}]@[\text{NaAl}(\text{C}_2\text{O}_4)_3]$ (MOF-5).⁴⁸ Long-lived $^3\text{MLCT}$ excited states with lifetimes of 760 and 1305 ns were observed in Ru-MOF-4 and Ru-MOF-5, respectively, under anaerobic conditions. With the presence of trace amount oxygen, the lifetimes were significantly shortened to 92 ns for MOF-4 and 144 ns for MOF-5, due to energy transfer from $\text{Ru}(\text{II})^*$ to O_2 . Similar to MOF-1 and MOF-2, $\text{Os}(\text{bpy})_3^{2+}$

could act as energy trap sites at doping level of 0.2-1.0%. Kinetic studies showed that the entrapped chromophores in three-dimensional frameworks MOF-4 and MOF-5 provides a network for rapid excited state energy transfer migration among $\text{Ru}(\text{bpy})_3^{2+}$ units, ultimately, finding an $\text{Os}(\text{bpy})_3^{2+}$ trap site.

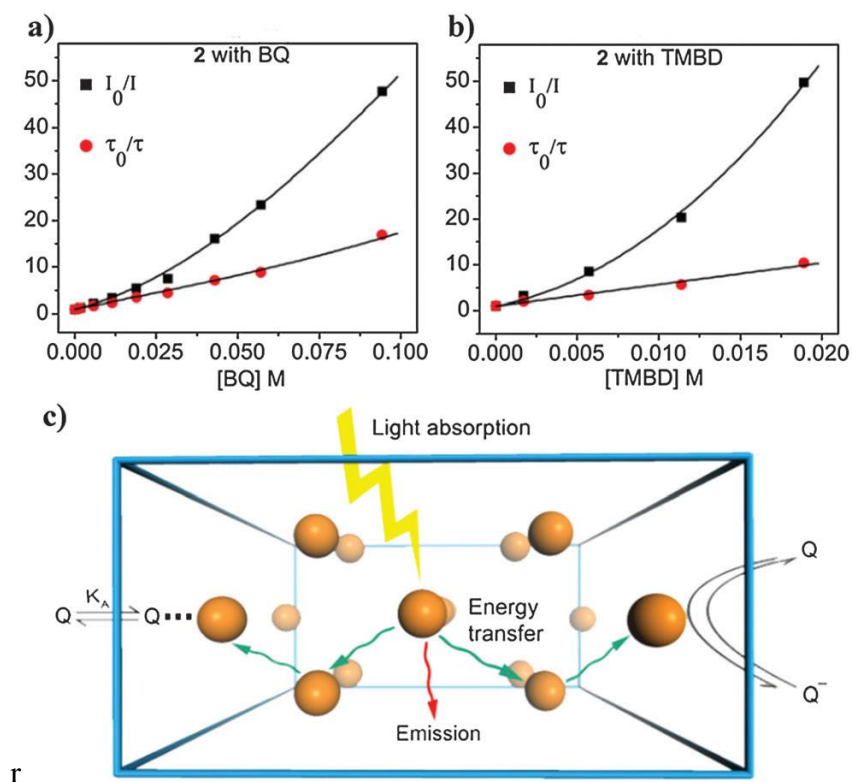


Figure 18. (a,b) Steady-state (black) and time-resolved (red) Stern–Volmer quenching analysis of MOF-2 with BQ (a) or TMBD (b). (c) Schematic showing the light-harvesting process in MOF microcrystals as a result of a rapid energy migration over several hundred nanometers followed by efficient electron transfer quenching at the MOF/solution interface.⁴⁶

Theoretical analysis was performed on ET in MOF-1 and MOF-4 to show how the MOF structure influences the pathways for exciton flow.⁸ The analysis showed that the exciton states are localized on single $\text{Ru}(\text{bpy})_3^{2+}$ or $\text{Os}(\text{bpy})_3^{2+}$ sites and the ET is dominated by a Dexter

mechanism. Both MOFs indicated ~ 10 ns exciton hopping times between adjacent Ru-polypyridyl sites separated by 8-10 Å. The excitons can make 3-6 hopping steps (~ 30-60 Å distances) within their lifetimes, depending on the dimensionality of the hopping network. The computed Dexter couplings in the MOFs showed that the exciton transport takes place in a 1D network in MOF-1, while ET in MOF-4 occurs through a 3D network. The kinetic analysis allowed direct comparison of ET efficiency between the two MOFs and indicated that the higher dimensionality coupling pathways weakly enhance the quenching efficiencies. In summary, the dominance of the weak Dexter coupling interactions leads to ET that is highly sensitive to metal-metal distance and to the existence of localized excitons and of hopping transport. One possible approach to improve the speed of ET in the Dexter coupling mechanism is to enhance Dexter coupling interactions by constructing MOFs with shorter intermetallic distances or more highly conjugated bridging units.

Yan and coworkers reported the encapsulation of Ru(bpy)₂(dpbpy) (dpbpy = 4,4'-diphosphonate-2,2'-bipyridine) into the biphenyl-based MOF (referred to as Ru@IRMOF-10).⁴⁹ The designed material exhibited well-defined blue/red luminescence at the crystal interior and exterior as detected by 3D confocal fluorescence microscopy. By controlling the amount and location of the Ru chromophores, the intensity ratio of blue to red emission can be varied at different regions within the MOF crystal. Specifically, at a low loading percentage of Ru@MOF (2.25%), the crystal interior exhibited blue luminescence, which was assigned to IRMOF-10 emission, while the surface of crystal exhibited emission at 600 nm, which can be attributed to the luminescence of the Ru chromophore. Those observations indicated the non-uniform distribution of Ru complex within the nanochannel, which is consistent with the gradual diffusion process of the Ru(bpy)₂(dpbpy) molecules into the MOF matrix. Moreover, the decrease in the intensity ratio of blue to red emission in the selected region close to the MOF surface suggests the occurrence of

energy transfer between the MOF host and Ru chromophore guest. A higher population of Ru(bpy)₂(dpbpy) molecules close to crystal exterior leads to more efficient energy transfer from

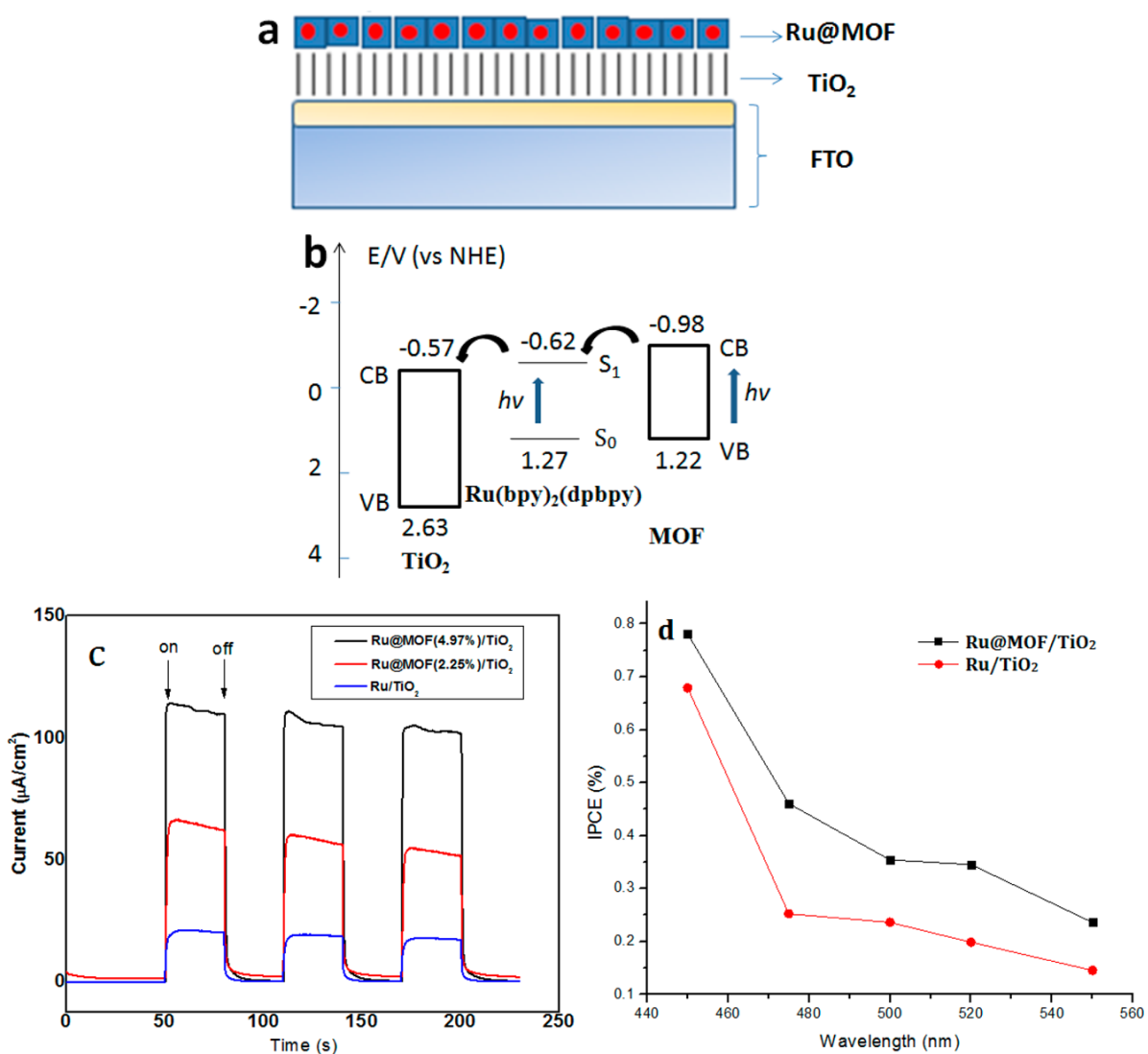


Figure 19. (a) Schematic structure of Ru@MOF/TiO₂ as photoelectrode on a FTO (Fluorine-doped Tin oxide) support. (b) Energy level positions of Ru complex, MOF, and TiO₂ relative to the NHE. (c) Photocurrent–time measurements with a chopped light from a Xe lamp light source (100 mW/cm²) and at an external bias (0 V vs Ag/AgCl) for Ru@MOF (2.25%)/TiO₂, Ru@MOF (4.97%)/TiO₂, and Ru/TiO₂ (0.1 M phosphate buffer, pH 7). (d) Dependence of IPCE values on incident wavelength for Ru@MOF (4.97%)/TiO₂ and Ru/TiO₂.⁴⁹

the MOF matrix to Ru chromophore compared with that in the center of MOF. The energy transfer processes from host to guest molecule and the intramolecular MLCT process were further

confirmed by DFT calculations, which were consistent with the experimental results. Upon attaching on the rutile TiO₂ nanoarray, the Ru@MOF system showed enhanced incident photon-to-current conversion efficiency (IPCE) relative to the pristine Ru-based complex directly anchored to the semiconductor surface (Figure 19). Therefore, by the appropriate choice of MOF and photoactive complex with suitable energy levels and luminescence, the host-guest photofunctional materials have potential applications in luminescent and optoelectronic materials.

4.4.2 Ru(bpy)₃²⁺ doped zirconium(IV) MOFs

UiO-67 is a water-stable framework containing Zr₆(μ₃-O)₄(μ₃-OH)₄ nodes connected by twelve 4,4'-biphenyldicarboxylate (BPDC) linkers (Figure 20A).⁵⁰ The structure contains pores with two distinct geometric environments: an octahedral pore of 23 Å diameter and a tetrahedral pore of 11.5 Å diameter (Figure 20B).⁵¹ UiO-67 provides a unique platform for incorporation of organometallic photosensitizers, such as [Ru(dcbpy)(bpy)₂]²⁺ (RuDCBPY), by the simple replacement of one the bipyridine ligands with 2,2'-bipyridyl-5,5'-dicarboxylic acid (DCBPY).⁵² (Figure 20B) Lin and co-workers were the first to report this mix-and-match synthetic strategy to dope different transitional-metal molecular catalysts, including RuDCBPY, into the UiO-67 framework.⁵² The dependence of the photophysical behavior on Ru(bpy)₃²⁺ loading was later probed by the Morris group.⁵³⁻⁵⁴ The changes in excited-state lifetimes and spectral differences observed with increasing dye concentration were attributed to dipole-dipole homogeneous resonance energy transfer (RET) and loading-dependent differences in incorporation/encapsulation environments (*vide infra*).⁵³⁻⁵⁴

The photophysical properties of RuDCBPY-UiO-67 were first probed as a function of the doping concentrations. The steady-state diffuse reflectance of the RuDCBPY-UiO-67 powder showed an absorption maximum at 455 nm, which was attributed to a singlet metal-to-ligand

charge transfer ($^1\text{MLCT}$) characteristic of $\text{Ru}(\text{bpy})_3^{2+}$ and its derivatives.^{53,55} This absorption band broadened with increased loading percentage, while the absorption maximum remained constant

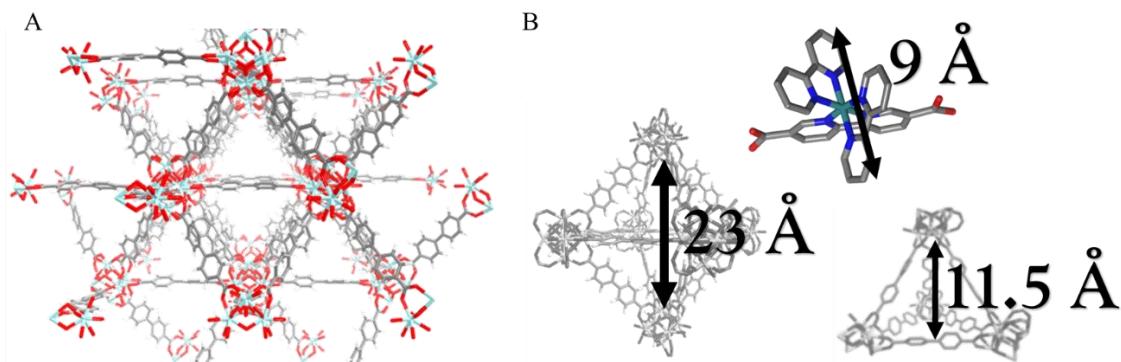


Figure 20. A) Crystal structure of UiO-67, $\text{Zr}_6(\mu_3\text{-O})_4(\mu_3\text{-OH})_4(\text{BPDC})_{12}$, where BPDC = biphenyldicarboxylic acid: black, carbon; red, oxygen; cyan, zirconium. B) Octahedral cavity (left), the tetrahedral cavity (right), RuDCBPY (middle).⁵³

at all doping concentrations. However, the energy of the emission maxima and excited-state lifetimes were found to be quite sensitive to the concentration of RuDCBPY incorporated into UiO-67. At low doping concentrations ($\leq 16.4 \text{ mm}$), the excited-state properties of RuDCBPY in the MOF deviate markedly from those in aqueous solution, but resemble those in DMF. Specifically, the emission maximum centered around 630 nm, was slightly bathochromically shifted relative to RuDCBPY in DMF (625 nm).⁵³ The emission decay can be adequately modeled using a single discrete exponential decay function with an observed lifetime of 1.4 μs , which is longer than that of RuDCBPY in DMF (890 ns). This increased lifetime is due to the fact that vibrational decay pathways are hindered when the chromophore is incorporated into a rigid matrix. Interestingly, at higher doping concentrations ($> 16.4 \text{ mm}$), the emission spectra demonstrated a bathochromic shift relative to the low doping materials, displaying an emission maximum around 650 nm. The observed emission decays at high loadings were biphasic with a concentration-dependent long lifetime component ($\tau \sim 165\text{-}210 \text{ ns}$) and a concentration

independent short lifetime component (~ 24 ns) resembling the lifetime of RuDCBPY in water (~ 38 ns).

A two-state model was proposed to explain the biphasic nature of the decay at high doping concentration (Figure 21). At low doping concentrations, RuDCBPY was said to preferentially occupy the larger octahedral cages of UiO-67 by incorporation into the backbone of the cage. As a result of residual solvothermal reaction solvent (i.e. DMF) in the pore, this population experiences a dimethylformamide (DMF)-like solvation environment. However, at higher doping concentrations, in addition to the RuDCBPY *incorporated* into the backbone of UiO-67, populations of RuDCBPY were found to be *encapsulated* in separate octahedral cavities of the MOF (Figure 21). Encapsulation is assumed to restrict the solvent (DMF) occupancy within the pore and the μ -O and μ -OH bridges of the Zr-nodes were thought to impose a polar water-like dielectric on RuDCBPY so that the solvation environment resembles that of bulk water. The result was emission spectra and lifetimes dominated by water-like photophysical properties. RuDCBPY has shorter emission lifetime (~ 38 ns) in water than in DMF, mainly due to the sensitivity to solvent (particularly solution pH) arising from preferred localization of the $^3\text{MLCT}$ on the DCBPY ligand.

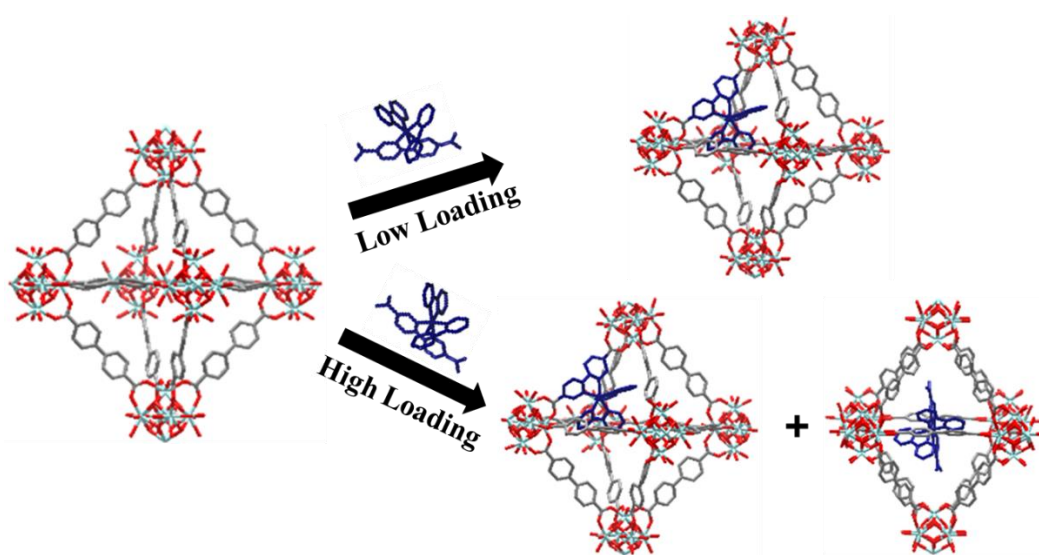


Figure 21. Two-state model of concentration dependent RuDCBPY doping behavior⁵³

The concentration dependence of the long lifetime component observed for RuDCBPY-UiO-67 was attributed to RET between RuDCBPY ³MLCT states. The emission lifetime data for RuDCBPY-UiO-67 at the doping concentration between 3 mm and 21 mm was fit to the Inokuti-Hirayama function, which lead to $1/r^4$ distance dependence for the energy transfer rate. This suggests a dipole-dipole RET process lying on a continuum between the Perrin weak coupling and Förster very weak coupling regimes, which has been proposed by Kenkre and Knox.⁵⁶ This indicates that the framework imparts a stronger dipole coupling between the incorporated RuDCBPY chromophores. The RuDCBPY incorporated in the MOF are locked into a specific geometry dictated by the crystal structure of the UiO framework. Such preferential orientation of chromophores enables dipole alignment, stronger dipole-dipole coupling, and longer range energy transfer.

RuDCBPY-UiO-67-DCBPY was prepared by a post-synthetic approach in order to incorporate the transition metal complex directly into the backbone of UiO-67 MOF *in situ*.⁵⁴ The emission decay of RuDCBPY-UiO-67-DCBPY can be fit in a more general model, suggested by Klafter and Blumen, which indicates concentration-dependent dimensionality of RET. Confocal fluorescence microscopy was used to study the bulk distribution of RuDCBPY centers within MOF crystallites as fractal-like so that the rate of energy transfer would depend on the fractal dimension \bar{d} . Detailed fitting showed at low loading of RuDCBPY (< 10 mm) RET was one-dimensional, at concentrations between ~10 and ~50 mm the RET was two-dimensional, and at a concentration above which a percolation limit was met, the RET was three-dimensional. (Figure 22)

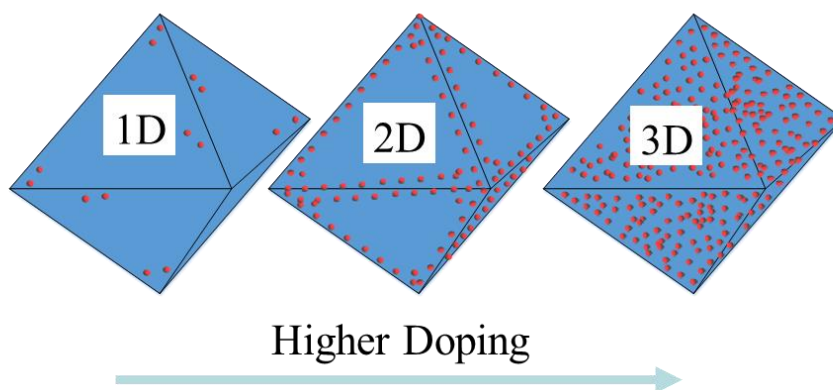


Figure 22. The assumption of FRET mechanism on dependence of RuDCBPY loading.⁵⁴

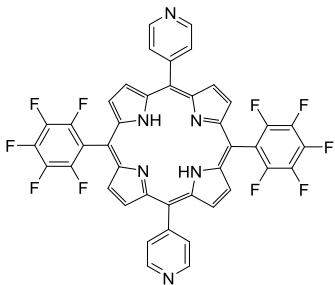
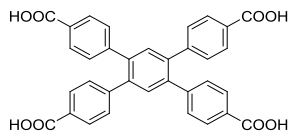
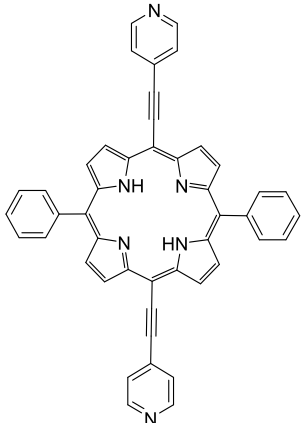
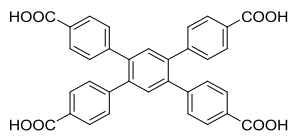
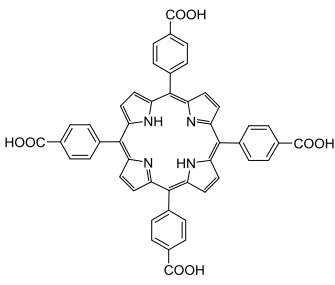
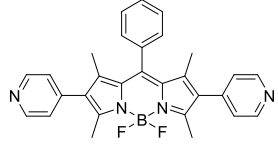
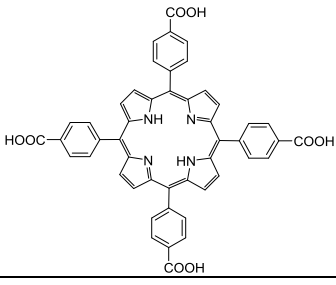
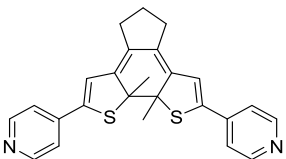
4.4.3 Summary

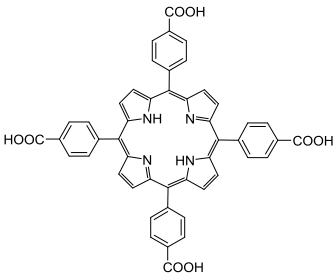
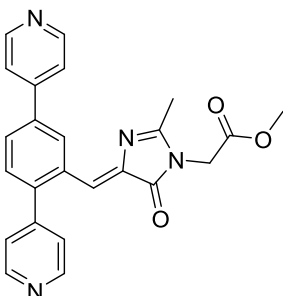
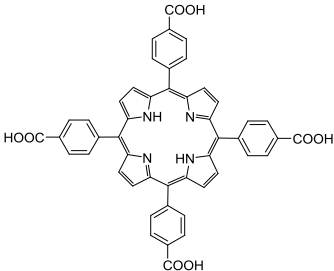
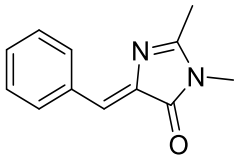
The excited state behavior of Ru/Os polypyridyl photosensitizers immobilized in MOF crystalline networks is unique and requires further study. Ru/Os based MOFs provide a special model to probe and explore ET in solid states. Understanding the ET process and mechanism in these MOFs would lead to the design of MOFs as functional materials in the fields of light harvesting, photocatalysis and photovoltaic devices. More importantly, figuring out the limitation of ET in these MOFs would lead to the intelligent design of a better generation in the near future.

4.5 Porphyrin and metalloporphyrins based MOFs materials

Porphyrins and their derivatives are a class of well-known molecular chromophores that typically have strong light absorption in the visible region. Porphyrin-containing struts are the primary building units used in MOFs that target solar light harvesting.⁹ Table 3 summarizes the porphyrin-based MOFs that have been reported in the literature.

Table 3. Summary of MOFs containing porphyrin-based ligands

MOF	Chemical Formula	Porphyrin based Ligand Structure	Co-ligand	Ref
F-MOF		<p>F-H₂P =</p> 		[57]
DA-MOF		<p>DA-H₂P</p> 		[57]
BOP MOF	$C_{77}H_{49}BF_2N_8O_9Zn$ 3	<p>TCPP =</p> 		[58]
$[Zn_2(ZnTCPP)(BPMT)_{0.85}(DEF)_{1.15}]$		<p>TCPP =</p> 	<p>BPMT =</p> 	[59]

DBP-PI-1	$[\text{Zn}_2(\text{ZnTCPP})(\text{DPBBI})_{0.86}(\text{DMF})_{1.14}] \cdot (\text{DMF})_{8.86}(\text{H}_2\text{O})_{20}$	TCPP = 	DPB-BI = 	[60]
DBP-PI-1'	$[\text{Zn}_2(\text{ZnTCPP})(\text{DPBBI})_{0.64}(\text{DEF})_{0.36}] \cdot (\text{DEF})_{6.94}(\text{H}_2\text{O})_{12.55}$	TCPP = 	BI = 	[60]

4.5.1 Porphyrin-based MOFs as crystalline powder

In natural photosynthesis, energy (exciton) migration primarily occurs in highly ordered porphyrin-like pigments (chlorophylls). Hupp, Wiederrecht, Farha and their co-workers designed two Zn-porphyrin based MOFs (DA-MOF and F-MOF) to mimic the light-harvesting behavior of natural photosynthetic systems (Figure 23).⁵⁷ Photogenerated exciton migration was investigated based on fluorescence quenching experiments and theoretical calculations. In F-MOF, a photogenerated exciton only migrates over a net distance up to ~3 porphyrin struts (8 hops) within its lifetime. Remarkably, the exciton migrates up to ~45 porphyrin struts (2025 hops) in DA-MOF with a high anisotropy along a specific direction. This implied that the molecular structure of the porphyrins plays a significant role in exciton hopping. As shown in Figure 24, the addition of two acetylene moieties in the porphyrin molecule enhances the π -conjugation in DA-H₂P ligand, which leads to higher absorption and a red-shifted Q-band, better absorption/emission overlap, greater dipolar coupling and much faster exciton hopping compare with F-ZnP. Under the excitation at 446nm, DA-MOF would generate a singlet exciton that can migrate by site-to-site hopping within

the MOF until it decays or is quenched by electron transfer to the excited linker from an axially ligand donor molecule (such as pyridyl-ferrocene, FcPy). If the quencher is present at only low concentration, rapid exciton migration results in amplified fluorescence quenching. The efficacy of exciton migration relative to the nonreactive exciton decay can be determined by measuring the extent of quenching with different levels of FcPy incorporation (Figure 25). DA-MOF provided the first example of long distance and directional energy migration in MOF materials and afforded useful guidelines for the development of efficient ligand-harvesting and energy-transport materials.

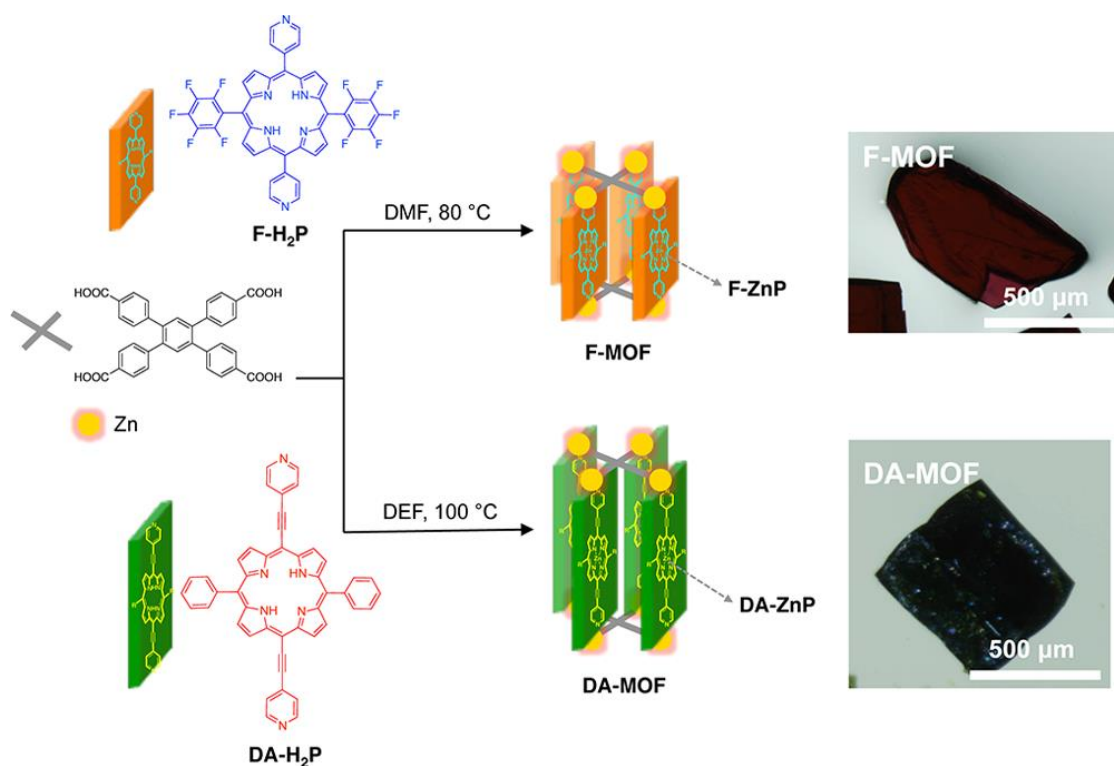


Figure 23. Synthesis routes of the isostructural DA-MOF and F-MOF compounds.⁵⁷

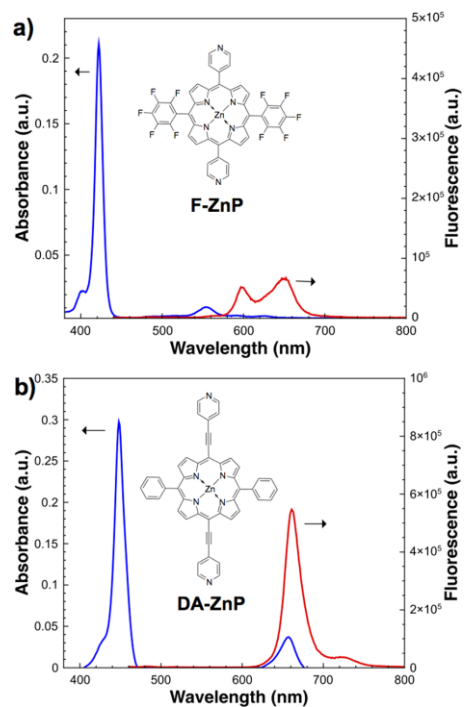


Figure 24. UV-vis absorption (blue) and emission (red) spectra of F-ZnP (a) and DA-ZnP (b) molecules in DMF. Their chemical structures are shown in the inset.⁵⁷

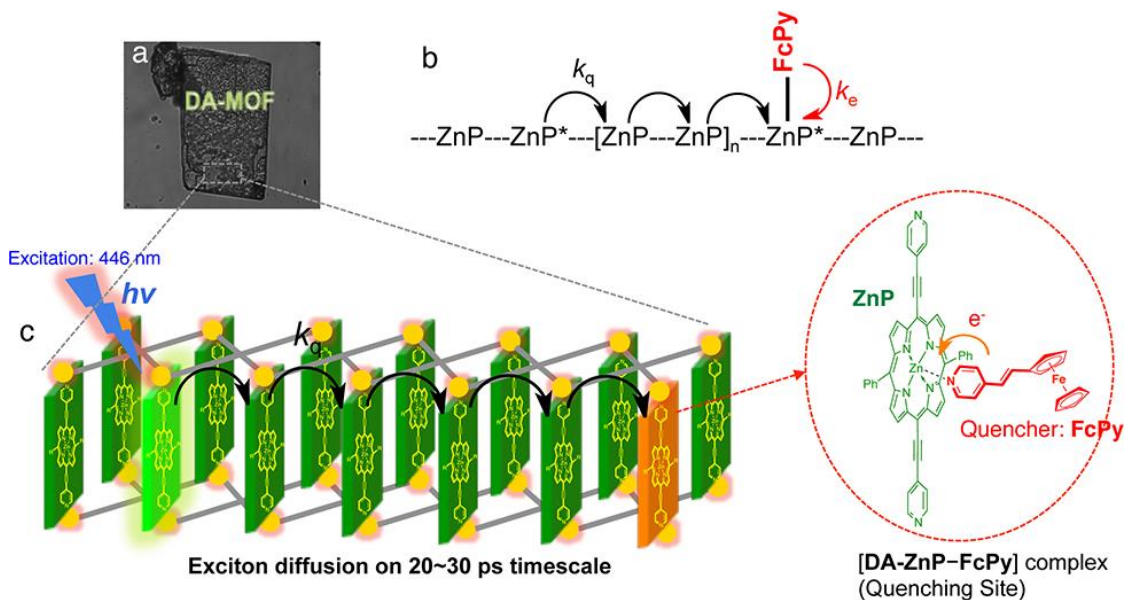


Figure 25. (a) Photograph of a DA-MOF particle from which fluorescence is recorded based on laser excitation at 446 nm. Luminescence quenching measurements are conducted to probe the energy (exciton) migration dynamics. (b,c) Schematic representation of the exciton migration and quenching processes.⁵⁷

Hupp and co-workers incorporated boron dipyrromethene (bodipy) and porphyrin complexes as complementary pairs of chromophores in pillared-paddlewheel type MOFs.⁵⁸ As shown in Figure 26, BOB MOF was prepared via solvothermal methods in DMF using $\text{Zn}(\text{NO}_3)_2 \cdot 6\text{H}_2\text{O}$, 1,4-dibromo-2,3,5,6-tetrakis(4-carboxyphenyl)benzene and dipyridyl boron dipyrromethene in the presence of HNO_3 . BOP MOF was synthesized using a two-step method, which relies on delaying the addition of the dipyridyl strut until after the tetraacid porphyrin has begun to assemble the zinc ions. The bodipy linkers absorb and emit in the green spectral region and serve as antenna chromophores for the excitation of porphyrinic struts via RET. By incorporation of the porphyrin units, the absorption of the bodipy-porphyrin-based (BOP) MOF crystals is extended even further into the visible range, so that the MOF crystals appear nearly black compared to just the bodipy-only MOF material. As shown in Figure 27, excitation of bodipy in BOB MOF at 543 nm results in typical bodipy fluorescence behavior with the emission maxima at 596 nm. However, excitation of same strut in BOP MOF at 543 nm is emissive in the 650-710 nm range, and indicates that sufficient energy is transferred from the bodipy strut to the Zn-porphyrin within BOP MOF.

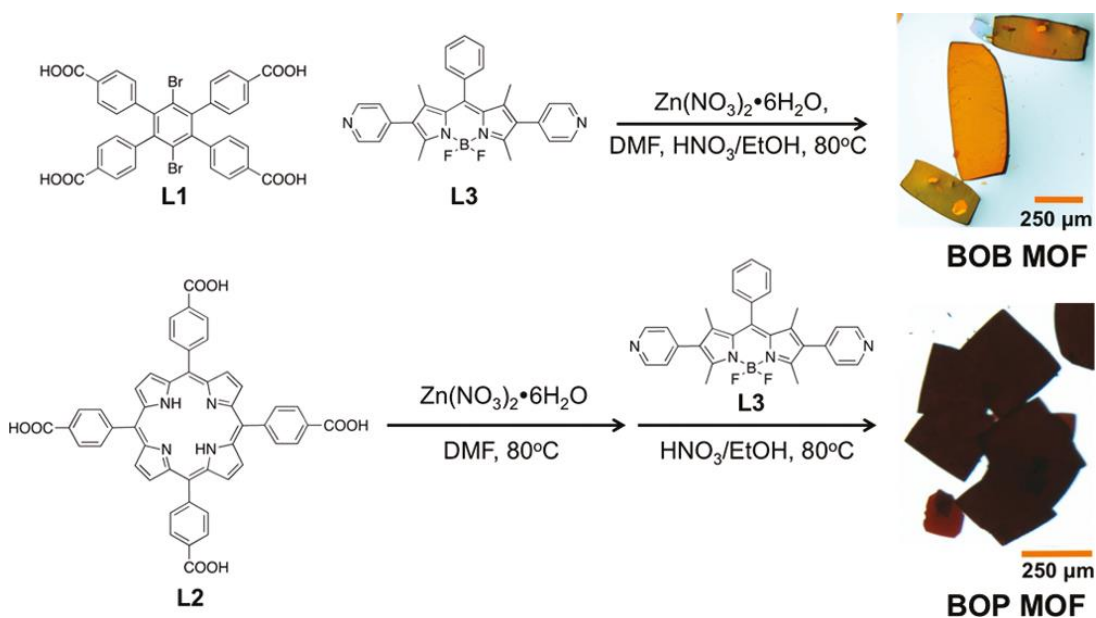


Figure 26. Synthesis of the Isostructural BOB MOF and BOP MOF.⁵⁸

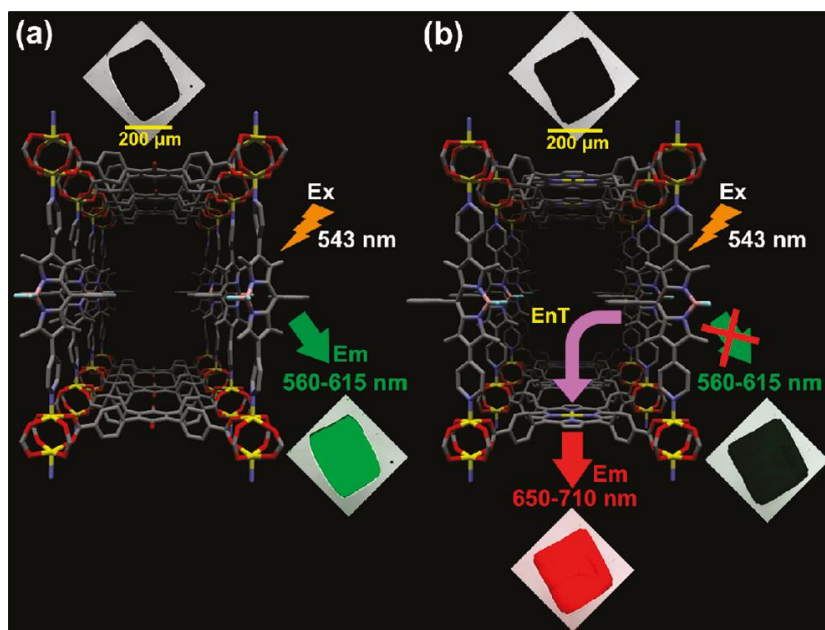


Figure 27. Confocal laser scanning microscopy (CLSM) images of crystals of: (a) BOB MOF and (b) BOP MOF.⁵⁸

After mimicking the light harvesting in the natural photosystem using highly ordered porphyrin as chromophore in MOFs, the next challenge is how to direct excitation-energy funneling along a predesigned pathway. One attractive strategy is to coordinatively immobilize a photochromic compound as pillars inside porphyrin-based MOF, which allows control of framework emission as a function of excitation wavelength. In that case, the photochromic diarylethene-based ligand acts as photo-switching because of its two discrete states upon photoirradiation.⁵⁹ Shustova and coworkers reported a 3D framework, $[\text{Zn}_2(\text{ZnTCPP})(\text{BPMT})_{0.85}(\text{DEF})_{1.15}]$, composed of bis(5-pyridyl-2-methyl-3-thienyl)-cyclopentene (BPMT) and tetrakis(4-carboxyphenyl)-porphyrin (H_4TCPP) ligands. The photochromic diarylethene-based derivative BPMT maintained its photoswitchable behavior and can direct the excited-state decay pathway of the host after coordinative immobilization in a MOF matrix. Specifically, the porphyrin-based linker acts as the donor and transfers excitation energy to the acceptor BPMT (Figure 28). Photoisomerization of BPMT resulted in the tunability of the MOF emission as a function of excitation wavelength. As shown in Figure 28b, irradiation of the MOF at 365 nm led to the closed form of BPMT, which

quenches the photoluminescence of the MOF through FRET with an estimated R_0 (Föster radius) of around 30 Å. When irradiated at 590 nm, BPMTTC isomerization to the open form successfully eliminates the ET pathway and the PL response of the porphyrin was observed.

Harkening back to the bioinspired nature of porphyrin light harvesters, the Shustova group extended their mixed ligand MOF studies to explore a MOF mimic of a highly efficient ET process observed between green fluorescent protein and a heme-binding cytochrome. Two approaches to study ET in a MOF mimic were explored including (1) direct incorporation of the donor and acceptor species as the linkers in a 3D framework and (2) the encapsulation of the donor in the pores of the MOF, termed BI@2 (Figure 29). Two unique MOFs with the donor (BI, 4-hydroxybenzylideneimidazolinone) and acceptor (tetracarboxyphenylporphyrin) incorporated into the backbone were achieved upon changing the solvothermal reaction conditions, $[\text{Zn}_2(\text{ZnTCPP})(\text{DPB-BI})_{0.86} (\text{DMF})_{1.14}] \cdot (\text{DMF})_{8.86}(\text{H}_2\text{O})_{20}$ (**1**) and $[\text{Zn}_2(\text{ZnTCPP})(\text{DPB-BI})_{0.64}(\text{DEF})_{0.36}] \cdot (\text{DEF})_{6.94} \cdot (\text{H}_2\text{O})_{12.55}$ (**1'**).⁵⁹ All three materials (**1**), (**1'**), and BI@2 showed efficient ET indicated by the complete disappearance of donor emission. Combining the time-resolved PL studies with spectral overlap function calculations, quantitative values of ET efficiency Φ_{ET} , ET rate constant, k_{ET} , and the Förster radius were determined and summarized in Table 4. Although, the efficiency of ET did not match that of the protein pair, the Φ_{ET} BI@2 was 72%. There were slight differences between the photophysical behaviors of (**1**) and (**1'**), which was attributed to the differences in interlayer stacking observed via single-crystal X-ray diffraction.

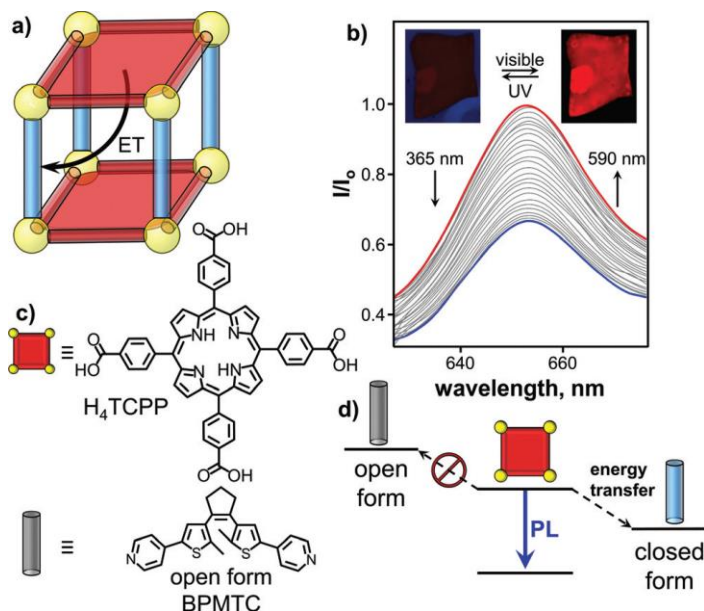


Figure 28. a) Förster ET between porphyrin-based ligand and photochromic BPMTC inside the MOF matrix. b) Emission spectra recorded for the porphyrin photoswitch MOF, scaled to give intensity (I_0) of 1.0 on the first scan at $\lambda_{ex}=590$ nm. The inset shows the epifluorescence microscopy images of the photoswitchable MOF crystal. c) Porphyrin-based donor and BPMTC acceptor (the latter is shown in the open form). d) A simplified diagram demonstrating the transitions responsible for fluorescence and FRET.⁵⁹

Table 4. The amplitude-weighted average lifetimes (τ_{av}), ET rate constants (k_{ET}), Förster critical radii (R_0), ET efficiency (FET), and spectral overlap functions (J) for DPB-BI, DPB-BI-1, DPB-BI-1', BI, and BI@2 samples.⁶⁰

	DPB-BI	DPB-BI-1	DPB-BI-1'	BI	BI@2
$\langle \tau_{av} \rangle$ [ns] ^[a]	1.09	0.38	0.51	1.89	0.53
k_{ET} [$\times 10^{10} \text{ s}^{-1}$]	–	1.71	1.04	–	1.36
R_0 [Å]	–	23	23	–	21
Φ_{ET} [%]	–	65	53	–	72
J [$\times 10^{-14} \text{ cm}^3 \text{ M}^{-1}$]	–	6.25	6.25	–	4.57

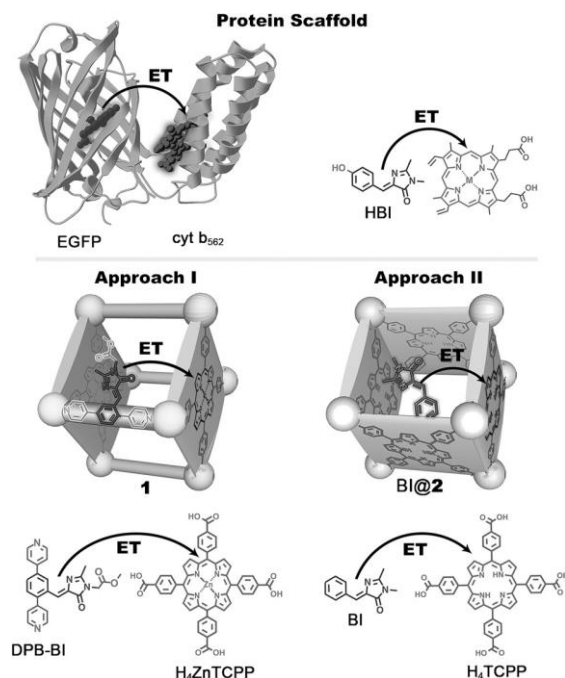


Figure 29. (top) Representation of ET between the two coupled chromophore cores of a green fluorescent protein variant (EGFP) and the electron-transfer protein, cytb562.[19] (bottom) Approaches I and II involved incorporation of chromophores with HBI- and porphyrin-based cores inside the rigid scaffold. Approach I focused on coordinative immobilization of both chromophores in crystalline scaffolds 1 and 1' while Approach II is based on inclusion of the BI donor in the porphyrin-based framework 2.⁶⁰

4.5.2 Porphyrin based MOFs materials as thin films

The discovery of porphyrin-based MOFs materials with light-harvesting and rapid energy transfer provides a variety choice of promising candidates in designing solar energy conversion devices. Fabricating MOFs in thin-film form on desired substrates is an especially attractive approach. Ideally, the designed MOF thin-films should meet certain criteria for practical application:

1. The thickness of films should be able to be precisely controlled by synthetic approach.
2. Directed exciton migration should be achieved with high efficiency and fast ET rate.
3. The exciton propagation distance should meet or exceed the MOF film thickness in order to move the exciton toward either an underlying electrode or external redox phase.

Following the study on DA-MOF in the powder form, So *et al.* grew DA-MOF as thin films on functionalized surfaces using a layer-by-layer (LBL) approach.⁶¹ The thickness of the film increased systematically with the number of assembly cycles. Polarization excitation and fluorescence measurements indicated that the porphyrin units are preferentially oriented in the MOF film. A far-red emitting squaraine dye (S1), which exhibits a high overlap integral with the DA-MOF, was deposited onto the surface of the MOF film. Exclusive emission from S1 was observed following selective excitation of Zn-porphyrin units in a 50-cycle film (Figure 30). These results suggest that the films can be used as antennae for light harvesting and efficient Förster energy transfer is possible within the film, considering the long-distance exciton propagation.⁹

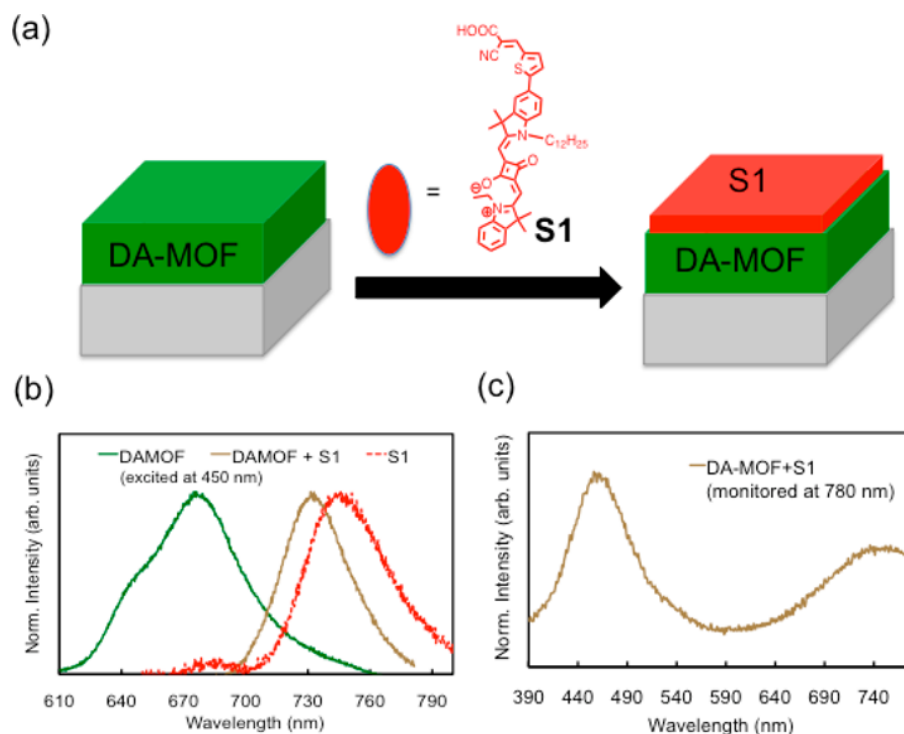


Figure 30. (a) Schematic diagram of preparation of sensitized DA-MOF film. (b) Comparison of emission profiles of DA-MOF (green solid), S1 (red solid), and DA-MOF sensitized with S1 (light-green dotted) upon excitation at 450 nm. (c) Excitation profile of the DA-MOF+S1 film monitored at 780 nm, where the emission from DA-MOF is negligible.⁶¹

In order to eliminate undesired exciton intralayer hopping, the Hupp's group converted a pillared paddlewheel porphyrin containing 3D MOF thin film to a 2D framework by solvent-assisted linker exchange (SALE).⁶² As shown in Figure 31, the pillar ligand 4,4'-bipyridine has been replaced by non-bridging ligand pyridine, leading to the collapse of the 3D MOF structure to a layered 2D coordination polymer. The distance between inter-layer chromophores significantly decreased due to the structural change, which resulted in enhanced energy transfer through the 2D MOF film. Pd-TCPP (P2) was used as an efficient, nonfluorescent energy acceptor (quencher) sited at the terminus of the film. Steady-state emission spectroscopy combined with time-resolved emission spectroscopy indicated that excitons can travel through about 9-11 porphyrin layers in the 2D films whereas, in the 3D films, exciton propagation only occurs through 6-8 chromophore layers. Considering the effective elimination of void space between porphyrin layers by SALE, one would expect a decrease in donor-acceptor separation distance, r , which should result in an enhancement in exciton migration through the 2D MOF films, from the simplest Förster energy transfer theory consideration. However, SALE-induced MOF collapse is accompanied by the lateral shifting of alternating 2D layers, which did not minimize the dipole-dipole coupling distance between the porphyrin chromophores as expected. Therefore, future direction for this strategy should focus on extending exciton propagation by diminishing chromophore interlayer spacing without also affecting the chromophore alignment and dipole– dipole coupling as a consequence.

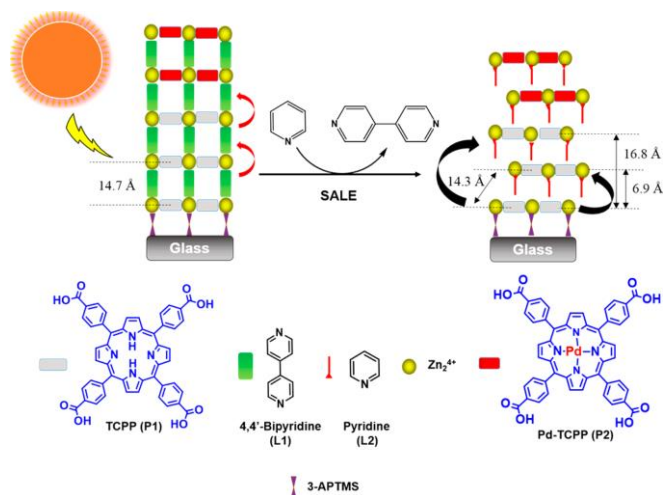


Figure 31. Free-base porphyrin P1 and linker L1 were used to fabricate N (number of cycles) cycles of MOF thin films followed by N + 1 and N + 2 cycles by palladium porphyrin P2 and linker L1.⁶²

Ideally, MOF thin films for solar energy conversion not only need directional ET in high efficiency, but also require high absorption which covers the visible light region as much as possible. Park *et al.* reported the synthesis of MOF-like thin films containing two perylenediimides (PDICl₄, PDIOPh₂) and a squaraine dye (S1), using a layer-by-layer assembly method.⁶³ As shown in Figure 32, 1,2,4,5-tetrakis(4-carboxyphenyl)benzene (L1) units as tetratopic linkers coordinate pairs of Zn(II) ions in paddlewheel fashion, and either (or both) N,N'-di(4-pyridyl)-1,7-di(3,5-ditert-butylphenoxy)-3,4,9,10-perylenetetracarboxylic diimide (PDIOPh₂) and N,N'-di(4-pyridyl)-1,6,7,12-tetrachloro-3,4,9,10-perylenetetracarboxylic diimide (PDICl₄) linkers serve as Zn(II)-ligating spacers/pillars between the L1-defined layers. The thickness of each layer with different building blocks can be precisely controlled through LBL assembly. Interestingly, the multicomponent MOF-like films can absorb light across visible light region and slightly beyond (350-750 nm) based on the functionalized perylene-diimide- and squaraine-type chromophores. Due to the high spectral overlap and oriented transition dipole moments of the donor (PDICl₄ and PDIOPh₂) and acceptor (S1) components, directional long-range energy transfer from the bluest to reddest absorber was successfully achieved. The observed panchromatic absorption and

cascade-type transport and delivery of molecular excitons over tens of nanometers to the film exterior have significant implications for the application in solar energy conversion.

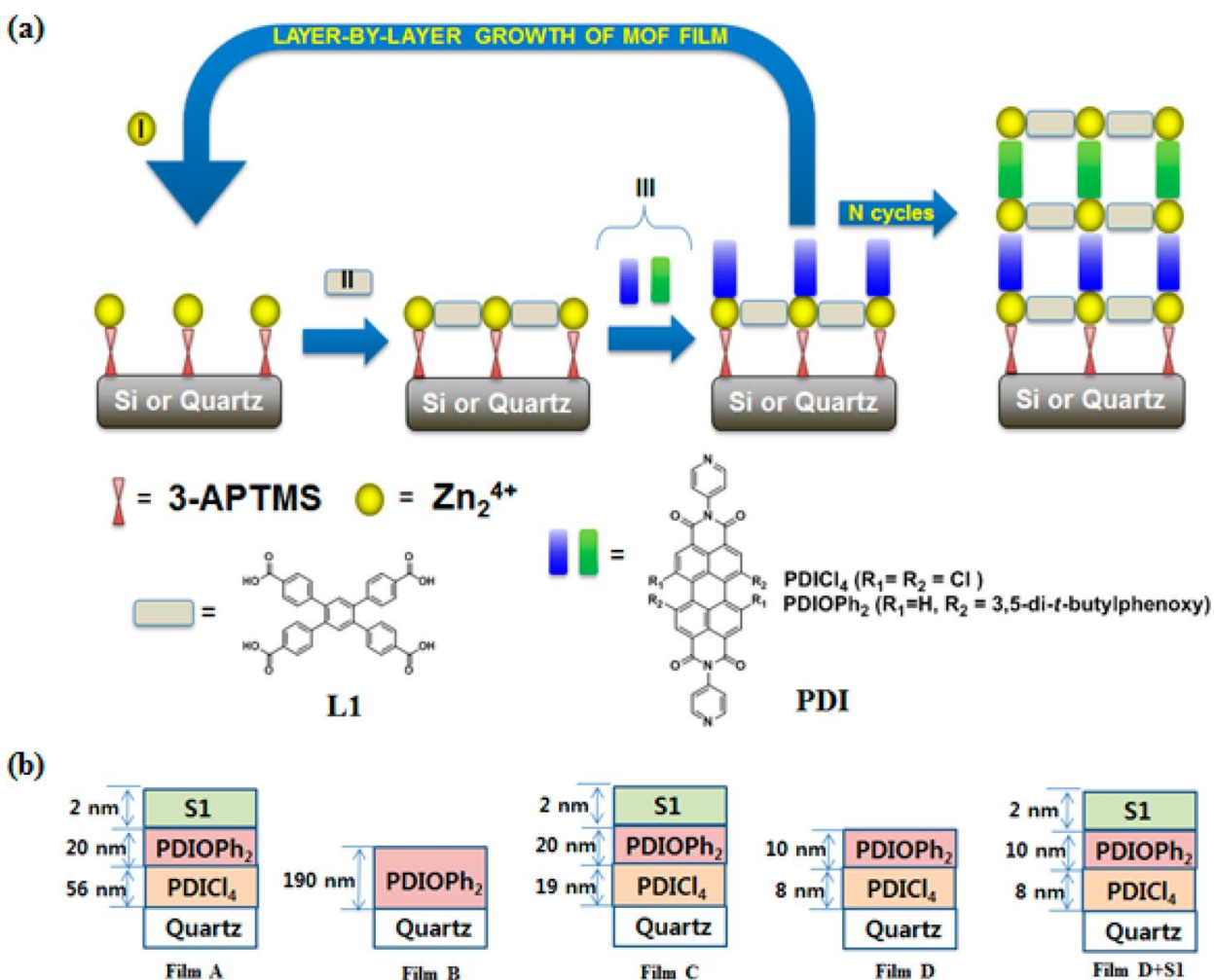


Figure 32. (a) Schematic diagram for sequential deposition of the MOF-like film via LBL assembly. Over N cycles, the thin MOF-like film is formed on silicon platform functionalized with 3-APTMS. Introduction of Zn(II) is followed by L1, and then PDI Cl_4 or PDIOPh $_2$. Note that the bay positions of the PDI are functionalized with either chlorine or 3,5-di-*t*-butylphenoxy groups. (b) Prepared thin MOF-like films of film A, film B, film C, film D, and film D+S1.⁶³

4.5.3 Summary

The use of porphyrin linkers in MOF assemblies not only mimics the molecular speciation of natural systems but also provides a scaffold for 3D control of orientation similar to protein

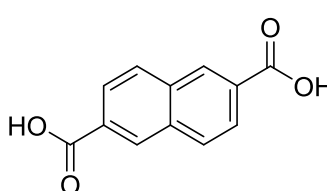
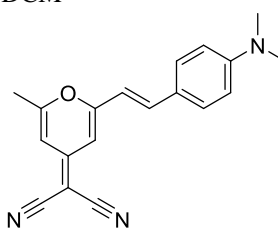
environment. While the pioneering examples here do not directly match the efficiency of biological approaches, critical information has been gained to guide future study:

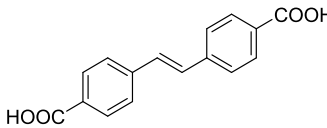
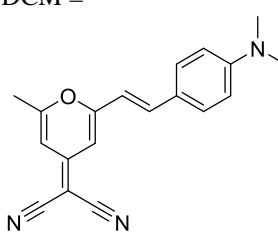
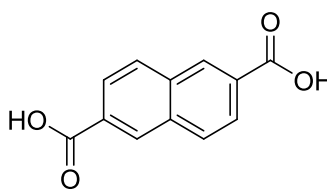
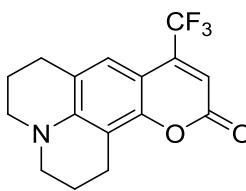
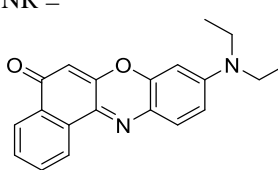
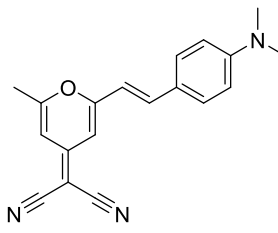
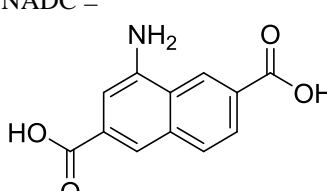
1. Long-range ET comprised of approximately 200 hops can be achieved between porphyrin chromophores.
2. The interporphyrin spacing is critical for efficient ET. Indeed, a factor of 2 in terms of number of hops can be achieved by collapsing parent MOF structures.
3. Photo-isomerizable linkers can be used as molecular switches to turn-on and turn-off photoluminescence via ET quenching.
4. LBL thin films of MOFs can result in efficient ET cascade assemblies, providing the potential for directional ET and charge separation at interfaces.

4.6 Non-porphyrinic, Organic Chromophore based MOFs

Organic chromophores such as naphthalene and stilbene have been used to study ET in MOF materials. Using different chromophores as ligands to construct heterolinker MOFs or assembling chromophore guests with MOF as host matrices are two common approaches that have been reported. Table 5 summarizes the reported MOFs that contain organic chromophores as ligands.

Table 5. MOFs constructed from ligands containing organic chromophores

MOF	Chemical Formula	Ligand Structure	Guest	Ref
DCM@IRMOF-8	$Zn_4O(C_{12}H_6O_4)$		DCM = 	[64]

DCM@stilbene-MOF	$Zn_4O(C_{16}H_{10}O_4)_3$		DCM = 	[65]
Zr-NDC	$Zr_6O_4(OH)_4(C_{12}H_6O_4)_6$	NDC = 	C153 =  NR =  DCM = 	[66]
Zr-NADC	$Zr_6O_4(OH)_4(C_{12}H_6O_4)_6$ $-x(C_{12}H_7NO_4)_x$	NADC = 		[67] [68]

Yan and coworkers reported the incorporation of a laser dye, 4-(dicyanomethylene)-2-methyl-6-(4-dimethylaminostyryl)-4H-pyran (DCM), into stilbene-based and naphthalene-based (IRMOF-8) MOF systems (Figure 33).⁶⁴ The resulting materials exhibit blue/red two color emission, corresponding to the MOF emission and DCM emission, respectively. Probed by 3D confocal fluorescence microscopy, the intensity ratio of blue to red fluorescence varies in different

planes within the MOF single crystals (Figure 34). The ratio is a function of the different degrees of energy transfer between the MOF hosts and guest molecules due to the non-uniform distribution of DCM within the MOF matrix. More DCM molecules are populated into the nano-channel away from the central plane of the MOF crystal than in the central plane itself, thus the energy transfer from the host matrix to DCM is more effective in those regions. The DFT calculations also indicate that host-guest energy transfer occurs for two DCM@MOF systems. Moreover, the luminescence response of the DCM@MOF systems is sensitive to volatile organic solvents (methanol, acetone and toluene), in that both the emission wavelength and the intensity ratio of blue to red emission vary after exposure, showing that the materials have potential applications in the fabrication of ratiometric luminescent sensors.

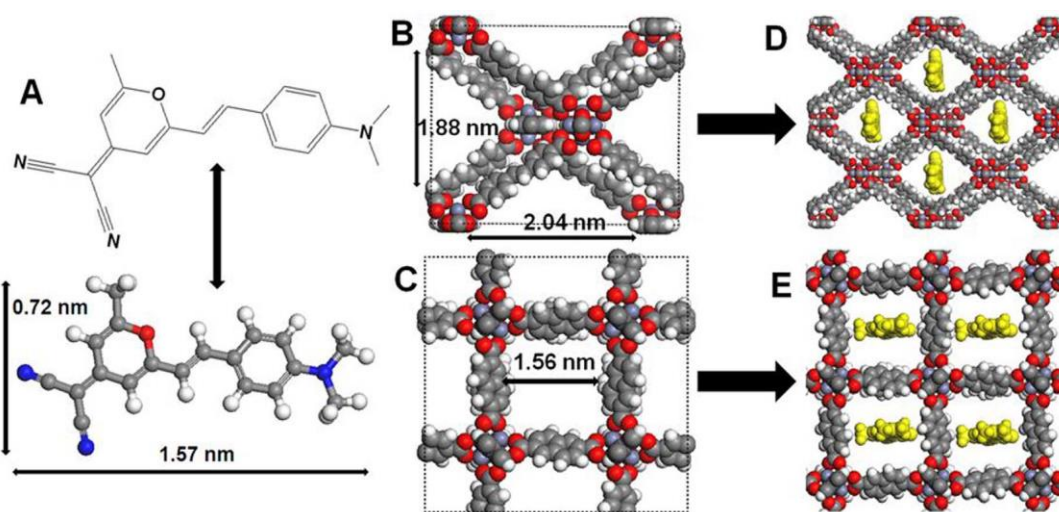


Figure 33. Incorporation of DCM guests into the nanochannels of MOFs. (A) The molecular structure of DCM; the host structures of stilbene-MOF (B) and IRMOF-8 (C); the schematic host-guest structures of DCM@stilbene-MOF (D) and DCM@IRMOF-8 (E).⁶⁴

A more detailed study to probe the energy transfer between MOF host with dye guest molecules has been reported by Douhal *et al.*⁶⁵ Three different laser dyes, Coumarin 153 (C153), Nile Red (NR) and 4-(dicyanomethylene)-2-methyl-6-(4-dimethyl-aminostyryl)-4H-pyran

(DCM), were trapped into a Zr-naphthalene dicarboxylic acid (Zr-NDC) MOF. By trapping these dyes into the Zr-NDC porous structure, the emission of the dye@MOF materials can be tuned due

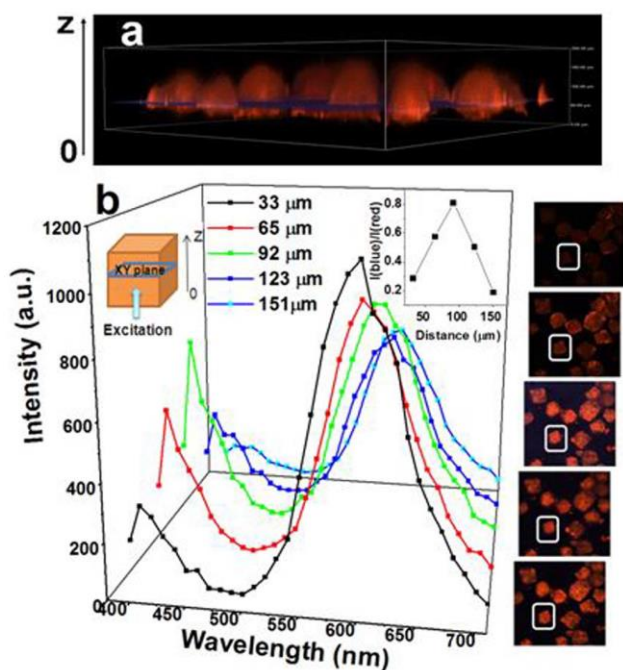


Figure 34. (a) 3D fluorescence image of the selected single crystal MOFs; (b) the two-color fluorescence spectra and intensity ratios of blue to red emission (inset) of an individual DCM@stilbene-MOF single crystal (outlined by the white color in the inset of b) in different xy-planes based on z-axis scanning. Inset photographs show the fluorescence images in focal planes at different distances (33, 65, 92, 123, and 151 μm) from the excitation laser (372 nm).⁶⁴

to energy transfer photoevents. For example, encapsulating C153 or NR, the original blue emission from MOF could be changed to green (C153) or red (NR). Moreover, the white-light-emitting composite materials can be obtained by simultaneously doping C153 and NR, or DCM, with quantum yields up to 41%. The obtained white light has CIE coordinates (0.32, 0.34), which are very close to the ideal ones (0.33, 0.33). The dynamic studies showed that different dyes lead to different energy transfer process, mainly due to their different occupancy in the MOF pores. For C153, it can occupy two different pores of the MOF dependent on doping concentration. At lower C153 loading concentrations the mean ET process time (from MOF monomers to C153) is ~ 3.3

ns, whereas at higher concentrations, it is ~360 ps. While for NR and DCM, the ET process happens from the MOF excimer to the trapped dyes.

Douhal and Sánchez reported the spectral and dynamic properties of two Zr-based MOFs, Zr-2,6-naphthalenedicarboxylate (Zr-NDC) MOF and 4-amino-2,6-naphthalenedicarboxylate (Zr-NADC) MOF.⁶⁶⁻⁶⁸ They first observed intraparticle excimer formation between neighboring naphthalene organic linkers in a diluted Zr-NDC MOF suspension.⁶⁶ Excimer formation is reflected by a broad red-shifted band in the Zr-NDC emission spectrum and also by its dynamics composed of three components; $\tau_1 = 650$ ps (excimer formation process), $\tau_2 = 3.7$ ns (monomer lifetime) and $\tau_3 = 13.9$ ns (excimer lifetime). By increasing the polarity of the solvent, blue shifts in both the absorption and the emission spectrum were observed. Furthermore, the excimer formation time changed significantly from 490 ps in ACN to 840 ps in DCM, which may be attributed to the MOF structure breathing effect, induced by the filling of solvent. Interestingly, at higher concentrations of MOF particles in suspensions of THF, fs-dynamic studies showed an ultrafast intercrystal excimer formation occurring in ~5 ps. The observation is attributed to the interaction between naphthalenes of closely associated MOF particles (Figure 35).

A follow-up study constructed a Zr-NADC MOFs by using heterolinker, a mixture of 2,6-naphthalenedicarboxylate (NDC) and 4-amino-2,6-naphthalenedicarboxylate (NADC). The fraction of NADC relative to NDC varied from 2% to 35% in these MOFs.⁶⁷ Increase percentages of NADC linkers in the MOF led to a decrease in the lifetime of NDC excimer formation, which can be explained by an increase in energy-transfer probability between NDC and NADC. Meanwhile, the emission intensity of NADC experienced a drop at the highest doping percentage in the MOF, mainly due to the ultrafast charge transfer assisted by the amino group. Specifically,

at the lowest NADC doping concentration (2%), the photodynamics are similar to Zr-NDC, mainly dominated by NDC-excimer photo-formation. With increase of NADC linkers in Zr-NADC MOFs

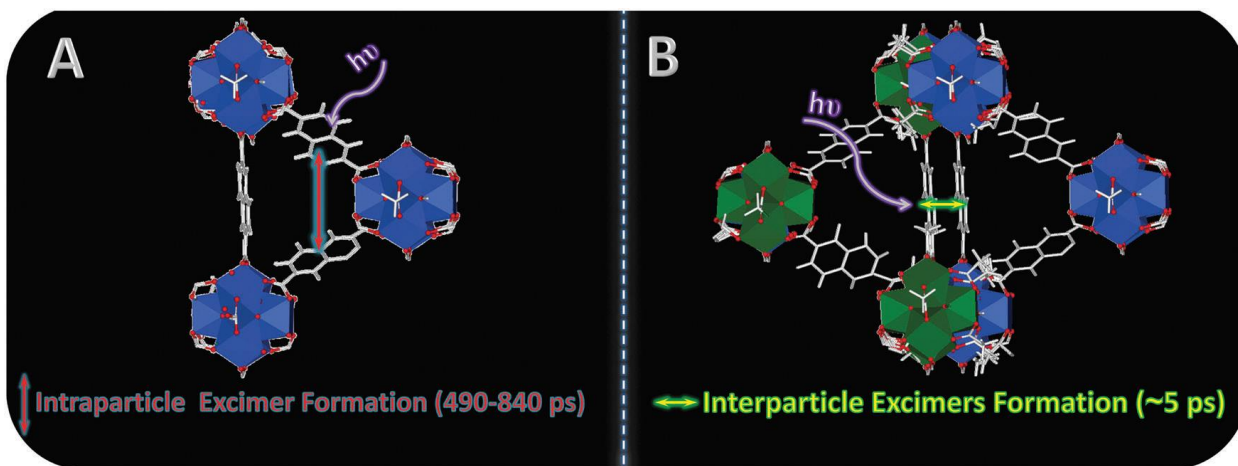


Figure 35. Representation of the excimer photoformation in (A) diluted suspensions, due to the interaction between naphthalenes of the same MOF crystal and (B) concentrated THF suspension, owing to interactions between naphthalenes of closely associated MOF crystals.⁶⁶

(5 and 10%), the lifetime of excimer is decreased because of higher probability for ET between NDC and NADC. For NADC fractions of 20 and 35%, we observed a very fast rise component (1.2 ps) in the emission signal due to the related ET between the heterolinkers. These results showed that by using MOFs with heterolinkers, it is possible to trigger and tune excimer formation and ET processes.

4.6.1 Summary

While organic chromophores typically exhibit short lived excited states, they have still found utility in MOF ET studies. Of particular interest is the work on in-MOF excimer formation and the effect on observed photophysics. There appears to be a moderate effect of encapsulation species on the formation of these excimers and further study is needed to uncover the guiding principles

behind this phenomenon. Additionally, the use of perylenediimides led to the first example of a multicomponent ET cascade in MOF-like thin films.

4.7 Bibliography

1. Atkins, P. W.; Friedman, R., *Molecular quantum mechanics*. Oxford University Press: 2011; p 537-537.
2. Schatz, G.; Ratner, M., *Quantum Mechanics in Chemistry*. Dover Publications, Inc.: 1993.
3. Tokmakoff, A., *Introductory Quantum Mechanics II*. 2009.
4. Greyson, E. C.; Vura-Weis, J.; Michl, J.; Ratner, M. A., Maximizing singlet fission in organic dimers: theoretical investigation of triplet yield in the regime of localized excitation and fast coherent electron transfer. *J. Phys. Chem. B* **2010**, *114* (45), 14168-77.
5. Parkhill, J. A.; Tempel, D. G.; Aspuru-Guzik, A., Exciton coherence lifetimes from electronic structure. *J. Chem. Phys.* **2012**, *136* (10), 104510-104510.
6. Lin, S. H.; Xiao, W. Z.; Dietz, W., Generalized Förster-Dexter theory of photoinduced intramolecular energy transfer. *Phys. Rev. E* **1993**, *47* (5), 3698-3706.
7. Skourtis, S. S.; Liu, C.; Antoniou, P.; Virshup, A. M.; Beratan, D. N., Dexter energy transfer pathways. *Proc. Natl. Acad. Sci. U. S. A.* **2016**, *113* (29), 8115-20.
8. Lin, J.; Hu, X.; Zhang, P.; Van Rynbach, A.; Beratan, D. N.; Kent, C. A.; Mehl, B. P.; Papanikolas, J. M.; Meyer, T. J.; Lin, W.; Skourtis, S. S.; Constantinou, M., Triplet Excitation Energy Dynamics in Metal–Organic Frameworks. *The Journal of Physical Chemistry C* **2013**, *117* (43), 22250-22259.
9. So, M. C.; Wiederrecht, G. P.; Mondloch, J. E.; Hupp, J. T.; Farha, O. K., Metal-organic framework materials for light-harvesting and energy transfer. *Chemical Communications* **2015**, *51* (17), 3501-3510.
10. Heine, J.; Muller-Buschbaum, K., Engineering metal-based luminescence in coordination polymers and metal-organic frameworks. *Chemical Society Reviews* **2013**, *42* (24), 9232-9242.

11. Zhang, T.; Lin, W., Metal-organic frameworks for artificial photosynthesis and photocatalysis. *Chemical Society Reviews* **2014**, *43* (16), 5982-5993.
12. Zhang, X.; Wang, W.; Hu, Z.; Wang, G.; Uvdal, K., Coordination polymers for energy transfer: Preparations, properties, sensing applications, and perspectives. *Coordination Chemistry Reviews* **2015**, *284*, 206-235.
13. Dhakshinamoorthy, A.; Asiri, A. M.; García, H., Metal–Organic Framework (MOF) Compounds: Photocatalysts for Redox Reactions and Solar Fuel Production. *Angewandte Chemie International Edition* **2016**, *55* (18), 5414-5445.
14. Williams, D. E.; Shustova, N. B., Metal–Organic Frameworks as a Versatile Tool To Study and Model Energy Transfer Processes. *Chemistry – A European Journal* **2015**, *21* (44), 15474-15479.
15. Eliseeva, S. V.; Bünzli, J.-C. G., Lanthanide luminescence for functional materials and biosciences. *Chemical Society Reviews* **2010**, *39* (1), 189-227.
16. Binnemans, K., Lanthanide-Based Luminescent Hybrid Materials. *Chemical Reviews* **2009**, *109* (9), 4283-4374.
17. Bünzli, J.-C. G., Lanthanide Luminescence for Biomedical Analyses and Imaging. *Chemical Reviews* **2010**, *110* (5), 2729-2755.
18. Zhang, X.; Ballem, M. A.; Ahrén, M.; Suska, A.; Bergman, P.; Uvdal, K., Nanoscale Ln(III)-Carboxylate Coordination Polymers (Ln = Gd, Eu, Yb): Temperature-Controlled Guest Encapsulation and Light Harvesting. *Journal of the American Chemical Society* **2010**, *132* (30), 10391-10397.
19. Zhang, X.; Ballem, M. A.; Hu, Z.-J.; Bergman, P.; Uvdal, K., Nanoscale Light-Harvesting Metal–Organic Frameworks. *Angewandte Chemie International Edition* **2011**, *50* (25), 5729-5733.
20. Balamurugan, A.; Gupta, A. K.; Boomishankar, R.; Lakshmiipathi Reddy, M.; Jayakannan, M., Heavy Atom Effect Driven Organic Phosphors and Their Luminescent Lanthanide Metal–Organic Frameworks. *ChemPlusChem* **2013**, *78* (7), 737-745.
21. Li, Y.; Zhang, S.; Song, D., A Luminescent Metal–Organic Framework as a Turn-On Sensor for DMF Vapor. *Angewandte Chemie International Edition* **2013**, *52* (2), 710-713.

22. Dang, S.; Min, X.; Yang, W.; Yi, F.-Y.; You, H.; Sun, Z.-M., Lanthanide Metal–Organic Frameworks Showing Luminescence in the Visible and Near-Infrared Regions with Potential for Acetone Sensing. *Chemistry – A European Journal* **2013**, *19* (50), 17172-17179.
23. Zhou, J.-M.; Shi, W.; Li, H.-M.; Li, H.; Cheng, P., Experimental Studies and Mechanism Analysis of High-Sensitivity Luminescent Sensing of Pollutational Small Molecules and Ions in Ln₄O₄ Cluster Based Microporous Metal–Organic Frameworks. *The Journal of Physical Chemistry C* **2014**, *118* (1), 416-426.
24. Lu, W.-G.; Jiang, L.; Feng, X.-L.; Lu, T.-B., Three-Dimensional Lanthanide Anionic Metal–Organic Frameworks with Tunable Luminescent Properties Induced by Cation Exchange. *Inorganic Chemistry* **2009**, *48* (15), 6997-6999.
25. Xiao, Y.; Cui, Y.; Zheng, Q.; Xiang, S.; Qian, G.; Chen, B., A microporous luminescent metal-organic framework for highly selective and sensitive sensing of Cu²⁺ in aqueous solution. *Chemical Communications* **2010**, *46* (30), 5503-5505.
26. Cai, S.-L.; Zheng, S.-R.; Fan, J.; Xiao, T.-T.; Tan, J.-B.; Zhang, W.-G., A new sensor based on luminescent terbium–organic framework for detection of Fe³⁺ in water. *Inorganic Chemistry Communications* **2011**, *14* (6), 937-939.
27. Wright, W. D., A re-determination of the trichromatic coefficients of the spectral colours. *Transactions of the Optical Society* **1929**, *30* (4), 141.
28. Guild, J., The Colorimetric Properties of the Spectrum. *Philosophical Transactions of the Royal Society of London. Series A, Containing Papers of a Mathematical or Physical Character* **1932**, *230* (681-693), 149-187.
29. Rodrigues, M. O.; Dutra, J. D. L.; Nunes, L. A. O.; de Sá, G. F.; de Azevedo, W. M.; Silva, P.; Paz, F. A. A.; Freire, R. O.; A. Júnior, S., Tb³⁺→Eu³⁺ Energy Transfer in Mixed-Lanthanide-Organic Frameworks. *The Journal of Physical Chemistry C* **2012**, *116* (37), 19951-19957.
30. Matthes, P.; Höller, C. J.; Mai, M.; Heck, J.; Sedlmaier, S. J.; Schmiechen, S.; Feldmann, C.; Schnick, W.; Müller-Buschbaum, K., Luminescence tuning of MOFs via ligand to metal and metal to metal

energy transfer by co-doping of $2\infty[\text{Gd}_2\text{Cl}_6(\text{bipy})_3] \cdot 2\text{bipy}$ with europium and terbium. *Journal of materials chemistry* **2012**, 22 (20), 10179-10187.

31. Ma, M.-L.; Ji, C.; Zang, S.-Q., Syntheses, structures, tunable emission and white light emitting Eu^{3+} and Tb^{3+} doped lanthanide metal-organic framework materials. *Dalton Transactions* **2013**, 42 (29), 10579-10586.

32. Liu, Z.-F.; Wu, M.-F.; Wang, S.-H.; Zheng, F.-K.; Wang, G.-E.; Chen, J.; Xiao, Y.; Wu, A. Q.; Guo, G.-C.; Huang, J.-S., Eu^{3+} -doped Tb^{3+} metal-organic frameworks emitting tunable three primary colors towards white light. *Journal of Materials Chemistry C* **2013**, 1 (31), 4634-4639.

33. Cui, Y.; Xu, H.; Yue, Y.; Guo, Z.; Yu, J.; Chen, Z.; Gao, J.; Yang, Y.; Qian, G.; Chen, B., A Luminescent Mixed-Lanthanide Metal–Organic Framework Thermometer. *Journal of the American Chemical Society* **2012**, 134 (9), 3979-3982.

34. Rao, X.; Song, T.; Gao, J.; Cui, Y.; Yang, Y.; Wu, C.; Chen, B.; Qian, G., A Highly Sensitive Mixed Lanthanide Metal–Organic Framework Self-Calibrated Luminescent Thermometer. *Journal of the American Chemical Society* **2013**, 135 (41), 15559-15564.

35. Miyata, K.; Konno, Y.; Nakanishi, T.; Kobayashi, A.; Kato, M.; Fushimi, K.; Hasegawa, Y., Chameleon Luminophore for Sensing Temperatures: Control of Metal-to-Metal and Energy Back Transfer in Lanthanide Coordination Polymers. *Angewandte Chemie International Edition* **2013**, 52 (25), 6413-6416.

36. Yan, C.; Li, K.; Wei, S.-C.; Wang, H.-P.; Fu, L.; Pan, M.; Su, C.-Y., Lanthanide homometallic and d-f heterometallic MOFs from the same tripodal ligand: structural comparison, one photon (OP) vs. two photon (TP) luminescence and selective guest adsorption behavior. *Journal of Materials Chemistry* **2012**, 22 (19), 9846-9852.

37. Liu, Y.; Pan, M.; Yang, Q.-Y.; Fu, L.; Li, K.; Wei, S.-C.; Su, C.-Y., Dual-Emission from a Single-Phase Eu – Ag Metal–Organic Framework: An Alternative Way to Get White-Light Phosphor. *Chemistry of Materials* **2012**, 24 (10), 1954-1960.

38. Luo, F.; Batten, S. R., Metal-organic framework (MOF): lanthanide(iii)-doped approach for luminescence modulation and luminescent sensing. *Dalton Transactions* **2010**, 39 (19), 4485-4488.
39. An, J.; Shade, C. M.; Chengelis-Czegana, D. A.; Petoud, S.; Rosi, N. L., Zinc-Adeninate Metal–Organic Framework for Aqueous Encapsulation and Sensitization of Near-infrared and Visible Emitting Lanthanide Cations. *Journal of the American Chemical Society* **2011**, 133 (5), 1220-1223.
40. Ma, M.-L.; Qin, J.-H.; Ji, C.; Xu, H.; Wang, R.; Li, B.-J.; Zang, S.-Q.; Hou, H.-W.; Batten, S. R., Anionic porous metal-organic framework with novel 5-connected vbk topology for rapid adsorption of dyes and tunable white light emission. *Journal of Materials Chemistry C* **2014**, 2 (6), 1085-1093.
41. Ward, M. D.; Barigelletti, F., Control of photoinduced energy transfer between metal-polypyridyl luminophores across rigid covalent, flexible covalent, or hydrogen-bonded bridges. *Coordination Chemistry Reviews* **2001**, 216, 127-154.
42. Fleming, C. N.; Maxwell, K. A.; DeSimone, J. M.; Meyer, T. J.; Papanikolas, J. M., Ultrafast excited-state energy migration dynamics in an efficient light-harvesting antenna polymer based on Ru (II) and Os (II) polypyridyl complexes. *Journal of the American Chemical Society* **2001**, 123 (42), 10336-10347.
43. Tsushima, M.; Ikeda, N.; Yoshimura, A.; Nozaki, K.; Ohno, T., Solid-state photochemistry: energy-transfer and electron-transfer of 3 CT in crystals of $[\text{Os}_x \text{Ru}_{1-x}(\text{bpy})_3]_2 \text{X}$ ($x=0-0.23$). *Coordination Chemistry Reviews* **2000**, 208 (1), 299-308.
44. Yersin, H.; Kratzer, C., Energy transfer and harvesting in $[\text{Ru}_{1-x}\text{Os}_x(\text{bpy})_3](\text{PF}_6)_2$ and $\{\Delta-[\text{Ru}(\text{bpy})_3] \Delta-[\text{Os}(\text{bpy})_3]\}(\text{PF}_6)_4$. *Coordination chemistry reviews* **2002**, 229 (1), 75-93.
45. Kent, C. A.; Mehl, B. P.; Ma, L.; Papanikolas, J. M.; Meyer, T. J.; Lin, W., Energy transfer dynamics in metal– organic frameworks. *Journal of the American Chemical Society* **2010**, 132 (37), 12767-12769.
46. Kent, C. A.; Liu, D.; Ma, L.; Papanikolas, J. M.; Meyer, T. J.; Lin, W., Light harvesting in microscale metal–organic frameworks by energy migration and interfacial electron transfer quenching. *Journal of the American Chemical Society* **2011**, 133 (33), 12940-12943.

47. Kent, C. A.; Liu, D.; Meyer, T. J.; Lin, W., Amplified luminescence quenching of phosphorescent metal–organic frameworks. *Journal of the American Chemical Society* **2012**, *134* (9), 3991-3994.
48. Kent, C. A.; Liu, D.; Ito, A.; Zhang, T.; Brennaman, M. K.; Meyer, T. J.; Lin, W., Rapid energy transfer in non-porous metal–organic frameworks with caged Ru (bpy) 3^{2+} chromophores: oxygen trapping and luminescence quenching. *Journal of Materials Chemistry A* **2013**, *1* (47), 14982-14989.
49. Tang, Y.; He, W.; Lu, Y.; Fielden, J.; Xiang, X.; Yan, D., Assembly of Ruthenium-Based Complex into Metal–Organic Framework with Tunable Area-Selected Luminescence and Enhanced Photon-to-Electron Conversion Efficiency. *The Journal of Physical Chemistry C* **2014**, *118* (44), 25365-25373.
50. Cavka, J. H.; Jakobsen, S.; Olsbye, U.; Guillou, N.; Lamberti, C.; Bordiga, S.; Lillerud, K. P., A New Zirconium Inorganic Building Brick Forming Metal Organic Frameworks with Exceptional Stability. *Journal of the American Chemical Society* **2008**, *130* (42), 13850-13851.
51. Bon, V.; Senkovska, I.; Weiss, M. S.; Kaskel, S., Tailoring of network dimensionality and porosity adjustment in Zr- and Hf-based MOFs. *CrystEngComm* **2013**, *15* (45), 9572-9577.
52. Wang, C.; Xie, Z.; deKrafft, K. E.; Lin, W., Doping Metal–Organic Frameworks for Water Oxidation, Carbon Dioxide Reduction, and Organic Photocatalysis. *Journal of the American Chemical Society* **2011**, *133* (34), 13445-13454.
53. Maza, W. A.; Morris, A. J., Photophysical Characterization of a Ruthenium(II) Tris(2,2'-bipyridine)-Doped Zirconium UiO-67 Metal–Organic Framework. *The Journal of Physical Chemistry C* **2014**, *118* (17), 8803-8817.
54. Maza, W. A.; Padilla, R.; Morris, A. J., Concentration dependent dimensionality of resonance energy transfer in a postsynthetically doped morphologically homologous analogue of uio-67 mof with a ruthenium (ii) polypyridyl complex. *Journal of the American Chemical Society* **2015**, *137* (25), 8161-8168.
55. Meyer, T. J., Photochemistry of metal coordination complexes: metal to ligand charge transfer excited states. In *Pure and Applied Chemistry*, 1986; Vol. 58, p 1193.
56. Kenkre, V. M.; Knox, R. S., Theory of Fast and Slow Excitation Transfer Rates. *Physical Review Letters* **1974**, *33* (14), 803-806.

57. Son, H.-J.; Jin, S.; Patwardhan, S.; Wezenberg, S. J.; Jeong, N. C.; So, M.; Wilmer, C. E.; Sarjeant, A. A.; Schatz, G. C.; Snurr, R. Q., Light-harvesting and ultrafast energy migration in porphyrin-based metal–organic frameworks. *Journal of the American Chemical Society* **2013**, *135* (2), 862-869.
58. Lee, C. Y.; Farha, O. K.; Hong, B. J.; Sarjeant, A. A.; Nguyen, S. T.; Hupp, J. T., Light-Harvesting Metal–Organic Frameworks (MOFs): Efficient Strut-to-Strut Energy Transfer in Bodipy and Porphyrin-Based MOFs. *Journal of the American Chemical Society* **2011**, *133* (40), 15858-15861.
59. Williams, D. E.; Rietman, J. A.; Maier, J. M.; Tan, R.; Greytak, A. B.; Smith, M. D.; Krause, J. A.; Shustova, N. B., Energy Transfer on Demand: Photoswitch-Directed Behavior of Metal–Porphyrin Frameworks. *Journal of the American Chemical Society* **2014**, *136* (34), 11886-11889.
60. Dolgoplova, E. A.; Williams, D. E.; Greytak, A. B.; Rice, A. M.; Smith, M. D.; Krause, J. A.; Shustova, N. B., A Bio-inspired Approach for Chromophore Communication: Ligand-to-Ligand and Host-to-Guest Energy Transfer in Hybrid Crystalline Scaffolds. *Angewandte Chemie International Edition* **2015**, *54* (46), 13639-13643.
61. So, M. C.; Jin, S.; Son, H.-J.; Wiederrecht, G. P.; Farha, O. K.; Hupp, J. T., Layer-by-Layer Fabrication of Oriented Porous Thin Films Based on Porphyrin-Containing Metal–Organic Frameworks. *Journal of the American Chemical Society* **2013**, *135* (42), 15698-15701.
62. Goswami, S.; Ma, L.; Martinson, A. B.; Wasielewski, M. R.; Farha, O. K.; Hupp, J. T., Toward Metal-Organic Framework Based Solar Cells: Enhancing Directional Exciton Transport by Collapsing Three-Dimensional Film Structures. *ACS Applied Materials & Interfaces* **2016**.
63. Park, H. J.; So, M. C.; Gosztola, D.; Wiederrecht, G. P.; Emery, J. D.; Martinson, A. B. F.; Er, S.; Wilmer, C. E.; Vermeulen, N. A.; Aspuru-Guzik, A.; Stoddart, J. F.; Farha, O. K.; Hupp, J. T., Layer-by-Layer Assembled Films of Perylene Diimide- and Squaraine-Containing Metal–Organic Framework-like Materials: Solar Energy Capture and Directional Energy Transfer. *ACS Applied Materials & Interfaces* **2016**, *8* (38), 24983-24988.

64. Yan, D.; Tang, Y.; Lin, H.; Wang, D., Tunable Two-color Luminescence and Host–guest Energy Transfer of Fluorescent Chromophores Encapsulated in Metal–Organic Frameworks. *Scientific reports* **2014**, *4*.
65. Gutiérrez, M.; Sánchez, F.; Douhal, A., Efficient multicolor and white light emission from Zr-based MOF composites: spectral and dynamic properties. *Journal of Materials Chemistry C* **2015**, *3* (43), 11300-11310.
66. Gutiérrez, M.; Sánchez, F.; Douhal, A., Spectral and dynamical properties of a Zr-based MOF. *Physical Chemistry Chemical Physics* **2016**, *18* (7), 5112-5120.
67. Gutiérrez, M.; Sánchez, F.; Douhal, A., Competitive Excimer Formation and Energy Transfer in Zr-Based Heterolinker Metal–Organic Frameworks. *Chemistry-A European Journal* **2016**, *22* (37), 13072-13082.
68. Gutierrez, M.; Cohen, B.; Sánchez, F.; Douhal, A., Photochemistry of Zr-based MOFs: ligand-to-cluster charge transfer, energy transfer and excimer formation, what else is there? *Physical Chemistry Chemical Physics* **2016**, *18* (40), 27761-27774.